SYNTHESIS, STRUCTURE AND ELECTRICAL PROPERTIES OF SODIUM ZIRCONIUM PHOSPHATE $Na_{1-x}LixZr_2(PO_4)3(x=0.00-0.75)$

BY

AHMADU UMARU B.Sc. (ABU 1990), M.Sc. (ABU 2005)

Ph.D/SCIEN/03625/2006-07

A DISSERTATION SUBMITTED TO THE POSTGRADUATE SCHOOL,

AHMADU BELLO UNIVERSITY, ZARIA

NIGERIA

IN PARTIAL FULFILLMENT FOR THE AWARD

OF DOCTOR OF PHILOSOPHY DEGREE IN

PHYSICS

DEPARTMENT OF PHYSICS

AHMADU BELLO UNIVERSITY, ZARIA

NIGERIA

October, 2010

DECLARATION

I declare that the work in the dissertation entitled 'Synthesis, structure and electrical properties of sodium zirconium phosphate $Na_{1-x}Li_xZr_2(PO_4)_3$ (x=0.00-0.75)' has been performed by me in the department of Physics under the supervision of Professor S. A. Jonah, Dr. N. Rabiu and Dr. A. O. Musa of Bayero University, Kano.

The information derived from the literature has been duly acknowledged in the text and a list of references provided. No part of this publication was previously presented for another degree or diploma at any University.

Ahmadu Umaru		October, 2010
Name of student	Signature	Date

CERTIFICATION

This dissertation entitled "**SYNTHESIS, STRUCTURE AND ELECTRICAL PROPERTIES OF SODIUM ZIRCONIUM PHOSPHATE $Na_{1-x}Li_xZr_2(PO_4)_3$ (x=0.00-0.75)**" by Ahmadu Umaru meets the regulations governing the award of the Degree of Doctor of Philosophy in Physics of Ahmadu Bello University Zaria and it is approved for its contribution to scientific knowledge and literary presentation.

Professor S.A. Jonah
Chairman, Supervisory Committee
Date: 06/11/2010

Dr. A.O. Musa
Member, Supervisory Committee
Date: 06/11/2010

Dr. N. Rabiu
Member, Supervisory Committee
Date: 21/12/2010

Dr. N. Rabiu
Head of Department
Date: 21/12/2010

Professor A. A. Joshua
Dean, Postgraduate School
Date: 23/5/2011

DEDICATION

...to:

The Omnipotent, The Omniscient, The Elevator, The Sustainer, The Master of Wisdom and Excellence

ACKNOWLEDGEMENT

I am indebted to many individuals within and outside the country for the successful completion of this work. However, I can only thank a few by their names but acknowledge the contributions of others. Thus my unreserved gratitude and appreciation posthumously, goes to the late Professor N. I. Hariharan, for introducing me to the concept of superionic conductors. I'm deeply grateful to my supervisory committee members, Professor S.A. Jonah, Drs. A. O. Musa and N. Rabiu, for their exemplary understanding and guidance throughout the work. The individual contributions they made enriched my knowledge and experience enormously. I should express my gratitude to the Director-General, National Agency for Science and Engineering Infrastructure (NASENI), Abuja, Professor Olusegun Adewoye, for his advice regarding some aspects of the work. This eventually facilitated the linkage in carrying out the Thermogravimetric Analysis (TGA) characterization by Dr. Sunday Afolabi, of the Mechanical Engineering departemnt, University of Witwatersrand, South Africa.To whom I am grateful.

Professor Sunday Thomas, Director–General, Sheda Science and Technology Complex (SHETSCO), Abuja, helped with useful theoretical guide in the synthesis of the materials. I acknowledge my indebtedness to him and appreciate the gesture. I also acknowledge and express my thankfulness on the synthesis to Dr. Jonathan Yisa, Chemistry department, Federal University of Technology, Minna. I am grateful to Dr. Tomas Salkus, Faculty of Physics, Vilnius University, Lithuania and his research group, for their suggestions regarding the synthesis conditions and stoichiometric calculations of the compositions. I must doubly thank him for the collaboration on Impedance spectroscopy characterization. Dr. Noppadon Nuntawong, of the Institute

for Electronic and Computer Technology, Thailand, also extended a similar collaboration in the area of Scanning Electron Microscopy (SEM), which is highly appreciated. I thank Engineer Shehu Ahmed Isah for the furnace work at the National Metallurgical Development Centre (NMDC), Jos and Dr. Kasim Uthman Isah, of the Physics department, FUT, Minna, who made this possible.

I express my sincere appreciations to Drs. P.O. Akusu, Saddiq Umar and Zakari Yusuf Ibrahim of the Physics department, Ahmadu Bello University, Zaria, for the various roles they played through their constructive criticism of the work. I also recognize the contributions of Dr. Yusuf Ahmed, Centre for Energy Research and Training (CERT), Zaria.

My profound gratitude also goes to my colleagues Mr. Auwal Musa Muhammad of CERT, Zaria, Mr. Tajudeen Olajide Ahmed and Mr. Jimoh Raimi of the physics department, ABU, Zaria and Mr. Abdelmalik Abdelgaffar of the University of Leicester, U.K., for their contributions in ways too numerous to mention. I wish to acknowledge the tremendous understanding and support from my wife Aishatu Abubakar, and my children who missed me so much.

ABSTRACT

Lithium doped Sodium Zirconium Phosphate, $Na_{1-x}Li_xZr_2(PO_4)_3$ (x= 0.00-0.75), belonging to the NASICON family of compounds is synthesized by solid state reaction and characterized by thermal analysis using DTA/TGA. The lithium doped compositions show high thermal stability in the temperature range from 873-1273K with an enhancement of their sinterability. No structural transformation was observed in the compositions. X-ray diffraction, in conjunction with scanning electron microscopy show that some compositions do not contain ZrO_2 second phase which is normally associated with solid state reaction. This is attributed to the processing technique. The SEM micrographs of sample x = 0.50 show dense particles with average size of 3-7μm of similar shapes. The impedance spectra of composition x=0.50 is observed to have two semicircles representing the grain and grain boundary processes. In sample x=0.75, a distorted semicircle and a straight line inclined at an angle is observed, representing grain boundary and electrode processes. The impedance curve for the x=0.00 sample did not give good semicircle due to the extremely high insulating properties at temperatures up to 550K. The temperature dependent conductivity for all the compositions is a straight line exhibiting the Arrhenius character, both for bulk and total conductivity. The values of conductivity obtained for the lithium doped samples show an improvement over reported values and their activation energies are within the range obtained for these materials. The highest value of conductivity obtained at 600K is 0.3S/m, for the sample with the highest lithium composition, $Na_{0.25}Li_{0.75}Zr_2(PO_4)_3$, representing the bulk conductivity, while the total conductivity is 0.1S/m at 590K. The activation energy is $0.41eV$. The increment in conductivity and the low activation energy is attributed to the level of densification attained in the compositions and to the processing method used. The

conductivity of sample x=0.00 is the least. The frequency dependence of the conductivity show two regions of frequency dispersion for bulk and grain boundary. These are observed to shift with increasing temperature towards higher frequency, establishing the activated nature of ionic transport. An abrupt drop in conductivity is observed for the lithium-doped samples at frequencies near the GHz region which is attributed to, among other factors, the effect of two mobile ions (Na^+, Li^+) reported in literature to result in fall in conductivity in some superionic glasses. The activation energies are observed to decrease at higher dopant levels of lithium.

TABLE OF CONTENTS

TITLE		PAGE
Title page		i
Declaration		ii
Certification		iii
Dedication		iv
Acknowledgement		v
Abstract		vii
Table of Contents		ix
List of Tables		xii
List of Figures		xiii
List of Appendices		xxii
CHAPTER ONE: GENERAL INTRODUCTION		1
1.1	Ionic Materials	1
1.2	Literature Review	5
1.2.1	Synthesis and Phase Transitions in NASICON	14
1.2.2	Thermal Properties of NASICON	25
1.3	Background and the Present Work	31
1.4	Thesis Outline	48

CHAPTER TWO: THEORETICAL CONSIDERATIONS 50

2.1 Theoretical Models of Ionic Conductivity 50

2.2 Methods of Synthesis and thermal Analysis 56

2.2.1 Solid State Synthesis 57

2.2.2 Thermal Analyses Techniques 61

2.3 Structure and Physical Properties of NZP 65

2.3.1 Defect Structure and Ionic Substitution 70

2.4 X-ray Powder Diffraction 74

2.4.1 Determination of Structure of NZP 79

2.4.2 Determination of Density and Crystallite Size 82

2.4.3 Scanning Electron Microscopy 83

2.5 Arrhenius Conduction 85

2.5.1 Impedance Spectroscopy 89

2.5.2 Frequency Dependence of Conductivity 103

2.5.3 Impedance Spectroscopy using the GHz Technique 105

CHAPTER THREE: MATERIALS AND METHODS 109

3.1 Sample Preparation and Synthesis 109

3.2 Structure, Microstructure and Phase Characterization 112

3.3 Arrhenius Conductivity and Impedance Spectroscopy 113

CHAPTER FOUR: RESULTS AND DISCUSSIONS 119

4.1 Thermal Analyses 116

4.2 Phase, Structure and Lattice Constants Determination 126

4.3 Microstructure Determination 139

4.4 Impedance Spectroscopy 145

4.4.1 Arrhenius Conductivity 160

CHAPTER FIVE: SUMMARY, CONCLUSION AND RECOMMENDATIONS 165

5.1 Summary and Conclusion 165

5.2 Future Work 170

5.3 Recommendations 172

REFERENCES 174

APPENDIX A 190

APPENDIX B 197

APPENDIX C 198

APPENDIX D 199

APPENDIX E 200

APPENDIX F 201

APPENDIX G 202

APPENDIX H 203

APPENDIX I 204

APPENDIX J 206

LIST OF TABLES

		PAGE
Table 2.1:	Comparison of electrical conductivity of different materials	88
Table 3.1:	Mass equivalents in grams of starting materials used for the preparation of $Na_{1-x}Li_xZr_2(PO_4)_3$	110
Table 4.1:	Summary of X-ray diffraction results for $Na_{1-x}Li_xZr_2(PO_4)_3$(x =0.00-0.75) and similar comparative compositions	131
Table 4.2 :	Summary of the bulk(σ_b) and total (σ_t) electrical conductivities and activation energies E_a of the investigated compositions at selected temperatures as deduced from the Arrhenius data	162
Table 4.3:	Summary of bulk (σ_b), total (σ_{tot}) electrical conductivities at selected temperatures and their activation energies (E_b, E_{tot}) for different NZP compositions, compared with sample from the present work, $Na_{0.25}Li_{0.75}Zr_2(PO_4)_3$	164

LIST OF FIGURES

		PAGE
Figure 1.1:	Processed NZP components	46
Figure 2.1:	View of the rhombohedral *R*3*c* structure of NASICON showing (ZrP_3O_{12})-units parallel to c axis and Na+ ions in Na1 positions(interstitial) octahedrally coordinated by O_2- ions. The Na1 positions are also octahedrally coordinated by empty Na2 positions in the same basal planes as the nearest-neighbour O_2- ions	66
Figure 2.2 (a-d):	(a) Corner shared ZrO_6 octahedra and PO_4 tetrahedra in the NZP structure. The brightness of the polyhedron face illustrates the distance to the viewer (Chene, 2003); (b) simple monoclinic unit cell with $a \neq b \neq c$ and $\alpha = \gamma = 90° \neq \beta$; (c) simple Triclinic unit cell with $a \neq b \neq c$ and $\alpha \neq \beta \neq \gamma \neq 90°$ and (d) simple Rhombohedral unit cell with $a = b = c$ and $\alpha = \beta = \gamma \neq 90°$	67
Figure 2.3:	(a) Schottky defect in NaC_l and (b) Frenkel defect in AgCl.	71
Figure 2.4:	(a) Cubic atomic arrangement for NaCl and (b) the migration of Na ion in the lattice, showing Na ion vacancy	72

Figure 2.5 (a): Direct Interstitial jump and (b) Interstitialcy mechanism in AgCl 72

Figure 2.6 (a): Vacancy and Interstitial atom and (b) Interstitialcy mechanism showing two possible locations of ions after movement 74

Figure 2.7: Each atom has six 1/6 atoms at each of top and bottom layer, two half atoms at top and bottom layer and 3 full atoms at the middle layer. Therefore each HCP unit cell has (2 x 6 x 1/6) + (2 x ½) + 3 = 6 atoms (a) schematic of the crystal structure (b) hard-sphere model (c) isolated unit cell schematic 79

Figure 2.8 (a-c): Geometrical dimensions of the hexagonal cell 80

Figure 2.9: Summary of the various signals obtained by interaction of electrons with matter in an electron microscope 83

Figure 2.9.1: SEM image of metal foam structure 85

Figure 2.9.2: The Arrhenius conductivity plots for different materials at Different temperatures 88

Figure 2.9.3 (a): A typical Nyquist plot for a polycrystalline material.

The real and imaginary components of impedance are plotted as parametric functions of frequency 92

Figure 2.9.3 (b): Equivalent circuit model of a polycrystalline material

in which components in parallel have been lumped together 92

Figure 2.9.4: "Brick Layer" Model of a polycrystalline material.

Grains are assumed to be cube-shaped, and grain boundaries to exist as flat layers between grains 93

Figure 2.9.5: Typical equivalent circuit (a) and corresponding impedance spectrum (b). The values of $R_1 R_2$ and R_3 depicted in figure 2.9.5(a), represents the resistance of the electrode reactions, grain (R_g) and grain boundary (R_{gb}), respectively 97

Figure 2.9.6: Comparison of equivalent circuit and impedance plot, a) parallel circuit consisting of a bulk electric resistance R_B and capacitance C_B, b) impedance plot for a single capacitance) and c) typical equivalent circuit which contain the contribution of ionic conduction at interface region 99

Figure 2.9.7: Central conductor and the coaxial line as sample holder (a) and the coaxial line represented as three T-matrices corresponding to 3 cascaded two- port networks (b). T_x is a matrix describing the sample, for an equivalent circuit 107

Figure 3.1: The X-ray difractometer used, version MD-10 112

Figure 3.2: Impedance spectrometer set-up operating in the frequency range 300 kHz-3 GHz 115

Figure 4.1: DTA plot of sample x=0.00 showing the exothermic peak at 461.9K(188.9°C) 116

Figure 4.2: TGA plot of of the powde mixture of sample x=0.00 showing the four temperature ranges for mass losses 118

Figure 4.3: DTA plot of powder mixture of sample x=0.25 showing the exothermic peak at 473K (200.0°C) 119

Figure 4.4: TGA plot of powder mixture of sample x=0.25 showing the four temperature regions of mass losses 120

Figure 4.5: DTA plot of powder mixture of sample x=0.50 showing the exothermic peak at 469.4K (196.4°C) 121

Figure 4.6: TGA plot of sample x=0.50 showing the four temperature regions of mass losses 122

Figure 4.7: DTA plot of powder mixture of sample x=0.75 showing the exothermic peak at 475.6K (202.6°C) 123

Figure 4.8: TGA plot of sample x=0.75 showing the four temperature regions of mass losses 124

Figure 4.9 (a): XRD patterns of Sintered sample x =0.00 with additional phases of ZrO_2 and $NaPO_4$ 126

Figure 4.9 (b): XRD pattern of sintered sample x=0.25 with only one phase, ZrO_2 128

Figure 4.9 (c): XRD pattern of sintered sample x=0.50 with additional phase of, $Na_5Zr(PO_4)_3$ 129

Figure 4.9 (d): XRD pattern of sintered sample x= 0.75 with additional phase of $Na_5Zr(PO_4)_3$ 130

Figure 4.9.1(a): Composite XRD patterns of sintered samples of $Na_{1-x}Li_xZr_2(PO_4)_3$ on the same scale for x=0.00-0.75 132

Figure 4.9.1(b): Relative value (with respect to PDF-2:33-1312) of lattice parameter a plotted against the XRD determined lattice parameter and theirerror bars for sample x=0.00 134

Figure 4.9.1(c): Relative value (with respect to PDF-2:33-1312) of lattice parameter c plotted against the XRD determined lattice parameter and their error bars for sample x=0.00 134

Figure 4.9.1(d): Variation of unit cell volume versus composition and the error bars for sample x=0.00-0.75 136

Figure 4.9.1(e): Plots of experimentally determined lattice parameters a and c against (x) with error bars for samples x=0.00-0.75 136

Figure 4.9.1(f): Variation of density with composition and error bars for sample x=0.00-0.75 138

Figure 4.9.2 (a): Micrograph of sintered sample x=0.00 with liquid–like phases and well formed crystallites at the top left corner 140

Figure 4.9.2(b): Micrograph of sintered sample x=0.00 at lower magnification with liquid–like phases 140

Figure 4.9.2(c): Micrograph of sintered sample x=0.25 at higher magnification showing well formed grains of different sizes and virtually no porosity 141

Figure 4.9.2(d): Micrograph of sintered sample x=0.25 at lower magnification showing large grains 141

Figure 4.9.2(e): Micrograph of sintered sample x=0.50 at higher magnification with large grains and fairly uniformly sized and no porosity 142

Figure 4.9.2 (f): Micrograph of sintered sample x=0.50 at lower magnification showing distribution of sizes in grains and some porosity 142

Figure 4.9.2 (g): Micrograph of sintered sample x=0.75 at higher magnification with fairly large grains 143

Figure 4.9.2 (h): Micrograph of sintered sample x=0.50 at higher magnification 144

Figure 4.9.3(a): Complex impedance plots at 500K showing the frequencies at the maximum imaginary impedance z'' at 2.7MHz and 100MHz for the grain boundary and bulk repectively 146

Figure 4.9.3(b): Complex impedance plots at 500K showing the frequencies at the maximum imaginary impedance z'' at 13MHz and 520MHz for the grain boundary and bulk repectively 146

Figure 4.9.4: Plot of sintered sample x=0.50 showing the real part of conductivity σ' versus frequency f and the frequency independent and dispersion regions 149

Figure 4.9.5: Complex conductivity plots at different temperatures 400K (a), 500K (b) and 590K (c) for composition x=0.75. The arrows point to the bulk (σ_b) and total conductivities (σ_{tot}) respectively 151

Figure 4.9.6(a): Complex impedance plots of x=0.75 at temperatures 400K
A reduction in the values of the real and imaginary parts
of impedance is also observed with increasing temperature.
R_b, Q_b are the resistance and capacitance and ρ_b, ρ_{gb}
and ρ_{tot} are the bulk, grain boundary and total ressitivity
(*intrinsic impedance*) 152

Figure 4.9.6(b): Complex impedance plots of x=0.75 at temperatures 500K.
A reduction in the values of the real and imaginary parts
of impedance is also observed with increasing temperature.
ρ_b, ρ_{gb} and ρ_{tot} represent the bulk, grain boundary and
total ressitivity (intrinsic impedance) 153

Figure 4.9.6(c): Complex impedance plots of x=0.75 at temperatures 590K
A reduction in the values of the real and imaginary
parts of impedance is also observed with increasing
temperature. ρ_b, ρ_{gb} and ρ_{tot} are the bulk, grain boundary
and total ressitivity (intrinsic impedance) 154

Figure 4.9.7: Plot of real part of conductivity σ' versus frequency f
for sample x=0.75 between 450 and 590K 155

Figure 4.9.8(a): Plot of frequency dependence of real part of conductivity at 500K for sample x=0.00 showing the fall in conductivity at high frequencies 157

Figure 4.9.8(b): Plot of frequency dependence of real part of conductivity at 600K for sample x=0.00 showing the fall in conductivity at high frequencies 157

Figure 4.9.9: Arrhenius plot of sintered samples $Na_{1-x}Li_xZr_2(PO_4)_3$ (x=0.00-0.75) showing the bulk (σ_b) and total conductivity (σ_{tot}) at different temperatures 160

LIST OF APPENDICES

		PAGE
APPENDIX A:	GLOSSARY	190
APPENDIX B:	XRD powder diffraction data for x =0.00 sample, hkl values and d-spacings	194
APPENDIX C:	XRD powder diffraction data for x =0.25 sample, hkl values and d-spacings	195
APPENDIX D:	XRD powder diffraction data for x =0.50 sample, hkl values and d-spacings	196
APPENDIX E:	XRD powder diffraction data for x =0.75 sample, hkl values and d-spacings	197
APPENDIX F:	Crystallite sizes for compositions x=0.00-0.75	201
APPENDIX G:	Specimen data for diffrentail thermal analyses	202
APPENDIX H:	Specimen data for thermogravimetric analyses	203
APPENDIX I:	Specimen data for Impedance Spectroscopy	204
APPENDIX J:	Specimen data for dc conductivity	206

CHAPTER ONE

GENERAL INTRODUCTION

1.1 Ionic Materials

Over the years ionic materials have become part and parcel of our electronic industry, as they complement the electronically-based semiconductor devices, based on their potential as renewable energy sources, low cost, environmental friendliness, abundance, flexibility and potential applications (Wang and Zhou, 1998). The materials may be insulators, amorphous or polycrystalline in nature and at high temperatures (Sakuma *et al*, 2006) a sublattice of the ions become delocalized and free to move, within the free empty sites. This provides free ions for electrical conduction under an applied electric field. The mobile ions are generally Na^+, Li^+, Ca^{2+}, or H^+, among others. Hydrogen ion conductors however, have been treated as a separate field due to their different conduction mechanism.They are very important for applications in intermediate temperature Solid Oxide Fuel Cells (Othman *et al*, 2007; Park *et al*, 2010). Most mobile ions are monovalent (due to reasons of Coulumbic interactions with the anionic lattice), however, recently a trivalent cation conducting Gadolinium ion (Gd^{3+}) has been reported with conductivity value in the application range, but at high temperature of 873K (Tamura *et al*, 2008). An ionic conductor is described as 'superionic ' when the conductivity attained is of the order of liquid electrolytes or their melt at room temperatures. This state of affairs is normally associated with a phase transition to a structural state favourable for ion motion. The avalanche in the number of the ions with increase in temperature is exponential, as observed in semiconductors. In the literature, materials of high ionic conductivity have been described variously as

superionic conductors, 'solid electrolytes' or 'fast ion conductors'. The transport properties of ionic materials depend critically on their microstructure. This is characterized by the geometrical shapes, spatial arrangements and relative amount of microstructural components, such as grains, pores, second phase particles and various interfacial boundaries (Ciobanu *et al*, 1999; Kidner, 2005). The differences in structure in these materials results in conduction mechanisms differing significantly. Attempts have been made to develop appropriate theoretical models to explain their conductivity mechanisms suitable for each structure. In this era of nanotechnology, it is noteworthy that the current trend in the miniaturization of devices has also spun a lot of research in the field of nanoionics (Maeir, 2005; Bellino *et al*, 2005; Mitchell, 2005) and thin films (West *et al*, 2004; Furasawa, 2006). This is expected to open new vistas of opportunity for applications in the field of nanotechnology. For example, NASICON thin-films of nanocrsytalline microstructure fabrication have been reported (Lessing and Huestis, 2006). The fabrication of thin films of these materials is necessary in order to reduce their resistance. There are several challenges being faced in the characterization of these materials, one of which is how to reduce the conducting temperature to ambient conditions so that they can be favourable for applications (they are currently applied mostly in high temperature devices), together with an understanding and development of the appropriate theoretical models to explain their superionic character from the microscopic point of view. Moreover, there is also the problem of optimization of the synthesis conditions in order to produce materials of the desired physical and chemical characteristics that would be suitable for applications. This is a consequence of their diverse applications in energy storage as rechargeable lithium ion batteries for laptop computers, mobile phones, electrodes, electrolyte materials, catalysts' supports and mirror blanks for space

technology (Vithal *et al*, 2000; Brunet *et al*, 2003), to name but a few. For application as electrolytes for example, the materials should have high room temperature ionic conductivity, transference number (ratio of ionic to electronic conductivity) close to 1 and temperature stability, among others (Sadoway and Mayes, 2003; Kartini *et al*, 2004; Pasciak *et al*, 2005). The high ion conductivity for solid electrolytes has been found to be rather unusual at moderate temperatures (293-573K), thus most ionic solids show certain ion localization and therefore very low conductivity. Their room temperature conductivities have been quoted as 10^{-2}-10^{-6} S/cm (Anantha, 2004) and 10^{1}-10^{-6}S/cm (Vitioo, 1999). When used as electrode materials, they should have mixed conduction properties, i.e. electronic and ionic. The conductivity of superionic conductors approaches that of liquid electrolytes at high temperatures and this is the point at which they become useful and applicable. Their conduction mechanisms is such that the mobile ions migrate between empty sites in the sublattice of the immobile ions. Further, they are characterized by both the liquid–like disorder structure of the mobile ions and the crystalline structure of the immobile ions (Shimojo, 2006). The superionic phenomenon has been reported in the planets Neptune and Uranus, where it was observed that at low temperatures the phase diagrams of water and ammonia exhibit a superionic solid phase between the solid and ionic liquid (Cavazzoni *et al*, 1999).

Various attempts have been made to realize the high ionic conductivity of solid electrolytes at ambient temperatures. Some of which include: (a) stabilization of open channel structure by substituting different cations or anions in AgI and CuI, (b) dispersion of insoluble, insulating, fine particles of oxides like Al_2O_3, SiO_2 into ionic matrices such as AgI or LiI, (c) formation of polymer-metal salt complexes, and (d) glassy electrolytes (Anantha, 2004).

There are many different categories of ionic materials, such as solid, glassy, polymer (Gimenez and Arves, 1999; Siekerski *et al*, 2006) and biopolymers, which show evidence of superionic conduction properties in gum Arabica (Mallick and Sarkar, 2000). The solid nature gives them good advantage over the liquid electrolytes. Glassy materials have become very important superionic conductors of recent and have been widely studied due to their potential applications and the high conductivity that can be attained (Sadoway and Mayes, 2003; Kartini *et al*, 2004; Pasciak *et al*, 2005; Sumiata *et al*, 2005). For example, it has been observed that the conductivity of glassy ionic materials are enhanced on introduction of a crystalline phase into the superionic glass matrix (Nowinski *et al*, 2006). The high conductivity in superionic conductors has been attributed to thermal activation, which is sometimes associated with phase transitions to a structural state that enhances conductivity by several orders of magnitude. This structural phase change could be related to particle size (Sumiata *et al*, 2005), pressure, density and microstructure, which also affect the electrical performance of the materials. In this study, the family of ionic conductors called NASICON (sodium superionic conductor) (Dongare *et al*, 1992; Brown, 2004; Naik *et al*, 2004) have been investigated. The materials possess high ion conductivity, high radiation and corrosion stability, among others, hence their use as refractory materials in the car and space industries, among others (Vladislav *et al*, 2002; Aboulaich, 2009).

1.2 Literature Review

The literature survey concentrated mainly on studies on synthesis, thermal, structural, electrical conductivity and impedance spectroscopy characterization, and analyzed the problems, challenges and interpretations and provided data on the materials. The review begins with electrical properties of NZP (sodium zirconium phosphate) and NASICON materials and other related ionic conductors.

Forsyth *et al* (1998) carried out studies on lithium conducting $Li_{1.3}Al_{0.3}Ti_{1.7}(PO_4)_{3-x}$(Z=V, Nb) system (LATP), and reported that Gromov *et al* substituted V and Nb for phosphorus and observed an increase in the conductivity of the system. The nature of the electrodes was crucial in resolving the grain boundary arc in the Cole-Cole plot (imaginary versus real impedance plot), as evidenced from their comparison of graphite, silver and gold electrodes, as well as their combinations in order to obtain well defined impedance arcs. They further observed that graphite alone was too resistive and tended to dominate the impedance values, whilst silver ink did not produce good adherent electrodes, even though the film resistance was quite low. The best electrodes were obtained by a combination of sputtered gold layer over which a silver ink was applied. Evidence of large porosity was found implying that sintering was incomplete and a large grain boundary resistance was inevitable. Similarly, Lessing and Huestis (2006) in their study of nanocrsytalline thin films of NASICON compositions, reported the case where a thick grain boundary whose resistance (possibly due to pellets that were not fully densified) dominated the imaginary Z'' component of the impedance spectrum, which comprised the major component of the electrical resistance of the samples.

It has been demonstrated in the study of $Li_{1+x}[Al_xGe_{2-x}(PO_4)_3$ glass ceramics, that heat treatments with shorter nucleation times lead to higher grain size and subsequently higher ionic conductivity (Cruz and Rodriques, 2007). Furthermore, a correlation is found to exist between the extent of sintering and total conductivity, as demonstrated by Kang and Cho (1999) in their study of two NASICON compositions. Previous reports showed that the substitutions investigated in their work lead to an increment in densification, attributed to the extra intergranular low melting or glassy phases which can act as fluxes to improve sinterability and connectivity. Forsyth *et al* (1998) have shown that Lithium-ion conducting ceramics (the LATP–Lithium Aluminum Titanium Phosphate system) and glasses, have advantage over polymer based systems because their conduction can be solely attributed to the lithium species. In addition, high room temperature conductivities (up to $1x10^{-3}$S/cm) have been reported, including reports that the ionic conductivity could be altered by controlling the channel sizes via one or more substitutions (Al, Sc, Nb and V), the lattice dimensions being dependent on the size of the structural cations.

Using NMR technique, it is possible to predict changes in ionic conductivity by measuring the mobility (Arbi *et al*, 2002) of lithium ions in these materials through ^{7}LiNMR. With increasing V content the ^{7}Li static line width was found to steadily increase, indicative of decreasing lithium ion mobility (Forsyth *et al*, 1998). The authors, predicted that V substitutions in LATP will not enhance the bulk conductivity of the electrolyte.

A study has been reported by Nian Xu *et al* (2004), on lithium ion conductor with composition Li_xMPO_4 (M=Mn, Fe, Co, Ni). The experiment was carried out in

Argon (Ar) atmosphere using a 4-probe conductivity measurement. The higher sintering temperature of the sample at 1123K ensured higher sample density. The samples exhibited highest absolute value of conductivity at a given temperature. Three of the undoped samples showed different values of conductivity, and were attributed to the measurement method. This suggest that differences in the absolute values of carrier concentration may be due to heat treatment conditions. Activation energies for all samples were within 0.39-0.50eV, pointing to a common mechanism of conduction due to its narrow range. The use of blocking electrodes in dc measurements made the conductivity predominantly electronic.

Salkus *et al* (2006a) studied the compounds $LiM_2(PO_4)_3$, where (M=Ge, Zr, Ti) that belonged to the NASICON-type structure. They found that ionic conductivity of the system was greatly enhanced when Zr^{4+} in the $LiZr_2(PO_4)_3$ was replaced by a smaller Ti^{4+} ion, since the tunnels in the $LiTi_2(PO_4)_3$ were more suitable in size for the Li ion migration. Partial substitutions of Ti^{4+} by Sc^{3+} and Cr^{3+} ions in the NASICON-type structure of $LiTi_2(PO_4)_3$ is known to also cause an increase of the value of the Li ion conductivity of the substituted systems. Substitution of Zr^{4+} by Ti^{4+} and trivalent ion Sc^{3+} in the $LiZ_2(PO_4)_3$ compound caused a drastic increase of conductivity σ at room temperature, in comparison with the values of ionic conductivity of $Li_{1+x}Zr_{2-x}Ti_x(PO_4)_3$ compound. The authors computed the room temperature values of σ for $Li_{1+1.2}Sc_{0.6}Z_{0.6}Ti_{1.6}(PO_4)_3$ as 1.2 $x10^{-2}$ S/cm, and was found to increase with temperature. The activation energy was E_g= 0.33eV. Further, they observed two dispersion regions in all the investigated samples, a high frequency part, attributed to the relaxation time in grains, and a low frequency part, corresponding to grain boundary processes which were thermally activated. There was also an observation of the shifting of the dispersion regions towards higher

frequencies with increase in temperature. It should be pointed out that the crystal structure of $LiZr_2(PO_4)_3$ depends on technological condition of its preparation. For example, the X-ray pattern of $LiZr_2(PO4)_3$ prepared at 1323K-1373K greatly differs from rhombohedral, and is thought to possibly correspond to a triclinic cell (Salkus *et al*, 2006a), figure 1.3c. At room temperature the values of the ionic conductivity of $LiZr_2(PO_4)_3$ is lower than 10^{-7}S/m.

An impedance spectroscopy study by Nga and Son (2004) of NASICON in aqueous solution (0.1M NaCl for different times), modeled the equivalent circuit and used the ion exchange method in the synthesis. They distinguished three semicircles with the first at high frequency 3-42kHz (HF), attributed to the bulk electrical properties of the material, and because of inhomogeneity of the sample, since it did not show an ideal semicircle shape but a flattened one. The second one at medium frequency 0.5Hz-3kHz (MF) was thought to be contributed by the NASICON/solution interface process, which was also not a perfect semicircle and became flatter when the ion exchange time increased. The third semicircle at low frequency 10mHz-0.5Hz (LF) was generally assigned to slow transport processes such as diffusion. The authors found that the bulk resistance increased while the bulk capacitance decreased, when ion exchange time increased. This was ascribed to the leaching of Na^+ ions from NASICON, with resulting increase in charge carrier concentration of electrolyte.

In his study, Dong-mei *et al* (2006) synthesized NASICON through hot-press sintering to prepare $Na_3Zr_2Si_2PO_{12}$ ceramics, using the sol-gel method. The results showed that the samples contained mainly monoclinic NASICON and no ZrO_2 phase was found, no matter the sintering temperature. At the sintering temperature of 1423K for example, they observed that ionic conductivity of the sample had the highest value

of $3.6x10^{-3}$S/cm. They attributed it to its having the highest density and the least grain boundary, due to the large crystal size of the ceramics. Recently, a variant of the sol-gel method has been reported, the so-called 'drop generation' method. This is said to overcome limitations due to conventional compacting method of ceramics, leading to structural modifications as a result of variations in size, density and non uniformity in shape, caused by the processing parameters (Judes and Kamaraj, 2009).

A comparison of sintering techniques has been studied by Lee *et al* (2004a) on NASICON compounds through solid state reaction, by sintering them using *Spark Plasma Sintering* (SPS) (uses microscopic electrical discharges between the particles under pressure, which allow quick densification to almost the theoretical density) and conventional sintering (CS). The SPS gave dense materials with high electrical conductivity at relatively low sintering temperature of 1373K, while highest conductivity of $1.8x10^{-3}$S/cm was achieved for the stoichiometric SPS composition, a value they emphasized was comparable to the best results reported in literature, $2.0x10^{-3}$S/cm. Specifically, two NASICON compositions were compared, $Na_3Z_2S_2PO_{12}$ and 5Na5P (5% excess of Na and P) and they observed two distinct regions: a straight line at low frequency, representing an electrode–ceramics interface phenomenon, and a semicircle associated with the grain boundary. The high frequency arc has been attributed to bulk effect and could not be well distinguished or observed in some cases. Though in principle, the bulk contribution could be determined by extrapolating the grain boundary semicircle, even in the absence of a high frequency arc. However, they could not determine precisely the bulk resistance due to the inevitable inductance contribution from the lead wire. Since the grain boundary resistance contributed to the total resistance, the evaluation of bulk resistance was also difficult. The total resistance of the NASICON ceramics was

therefore determined from the intercept of the electrode and grain boundary arc. In addition, the sample from low temperature sintering had visible grain boundary arc, while the bulk contribution could only be estimated from the high frequency intercept of the grain boundary arc. With increasing temperature, the grain boundary arc became smaller and the grain arc became more visible. The dc conductivity of the samples was calculated using the bulk resistances determined from the complex plots. With increment of sintering temperature, the dc conductivity improved and reached 5.64 $x10^{-3}$S/cm at 1423K, higher than the reported results. For the sintered NASICON ceramics, the impedance from the grain boundary dominated, as the crystals from these samples were very small. Density of sample sintered at 1273K was the lowest and crystal size the smallest, thus the impedance from the crystal boundary was the highest and the ion conductivity of the sample the lowest. It has similarly been reported that long periods (55h) of high-energy ball-milling is as effective as Spark Plasma Sintering in improving conductivity (Vijayan, 2009).

A study of the effect of different Zirconia precursors on the electrical properties of NASICON (Fuentes *et al*, 1999) has also been reported in which the compositions are NASICON-$Na_3Si_2Zr_2(PO_4)_3$ and NASICON-TZP ($Na_3Zr_{1.94}Y_{0.06}Si_2PO_{12}$). The NASICON was found to exhibit different grain sizes and the presence of a liquid phase was confirmed, suggesting the effect of high sintering temperature, which can lead to low temperature ion–blocking phenomenon. It was found necessary to carry out low temperature measurements at 273K in order to distinguish the bulk from the grain boundary contribution, for both the NASICON and NASICON-TZP due to the higher impedance of the NASICON pellets. However, even at this temperature, only the grain boundary arc was clearly seen and the bulk contribution had to be estimated from the high frequency intercept of the grain

boundary arc, in the case of the NASICON. The NASICON–TZP was also found to have the advantage of sintering to full densification at lower temperatures. The computed conductivities and activation energies for the NASICON and NASICON-TZP were respectively, 4. x10^{-4}S/cm with activation energy of 0.39eV, and 2.1x.10^{-3}S/cm corresponding to activation energy of 0.36eV at room temperature.

Studies of zirconia precursors (Fuentes *et al*, 1999; Tarnopolsky *et al*, 2003) have also been reported in which it was found, in the case of hydrated and nanocrsytalline zirconia, that ion conductivity of the hydrated zirconia could be increased by thermal treatment by one order of magnitude or more. Salkus *et al* (2006b) studied lithium conducting NASCON-type materials. $LiM_2(PO_4)_3$ (where M=Ge, Zr, Ti) and synthesized $Li_{1.3}\square_{1.7}Sc_{0.3}Ce_{1.7}(PO_4)_3$ by solid state reaction method. The square indictaes the amount which was replaced by Sc (Scandium). Three dispersion regions were found in the conductivity (σ) spectra which all shifted toward higher frequencies with increase of temperature. The low frequency dispersion regions were attributed to the blocking Pt electrodes and the complex conductivity plots show that the higher frequency part of the spectrum correspond to the relaxation in grains, while the lower frequency part correspond to grain boundary processes. At 650K the values of total conductivity (σ_t) and grain conductivity (σ_g) of the investigated ceramics were found to be σ_t = 8.59 x10^{-4}S/m and σ_g=1.95 x10^{-3}S/m respectively, with corresponding activation energies for the total and grain conductivity given as E_t=1.34eV and E_g =0.73eV respectively.

488600

The study by Mouahid *et al* (2001) of lithium conductivity in the system $LiTi_2(PO_4)_3$ (~10^{-6}S/cm at room temperature) found that the conductivity may be increased from this value by at least two orders of magnitude upon partial substitutions of Ti^{4+} by trivalent cations such as Al, Ga, In, Sc,Y,La,Cr or Fe. The increase of ionic conductivity was due to a higher charge carrier number which they attributed to the lower porosity of the pellets. The conductivities of $Li_{1+x}Ti_{2-x}Al_x(PO_4)_3$ materials on the other hand, could be as high as 10^{-3}S/cm at room temperature. They argued that this could mean that the ionic radius of Al^{3+} was likely to lie within the tolerability limit of the NASICON framework, and that the maximum amount of Titanium that could be replaced with Al^{3+}, with the concomitant insertion of Lithium to balance the charges, was 0.4 per formula unit. The experimental results indicated clear blocking phenomena at grain boundaries and electrode characteristics of ionic conductors. The complex impedance plots at high temperatures showed well developed spikes characteristic of blocking electrodes which were observed at low frequencies. At lower temperatures, they observed a depressed semicircle which they suggested might be related to the presence of a second semicircle at lower frequencies due to partial blocking of the grain boundaries. The grain boundary contribution probably resulted from the relatively low pellet density, an indication of a very good connectivity between grains, resulting from small amount of Li_3PO_4 impurity phase acting as an intergrain binder. Oda *et al* (2007) have studied Lithium ionic conductive solid electrolyte based on the NASICON–type $Li_{1+x}Ga_xTi_{2-x}(PO_4)_3$ (x=0.1-0.9), and obtained a maximum conductivity of $7.3x10^{-4}$S/cm at 303K and activation energy of 0.30eV, for $Li_{1+1.25}Ga_{0.25}Ti_{1.75}(PO_4)_3$. Addition of Li_3PO_4 or TiO_2 as binder did not increase the conductivity in all the samples, rather they became lower. They thus argued that it is an indication that these materials have no effect on the values of the

measured parameters, even though such phases might be present in the synthesized materials.

Anantharamulu *et al* (2008) have also studied new NASICON-type materials of composition, $Li_{3-2x}Al_{2-x}Sb_x(PO_4)_3$ (x = 0·6 to 1·4) and their dc conductivities. Impedance studies carried out at different frequencies and temperatures showed Arrhenius behaviour for all compositions. The Cole–Cole plots obtained from impedance data do not show any spikes on the lower frequency side, indicating negligible electrode effects. A maximum conductivity of $4{\cdot}5 \times 10^{-6}$ S cm^{-1} at 573 K was obtained for x = 0·8, for the $Li_{3-2x}Al_{2-x}Sb_x(PO_4)_3$ system. The complex impedance plot did not show semicircles up to 323K but as the temperature increased the curves attained greater curvature and became perfect semicircles, terminating at the origin, an indication of the absence of series resistance in the equivalent circuit model of the sample. All the semicircles started on the real impedance axis at the lowest frequency, and this point was found to decrease with increase in temperature. Frequency variation of conductivity showed two shapes at all temperatures of the measurements. The authors therefore suggested that the low frequency and low temperature conductivity could be due to intrinsic defects and charge accumulation in the sample, therefore the variation of slope with conductivity plots at lower frequencies was an indication of presence of such defects. Khatri *et al* (2008) carried out impedance study on the system $Ba_3V_2O_8$, and found a systematic appearance and disappearance of the impedance arcs. At lower temperature, a single arc appeared which was attributed to grain interior of the material. However, at high temperatures, another arc appeared, and the spectrum comprised of two semicircular arcs, with their centres lying below the real axis. The high frequency semicircular arc was attributed to the bulk properties. However, with subsequent rise in temperature, both the grain

and the grain boundary phenomena appear to merge in to a single arc, suggesting a substantial modification in the overall electrical behavior of the material. Furthermore, the variation of real component of impedance Z' with frequency, from which the relaxation frequencies were calculated, showed shifts in their peaks to higher frequencies on increasing temperature (relaxation frequency is the frequency at the maximum impedance value). There is delailed analyses of the concept in the chapter on theoretical considerations (chapter two). This suggests the occurrence of relaxation in the system. Peak broadening was also observed, suggesting relaxation, a result of the presence of immobile species at low temperatures and defects at higher temperatures. Similarly, the imaginary part of impedance was found to increase with rise in frequency, indicating that conduction is increasing with rise in temperature and frequency.

1.2.1 Synthesis and Phase Transitions in NASICON

When NASICON are sintered at high temperatures, their porosity become reduced. High sinter density and good mechanical strength are desired characteristics for enhancing the utility of these materials. Several efforts have been adopted to improve these properties, such as the use of grain growth inhibitors. There have also been attempts to alter the axial thermal expansion coefficients by proper ionic substitutions, which have helped in overcoming some of the problems to a great extent (Angadi *et al*, 2002). An advantage of NASICON over other materials used as solid electrolytes is their low sintering temperatures. That is the temperature required for fusion of the particles is lower, around 1273K. The most challenging problem faced in the solid state synthesis of the materials is the presence of certain amount of ZrO_2 second phase, and a monoclinic to rhombohedral phase transition that occurs at

1373K, below the usual sintering temperature of the NASICON. A further monoclinic to rhombohedral transition, around 473K causes a dilatometric anomaly unfavourable for applications. One suggesion to overcome such problems is through compositional modifications, as has been reported by Kang and Cho (1999). They emphasized the importance of choosing an appropriate sintering temperature and cooling rate, in order to produce sintered NASICON with less ZrO_2 and high electrical conductivity. The poor sinterability and phase purity limits the applications of NASICON in practical devices. A further problem faced in solid state synthesis of these materials at high temperatures is the volatilization of Na_2O and P_2O_5, and the resultant segregation of zirconia at the grain boundary. This is known to be responsible for the decrease in ionic conductivity observed (Kang Cho, 1999). Methods such as sol-gel synthesis, yittria doping and spark plasma sintering (SPS) technique, among others have been used to minimize the problem. The SPS technique, reported by Kang and Cho (1999), uses microscopic electrical discharges between the particles under pressure, which allow quick densification to almost the theoretical density. These enhancements have been observed in several metallic, ceramic and other systems. There is also the advantage of a relatively lower temperature and minimal grain growth, and has been applied to fabricate nanostructured materials (Kang and Cho, 1999).

Dong mei *et al* (2007) synthesized and studied NASICON $Na_{1+x}Zr_2Si_xP_{3-x}O_{12}$ (x=2) by hot-press sintering, using the sol–gel method. The XRD from the samples sintered showed peaks corresponding to the monoclinic NASICON phase and no ZrO_2 phase in any sample. The peaks of the samples sintered at 1273K were wider and lower than those of the samples sintered at higher temperatures, especially at 1423K, indicating that crystal size of samples sintered at lower temperatures was smaller than

that sintered at higher temperatures. The SEM micrographs also showed that the crystal in the sample sintered at 1273K was smaller than the others. There were also lots of pores in samples from low sintering temperatures, which decreased in both amount and size with increase in temperature. At 1423K, there were no pores at all and the crystals were larger, in agreement with the XRD results.

NASICON presents significant challenges to solid state Physicists, material scientists, inorganic chemists and materials' engineers, in terms of understanding of its complex structure; the lack of single crystals, most materials are polycrystalline, the art of producing single crystals is yet to be perfected, and the non stoichiometric nature of its composition. These various problems are being studied by various groups. An alternative being pursued is to develop new superionic conductors with simple structures, the so-called NASICON analogues, which are easier to synthesize. Superionic phosphates and silicates are in this group. A member of the group which has been reported recently (Gopalakrishna *et al*, 2005), and synthesized by the hydrothermal technique, is Potassium Iron (III) pyrophosphate ($KFeP_2O_7$). On the basis of its good ionic conductivity and low cost, rhombohedral $Li_3Fe_2(PO_4)_3$, a NASICON-type, is seen as a potential insertion electrode material in lithium polymer batteries. The rhombohedral phase is found to be unstable and when heated above 852K, turns into monoclinic modification (Xu *et al*, 2004). Although the phase remains stable upon cooling to room temperature, monoclinic $Li_3Fe_2(PO_4)_3$ exhibits several reversible phase transitions with temperature (Xu *et al*, 2004).

Phase transitions determine many properties of inorganic compounds, particularly of solid state ionic conductors, such as AgI and Li_2SO_4. For most of these materials high ionic mobility appears only after superionic phase transitions which

goes with sharp changes in the ordering of cationic or anionic sublattice. In other compounds on the contrary, a gradual growth of ion mobility with temperature lead to *second order phase transitions, accompanied by change in symmetry and properties of* crystals.

The NASICON structural family exhibits complex polymorphism (compounds having more than one crystal structure), and the materials with the highest ion mobility are usually rhombohedral. However, they can transform to triclinic phase at low temperatures, as observed earlier. Na and Li-based NASICON-type compounds have been thoroughly investigated. For example, a partial substitution of Zr^{4+} for tri- (Bi^{3+}) and pentavalent (As^{5+}) cations lead to lithium mobility increase, and favoured triclinic–rhombohedra phase transition in the material obtained. Heating of this material lead to the same changes, though there appears to be discrepancy between published data on the temperature of phase transitions.

Salkus *et al* (2006a) studied the powder of $Li_{1+x}Sc_xZr_{2-x}$ $(PO_4)_3$ (x=0.1-0.3) from the solid state reaction method and observed phase changes. The XRD pattern of $LiZr_2(PO_4)_3$ (LZP) prepared at 1323-1373K greatly differed from the rhombohedral and, they argued, possibly corresponds to a triclinic cell. At 1423-1473K, sintered LZP pellets belonged to a rhombohedral symmetry, depending on the temperature of synthesis, 1473K or 1173K, two different phases were obtained: the LZP prepared at 1473K showed a NASICON–type structure and a monoclinic-rhombohedral first order transition took place at a temperature of about 313K. The LZP prepared at 1173K however, exhibited the β-$Fe_2(PO_4)_3$-type structure and a monoclinic-orthorhombic transformation took place at 573K. Best *et al* (1998) studied Lithium Aluminium Titanium Phosphate (LATP) by the substitution of Vanadium (V), Aluminium (Al) and Niobium (Nb) in LATP ($Li_{1-x}Al_xTi_{2-x}(PO_4)_{3-y}(MO_4)_y$

(M=V,Nb,Y). Their XRD patterns were consistent with an R-3c unit cell, with slightly varying unit cell dimensions as a function of composition. Their spectra also confirmed that the reactions were complete, as there was no evidence of the presence of any starting materials. Only the peak at 25.6°, for example, was common to both the basic LATP structure and one of the starting materials, TiO_2. In all patterns there were however evidence of low peaks in the region 2θ=27-28°,which they argued had previously also been observed. The search to identify these peaks proved abortive. Analysis of some of the diffraction patterns indicated that V and Nb substitution caused only a slight increase in the cell volume compared with LATP.

Anantharamulu *et al* (2008) have studied $Li_{3-x}Al_{2-x}Sb_x(PO_4)_3$ (LASP) (x=0.6-1.4) using solid state reaction. All the compositions, except for x=0.6 and 0.8, were found to be single phase with no detectable impurities or unreacted starting materials. The d-lines for x=1.4 and 1.0 compositions, i.e. $Li_{0.2}Al_{0.6}Sb_{1.4}(PO_4)_3$, $Li_{0.6}Al_{0.8}Sb_{1.2}(PO_4)_3$ and $LiAlSb(PO_4)_3$, clearly suggested a hexagonal lattice for these phases. For x=0.8 and 0.6 compositions, majority of observed d-lines belonged to monoclinic phase NASICON. For instance, they observed that the two d-lines in the range 2θ=13-17° belonged to a monoclinic NASICON phase, and argued that these two compositions could be regarded as pure monoclinic phase due to intense peaks at 2θ=21,22,25,31 and 34°, which were due to the hexagonal NASICON phase, and the absence of low intense d-lines at 2θ=22-24° and 2θ=26-30°, corresponding to the monoclinic phase. The composition x=0.6 and 0.8 for example, were predominantly hexagonal with a trace of monoclinic phase. They therefore suggested that for x =0.6 compositions, the monoclinic phase may be formed with or without trace of hexagonal phase. The lattice constants for all the compositions were derived assuming hexagonal lattice. Attempts to prepare compositions with x<0.6 either resulted in melt

formation or mixture of unknown phases. Neither did heating the mixture at lower temperatures (1073K) for a very long time proved successful. Thus the phase formation range in their work for the LASP series was x=0.6-1.4.

Oda et al (2007) synthesized NASICON of composition $Li_{1+x}GaTi_{2-x}(PO_4)_3$ with x=0.1-0.9 by the sol-gel method at 1173-1273K for 6h air. They indexed the diffraction lines based on a rhombohedral structure with space group R-3c. For discs sintered at 1173K, single phase solid electrolytes were formed between x=0.0 and x=0.4, while impurity phases of $LiTiPO_3$ and $GaPO_4$ (hexagonal), rhombohedral appeared at high content ratio of x>0.5. For discs sintered at 123K single phase solid electrolyte was formed between x=0.25 and 0.35; on the other hand, when the discs were sintered at 1273K solid phase solid electrolyte was formed up to x=0.2; while the impurity phases of $LiTiPO_5$ and $GaPO_4$ (orthorhombic) appeared for x>0.4.

The TGA of the samples showed weight loss in the examined temperature ranges 373-673K which they attributed to the separation or loss of organics. In contrast, the DTA peak appeared around 873-973K,which were attributed to crystalization. All the other TGA-DTA curves were similar in shape for $Li_{1.2}Ga_{0.2}Ti_{1.8}(PO_4)_3$. The SEM micrograph for $Li_{1.3}Ga_{0.3}Ti_{1.7}(PO_4)_3$ sintered at 1173K, showed similar sized particles. The particle size was increased by increasing the sintering temperature and content of Ga^{3+}, though similarly sized particles were not observed. Lee *et al* (2004a), used spark plasma sintering (SPS) method to obtain dense NASICON ceramics with high electrical conductivity. This was compared with conventional sintering (CS). They obtained a well crystallised NASICON powder after calcinations at 1423K for 5h with presence of ZrO_2 detected. The conventional sintering at 1393K for 14h produced an almost single phase NASICON while

observing a reduction in the peak intensity of ZrO_2 after CS, suggesting that the solid state reaction during calcinations was incomplete. In contrast to CS, SPS gave a more intense ZrO_2 peak and this increased with increasing SPS temperature. The dominant existence of ZrO_2 was suspected to be caused by Na and P volatilization in a vacuum leading to the segregation of ZrO_2. The authors observed that the addition of excess Na and P resulted in significant reduction in the ZrO_2 content after SPS.

Fuentes *et al* (2004) synthesized $Na_3Zr_2Si_2P_3O_{12}$ by gel–combustion method. The SEM micrographs obtained for the samples showed that for low calcination temperatures and shorter calcinations periods, the morphology of the reactant mixture presents a glassy aspect. This suggests the formation of a liquid. It was speculated that the reaction of ZrO_2 with this liquid may lead to the formation of zirconium silicates or phosphates, as this was also highly probable at this temperature. They observed that increasing t_c up to 8h lead to large grains of a crystalline phase of composition similar to NASICON. These Ziconia crystallites were attributed to the precipitation of monoclinic Ziconia ($mZrO_2$) due to Na and P volatilization at high temperatures.

The XRD patterns show that NASICON was not formed at 1273K or lower. At 1373K, there was onset of low intensity NASICON peaks indicating the early stages of the formation reaction, which was significantly enhanced when temperature increased to 1573K. This was in full agreement with the EDX (Energy Dispersive Spectroscopy) results. There was a decrease in the reaction rates at high temperature for NASICON formation. Significant fractions of Na and P may also be lost by volatilization at temperatures above 1573K and the structure tends to release Zr^{4+} cations that precipitate as the oxide. They concluded that the formation of

NASICON occurred in a very narrow temperature range. Kang and Cho (1999) studied two NASICON compositions $Na_3Z_2Si_2PO_{12}$ (H-type) and $Na_{3.2}Zr_{1.3}Si_{2.2}P_{0.8}O_{10.5}$ (A-type) and correlated the effect of sintering temperature, time and cooling processes in the formation of phases like ZrO_2 and crystalline NASICON. The XRD curves obtained for the A-type samples sintered at 1473, 1533, 1573, 1593, and 1633K for 1h . respectively, showed all samples corresponding to either monoclinic NASICON or ZrO_2 phases. However, samples sintered above 1573K contained certain amount of ZrO_2 second phases. Due to air-quench, it was believed that considerable amount of ZrO_2 was in thermal equilibrium with the crystalline NASICON at 1613K.

Anna *et al* (2000) have shown that $Li_3Fe_2(PO_4)_3$ was found to adopt a rhombohedral symmetry which was metastable, and if heated above 843K, turned into monoclinic modification. This phase remained stable upon cooling to room temperature. Like the Na compound, monoclinic $Li_3Fe_2(PO_4)_3$ exhibited several phase transitions with temperature. The $Na_3Fe_2(PO_4)_3$ has monoclinic symmetry with space group C2/c, denoted by the α-phase, and it exhibited two reversible polymorphic phase transitions at 368K (α-β) and at 418K (β-γ), respectively.

Alexander Graham Bell discovered that a material generates an acoustic signal when illuminated with periodically modulated light. This is called the photoacoustic effect (PA).There has been interest in the method as an experimental tool in the studies of optical, thermal and spectral properties of liquid and solid state materials. The measured quantity in the photoacoustic technique is the pressure variation in the gas surrounding the sample. This is caused by transfer of heat from the sample to gas. The frequency of the signal is identical to that of the modulation. The dependence of

the photoacoustic parameters on the thermal properties of investigated materials permits the application of the PA technique in detecting those processes in which they are changed. Zurawaski (2006) has applied this technique successfully to some metals and metal alloys. In particular, it has been applied to the solid-solid (polymorphic) phase transitions in silver salts (AgI, Ag_2Se), which are superionic conductors. The temperature of phase transition for Ag_2Se, Ag_2S, determined from such measurements, agreed well with literature data on the superionic transition temperatures of these materials. Similarly, the smeasured temperature dependencies of the amplitudes of photoacoustic signals with control measurements from DSC(Diffrential Scaning Calorimetry), for Vanadium Oxide, for example, showed that the low temperature (340K) anomalies coincided well with the DSC endotherm. Also its position does not depend on the heating rate and is reproducible in the second and subsequent heating runs.

Naik *et al* (2004) studied sodium zirconium phosphate ($NaZr_2P_3O_{12}$), synthesized by heating mixture of Na_2CO_3, ZrO $(NO_3)2.5H_2O$ and $(NH_4H_2PO_4)$ in air in a resistance heated furnace and a microwave heating system respectively. The temperature range was 723-923K. The mixture heated for 1h in a resistance heated furnace at 723K produce a poorly crystalline NZP (sodium zirconium phosphate). Increasing the temperature to 923K produced a highly crystalline product. The same mixture heated in a microwave oven at 723K for 1h however, yielded the most crystalline NZP. Alternatively, when a mixture of (NaH_2PO_4), (ZrO_2) and (NH_4HPO_4) were heated in a resistance furnace at 923K for the same period, it did not react in air and did not yield the pure product at 723K when heated in microwave assembly for 1h.The first step in the TGA (room temperature-363K) had approximately three regions using the first method and corresponded to dehydration,

followed by the second (353-573K), nearly overlapping step which involved mass loss due to removal of nitrate groups and elimination of carbon dioxide from the mixture. In the DTA plot, the first peak was endothermic (393K) and corresponds to the elimination of water from the mixture. This was followed by two prominent peaks. A sharp peak at 523K followed by a broad one at 723K were attributed to the oxidation of evolved ammonia by zirconyl nitrate, followed by solid state reaction between the components to yield $NaZr_2P_3O_{12}$. The width of the second broad peak in the DTA plot was typical of solid-solid reaction and corresponded with the formation of NZP from ZrO_2, P_2O_5 and Na_2CO_3. The DTA results suggested that the formation of NZP from the reaction components was complete by 923K as the stability region was from 923-1073K.

Stennia *et al* (2006) studied ionic conductivity and phase transitions of lithium zirconium phosphates, $Li_{1\pm x}Zr_{2-x}M_x(PO_4)_3$, with NASICON structure, using XRD and calorimetry. Triclinic-rhombohedral phase transition in these materials occurred in a wide range of temperature together with the coexistence of both phases. They observed an unusual change of $LiZr_2(PO_4)_3$ lattice parameters with increasing temperature during the heating of the compound in which the lattice parameter 'a' significantly increased. Kumar and Yashonath (2002) using simulation studies, developed an interatomic potential that reproduces several known experimental data in excellent agreement with theory, such as the structural parameters, ionic conductivity (as function of both temperature and alkali ion content) and their site occupancy. The simulation provided valuable atomic energy level picture of a variety of phenomena such as the nature of the fast ion transport, phase transitions and low thermal expansivities of these solids. Maldonado-Manso *et al* (2005) studied nominal powder of $Na_{1.4}A_{l0.4}M_{1.6}$ $(PO_4)_3$ (M=Ge,Sn,Ti,Hf,Zr), prepared and studied by

Rietveld analysis of X-ray and neutron diffraction patterns. The result showed that the M=Ge and Sn crystallize in the R-3 space group and that the M=Ti,Hf and Zr compounds crystallize in the R-3c space group. The deduced aluminium contents and local atomic environments found that Aluminium contents in the NASICON phases were always smaller than the nominal ones. Electrical conductivity measurements and impedance spectroscopy analysis of samples with high Aluminium contents, i.e. M=Ge, Sn and Ti carried out showed that the Titanium sample had the maximum Aluminium contents and displayed the lowest activation energy (E_a= 0.512eV) and the highest conductivity at 400K, 1.5 x10^{-5}Scm^{-1}.

1.2.2 Thermal Properties of NASICON

Most ceramics expand on heating, due to increased thermal agitation of atoms and the subsequent increase of the bond lengths. There are some anisotropic thermal expansion ceramics that exhibit the opposite behaviour, i.e., contraction on heating. These structures will expand in one or two dimensions and contract in the other dimension (s). Examples of anisotropic materials are Al_2TiO_5, $ZrTiO_4$, eucryptite, cordierite, and NZP ($NaZr_2P_3O_{12}$). The problem with anisotropic materials is that microcracking occurs during the heating cycle, the thermal behaviour is characterized by *hysteresis* (a phenomenon observed, for example, in an ordinary piece of iron which might not have an overall magnetic moment, though magnetization can be induced in it by putting the iron in a magnetic field, thereby aligning the moments of all the individual domains; the energy expended in reorientaing the *domains* from the magnetized back to the demagnetized state manifests itself in a lag, known as *hysteresis*) loops, and by a much lower thermal expansion coefficient compared with dense ceramic (Kim and Kim, 2004). As the near zero thermal expansion of the anisotropic material minimizes thermal stress in a body, much effort has been focused upon developing low-expansion materials for severe thermal shock applications which is the rational approach to thermal stabilization of composites.

There are several studies on the thermal properties, for example, Trice *et al* (1999), Colomban and Gouadec (2005). These properties are very important due to their relationship to microstructure and density, all of which impact on the overall properties of the compounds. Some of the important ones and their implications on applications in devices have been reviewed (Ahmadu *et al*, 2008). They have the lowest tailorable thermal expansion coefficients and exhibit anisotropy in their thermal expansion leading to several theoretical models being formulated to

explain the thermal expansion properties (Hazen *et al*, 1987; Huang *et al*, 1994; Biao *et al*, 1996; Jackson and Porter, 2001; Achary *et al*, 2008) and studies on the coefficients of thermal expansion parameters (Hazen *et al*, 1987; Woodcock *et al*, 1998) have been carried out.

Microcracking is a phenomenon that is observed in these polycrystalline materials when they are heated. Internal forces are set up (that causes cracks in the grains due to the anisotrophy in the expansion of the unit cell dimensions) due to internal stresses among grains, resulting in significant lowering of strength and coefficient of thermal expansion (Biao *et al*, 1996). The microcracks begin when a critical grain size of 2μm is exceeded and this is related to the maximum thermal expansion difference between the lattice parameters (Angadi *et al*, 2002a). In low density ceramics, these microcracks and pores can absorb some expansion thereby causing a reduction in the thermal expansion.

It has been suggested that the anisotropic thermal expansion in NASICON gives rise to poor sinterability of the materials (Tantri *et al*, 2000). This is because the expansion anisotropy in general leads to a contraction of the 'a' axis and an expansion of the 'c', with the R-3c systems, whearas a reversal of this is observed in the R-3 systems (Woodcock *et al*, 1999). Limaye *et al* have synthesized $Ca_{0.25}Sr_{0.25}Zr_2(PO_4)_3$ (CaSrZP) which combines behavior of CaZP with more conventional R-3 behavior of SrZP, to create an essentially zero expansion material (Woodcock *et al*, 1999). The mechanism of thermal contraction within these materials have been under investigation and Alamo has proposed a model based on coupled rotations of the polyhedral networks. The compositions with high degree of thermal anisotropy are the ones prone to microcracking upon cooling at room temperature

(Jackson and Porter, 2001) since the onset of microcracking is related to the sintering temperature and hence grain size. Further, they suggest that the microcracking may be delayed or enhanced by controlling the atmosphere in which the ceramic is heated and cooled, and that thermomechanical properties in general can be improved by compositional and microstructure designs (Biao *et al*, 1996). The use of appropriate atmosphere is therefore important in the characterization and performance of these materials. All the measurements in this work have been carried out in air in order to determine the stability of the compositions. Many other thermal properties have been studied for different microstructures (Ahmadu *et al*, 2008).

Mouahid *et al* (2001) synthesized $Li_{1+x}Ti_{2-x}Al_x(PO_4)_3$ (i.e.Na_{1+x}) by lithium ion exchange reactions and detected lithium content due to an impurity phase Li_3PO_4. Unfortunately, the reactions were incomplete and sodium was found to be present to an appreciable degree in the NASICON samples. They showed that $Li_{1+x}Ti_{2-x}Al_x(PO_4)_3$($x<1.0$) can easily be prepared by direct solid synthesis, though $Li_{1+x}Ti_{2-x}Al_x(PO_4)_3$ ($x>0.5$) could not, hence they used ion exchange in preparing solids with this composition, $Li_{1+x}Ti_{2-x}Al_x(PO_4)_3$ ($0.5<x<0.9$). The thermal studies of the materials did not show any mass losses between room temperature and 1073K. Similarly, DTA did not show any structural change on heating, but melting was observed above 1073K. The lithium orthophosphate, Li_3PO_4 detected provided good connectivity between grains, resulting from small amount of impurity which acted as an intergrain binder. Dongare *et al* (1992) synthesized $NaZr_5(PO_4)_3$, hydrothermally and observed a mass loss of 7.3%, which was associated mainly with the two exotherms in the DTA plot at 593K and 863K, respectively, and which were ascribed to the loss of organic matter used in the synthesis. All organics were removed below 873K and there were no mass losses or heat changes, up to1273K, showing the

thermal stability of the material. Tantri *et al* (2000) studied $Ba_{1.5-x}Sr_xZr_4P_5SiO_{24}$ compounds with x=0.00,0.25,0.50,0.75,1.00,1.25 and 1.50, belonging to the low thermal expansion NZP family, using solid state reaction method. Traces of ZrP_2O_7 were found in all the samples. The SEM micrographs showed an almost uniform grain distribution and the samples were not fully dense, showing a number of pores. The grain sizes ranged from 5 to 35μm. $S_{1.5}Zr_4SiO_{24}$, for example, had a very large grain size which was attributed to the large sintering time and temperature.

Lessing and Gary (2006) synthesized two nanocrsytalline NASICON compositions $NaZr_2S_xP_{3-x}O_{12}$ and $Na_{1+x}Sn_{2-x}In_xP_3O_{12}$. The TGA-DTA were performed on powder samples previously heated in air to 593K. Their TGA-DTA plots showed a significant exotherm occurring at 843K and 803K. The DTA plot showed four different processes happening: two endothermic peaks at 341K and 707K and two exothermic peaks at 490K and 800K. The first peak they attributed to a mass loss of 5.75% , which was due to tightly bound water and volatile organic carbon. The second endothermic peak at 707K, was ascribed to a bond breaking process of tin (Sn), Na and P, that were coordinated with carbon, oxygen and Hydrogen atoms. The first exothermic peak at 408K was broad and has been attributed to the combustion of the precursor carbon. The last exothermic peak at 800K was associated with phase transformation of the precursor compounds to the final NASICON metal oxide.

Brown (2004) showed that low CTE (coefficient of thermal expansion) values confer thermal shock resistance to NZP ceramics. NZP based ceramics and composites exhibit very low thermal conductivities. These combinations of properties makes NZP based ceramics particularly attractive for applications requiring thermal

management, thermal shock resistance, exposure to aggressive gaseous environment and gas clean up.

Lee *et al* (1996), have studied the potential application of $Ca_{0.5}Sr_{0.5}Zr_4P_6O_{24}$ as corrosion–resistant coating, for Si based ceramics, and as a thermal barrier coating material for Ni-based alloys. NZP possess unique properties for consideration as protective coating materials for high temperature structural applications. They have very low thermal conductivity (-1W/mk) for dense slip-cast materials and low coefficients of thermal expansions (CTE) of about 3.61 $x10^{-10}$ to 1.1 $x10^{-8}K^{-1}$. However, some NZP compositions such as $Ba_{1+x}Zr_4P_{6-2x}Si_{2x}O_{24}$ $(0\leq x\leq 1)$, $Ca_{1-x}Sr_xZr_4P_6O_{24}$ and $Ca_{1-x}Zr_4P_6O_{24}$ can be tailored to obtain isotropic thermal expansion characteristics. The melting point of NZP is typically higher than 1073K and therefore their low thermal expansion might render them possible for application as thermal barrier coating materials. The values of thermal expansion coefficients (TEC) determine compatibility with other materials at elevated temperatures and thus are among key properties of a solid electrolyte considered for practical applications. TGA analysis revealed a substantial loss for all hydrated materials on heating up to 373K, accompanied by endothermal DTA effect, attributed to water evaporation. The dehydration of $Na_2CO_3.H_2O$ was expected at 370-420K, whilst the decomposition of Na_2CO_3 took place at considerably higher temperatures (approximately 831K). The study used a family of NZP for developing suitable coating material for C-C composites. The study by Hazen *et al* (1987) determined the high temperature crystal structures of NZP ($Na_{1+x}Zr_2P_{3-x}Si_xO_{12}$) by XRD made on single crystals. The thermal expansion of the NZP for x=0.11, parallel to the hexagonal c-axis was positive ($8.21\ x10^{-8}\ K^{-1}$) between 298K and 973K. The expansion perpendicular to the c-axis was slightly negative ($-1.98\ x10^{-8}K^{-1}$). The authors proposed a model in which the

rotation of the phosphate tetrahedron was coupled to the rotation of the zirconium octahedron. In NZP, replacing the Na with a large cation caused the 'c'-direction of the rhombohedral cell to increase but anomalously the 'a' dimension decreased. Alamo, for example, noticed that the polyhedra were coupled and was able to postulate a model that could account for this anomaly. The stability of this structure for wide range of chemical elements makes this a candidate for universal nuclear waste host material. Heating an alkali NZP ($Na_{1+x}Zr_2P_{3-x}Si_xO_{12}$) caused 'c' dimension to increase and 'a' dimension to decrease. Alkali metals were found in which Li had a positive expansion in both directions while K, Rb and Cs all behaved in a similar fashion to NZP.

Bothe and Brown (2005) prepared low temperature (<1273K) NZP ceramics and got a slurry at 1123K. The CTE values were 9.34 $x10^{-8}K^{-1}$and -2.35 $x10^{-8}K^{-1}$, for the 'c' and 'a' axes respectively. The chemical routes used involved using $ZrO(NO_3)_2.xH_2O$,$NaHCO_3$,$NH_4H_2PO_4$ and $Cu(NO_3)_2.2H_2O$. The DTA showed only one peak at about 523K attributed to exothermic reactions. The temperature range for the heating was room temperature-1273K and total mass loss was around 27.5%, roughly broken into four temperature ranges with thermal stability from 873K. Catti and Stramare (1999) identified two phases of LZP (lithium zirconium phosphate), $LiZr_2(PO_4)_3$, the α and β phase at 423K and 473K, respectively. The α phase with space group R-3c has rhombohedral structure. The other is of a different space group but isotropic with that of β-$Fe_2(SO_4)$. The Li^+ were held firmly to the surrounding oxygen, unlike in the α and α' phases, they had no alternative site to jump in. The structural results therefore fully account for the lower ionic conduction of the beta phase Karian *et al* (2005) studied lithium polymer batteries and used TGA to determine that the nanocomposites were completely dry and moisture free, in

an experiment performed from 573-973K. They attributed weight loss at 373K to the presence of water while the amount of residue that remained at the end of experiment run provided a measure of the inorganic or ash content in the material. The TGA for the nanocomposite electrolyte showed no detectable mass loss that could be associated with the presence of either residual water or organic solvents from the fabrication techniques used. They therefore concluded that the materials were dry and the measured properties were not influenced by such contaminations.

1.3 Background and the Present Work

Sodium zirconium phosphate ($NaZr_2(PO_4)_3$), henceforth called NZP is the parent compound of the family popularly known as NASICON, that is sodium superionic conductor, based on its general formula $Na_{1+x}Zr_2SixP_{3-x}O_{12}$ ($0 \leq x \leq 3$) in which some of the P have been substituted by Si. The x represents the number of moles of the substitution. The general formula shall be referred to as NASICON while the parent compound shall be referred to as NZP, unless otherwise stated. NZP has been widely investigated as a fast ion conductor (Komarneni *et al*, 1986). However, its conductivity is very low for applications and has the problem of stability when operational in cells due to the size of the conducting channels, hence the improvement when Si, for example is partially substituted for Zr, apart from the issue of sinterability (Aono, 1994). Phases with the NZP structure remain the most widely studied of the known low and negative thermal expansion materials. It is also chemically the most versatile (Woodcock *et al*, 1999). The Na is responsible for the ionic conductivity in the compound. A family of compounds of different compositions can be synthesized by substituting the Na, Zr and P with atoms of different sizes and oxidation states. These family of compounds are generally referred to as NASICON,

whether Na or some other atoms are responsible for the ionic conduction or not (Kumar and Yashonath, 2006).

The compounds share the same structural features and different compositions may be synthesized by different methods, such as solid state reaction and sol-gel, principally. Each of these methods results in compounds of different degrees of phase purity, solid solution formation and levels of the optimization of their physical features. In particular, the thermal and electrical properties are sensitive to the synthesis conditions and the processing method used. Therefore different methods of characterization have been applied in order to fully understand the structure and physical properties of the compounds, including X-ray diffraction, for lattice constants and phase determination, chemical analysis, for the determination of composition (using Atomic Absorption Spectroscopy, AAS), Microprobe analysis and Energy Dispersive Spectroscopy (EDX), among others. Also the infrared (IR) spectrum (using Fourier Transform, FT-IR) of the materials have been studied and provides information on the vibrational modes of the various ions and chemical groups present, such as the phosphate group. The most important characterization for energy applications is the electrical characterization, using temperature and frequency dependent conductivity, that is impedance spectroscopy and dc conductivity.

Data is not available for all compositions, particularly for partial substitutions of the Na atoms in the NZP system by Li. $NaZr_2(PO_4)_3$ has been widely studied by many characterization techniques and their electrical properties were found not to be sufficient for applications in electrochemical cells for structural reasons. Hence most studies in the area of energy applications have focused on the full substitution of the Na by Li to give $LiZr_2(PO_4)_3$ and further substitutions of the Zr by Sn, Al, Sc, Ti and P, or by co-doping two atoms at a time in order to enhance the electrical conductivity.

Heterovalent substitution, for example of Zr^{4+} with Sc^{3+} has been shown to be a viable option to obtain compositions with high ionic conductivity (Potapova *et al*, 2008). Other studies have been devoted to conduction due to only one ionic species, that is Li due to its lightweight and high mobility.

In the present work the system $Na_{1-x}Li_xZr_2(PO_4)_3$ (x=0.0,0.25,0.50 and 0.75) was studied in which the Na and Li are simultaneous mobile species and have the same charge. Although the x= 0.00, 1.00 [$(LiZr_2(PO_4)_3$] have been extensively studied and characterized by different methods, data is not available for the other intermediate x values between 0.0 and 1.0. Thus the research provides complementary data on the thermal, structural and electrical properties of this system.

Different compositions of the NASICON and NZP family have been studied by various substitutions of atoms in the structure, depending on the application in view and have provided insight into the nature of research being conducted and the relevant challenges and interpretations that have led to the choice of this system. This is evident from the range of synthesis and characterizations in the following studies.

There has been extensive studies on the $NaZr_2(PO_4)_3$-$LiZr_2(PO_4)_3$ system, but not much data is available on the electrical properties of the $Na_{1-x}Li_xZr_2(PO_4)_3$ system and the effect of two mobile ions (Na, Li) in the NZP system. Such work has only been carried out on glassy superionics and not the NASICON or NZP system, as the coupling of the two ions have been observed to decrease the conductivity to a minimum. Further, most problems associated with solid state synthesis are based on the trade-off of temperature-time relationships: sintering at low temperatures but longer time periods or vice-versa. Here the heat treatments have been optimized through a specified method of processing of the ceramic in order to determine the possibility of formation of a solid solution and single phase NZP in contrast to the

188600

traditional longer time periods at lower temperatures. Though many thermal parameters of the system have also been quantitatively determined, however, the thermal behaviour with respect to mass decomposition, structural and phase transformations have not been fully qualitatively described with increasing lithium substitutions and temperature by DTA/TGA analyses.

This study provided the complimentary data needed. In addition, to systematically study the impedance of these compositions for the first time, the impedance spectra were measured in a broad spectrum of frequency up to the GHz range in contrast to the typical studies carried out on these materials which were limited to the MHz and lower range of frequencies. Further, because the Na was not fully substituted, it would further lead to an understanding of the behaviour of the two mobile ions (Na,Li) with respect to electrical conductivity, on the impedance spectra of the NZP system.

Pet'kov *et al* (2008) in his study provided data on the synthesis, thermal behaviour and thermodynamic properties of NZP phosphates $NaMe_2(PO_4)_3$ and $Na_5Me(PO_4)_3$ (Me=Ti,Zr,Hf) which were synthesized by solid state reaction and sol-gel methods. The thermal behaviour was studied by DTA measurements and heat capacities were measured. The authors used heat treatments of 12h and above and 24h at each of the higher temperatures for sintering. The DTA curves of the compounds $NaMe_2(PO_4)_3$ did not show any thermal effects in the temperature interval 298-1123K, and the lattice constants were found to be in agreement with standard values of the compounds. However, there was no detailed analysis of the trends in the curves.

The grains were found to be homogenous, with crystallite sizes of 1-50μm, leading to the formation of $NaZr_2(PO_4)_3$ and $Na_5Hf(PO_4)_3$, that undergo reversible phase transitions with maximum at temperatures 410 and 520K respectively. However, the lattice parameter change with temperature was not investigated in this case. Pet'kov *et al* (2003b) based on the studies of many phosphate groups provided a guideline for general synthesis of targeted compositions. This information is available for the synthesis and expected properties of some phosphates that were based on the framework ions in the skeleton structure of the NZP system. Using the data on the thermal expansion of NZP materials in the range 293-1273K, together with crystal-chemical data on their structure, a comprehensive guideline to identify the processes underlying the thermal expansion of these materials was predicted. This guideline can lead to the designing of NZP based materials with controlled thermal expansion and near zero anisotropy. Though, such a guideline is not available for all solid solutions, as many compositions have not been studied or synthesized, and data for their thermal properties could not be found.

The enormous substitutions possible in the NZP phase made Komarneni *et al* (1986) to assert that it is one versatile structure capable of immobilizing all the elements in nuclear wastes. Kotelnikov *et al* (2009) and Donald *et al* (1997) have shown that it is indeed possible to use NZP based ceramics for immobilization of radionuclide from radioactive wastes due to their high chemical stability and thus substituted Na by Ca, Sr and K, these seemed to produce good results that enabled an understanding of the behaviour of NZP matrices in the earth's crust. Using the hydrothermal method they studied Sr substitution (Na,Sr), as data is not available for this system, and observed complete ion exchange and solid solution formation. There has also been reports of lithium ion irradiation of NZP to determine

the effect on thermal expansion (Angadi *et al,* 2002b). NZP materials are known to resist radiation damage, form solid solutions with approximately two thirds of all known elements, thus the actinide positions in this structure have been studied by Hawkins *et al* (2000).

Pet 'kov *et al* (2003a) investigated a single host matrix based on NZP designed to immobilize commercial nuclear waste and studied the incorporation of different alkali elements in the NZP host structures. Single phase phosphates corresponding to crystalline solutions with structure similar to NZP were found in the compositions investigated. Using solid state reactions and by heating from 8-20h at different temperatures up to 873K and 10-20h at maximum sintering temperature of 1073-1123K, they obtained well crystallized single phase materials. Powder XRD patterns, with smooth changes in their relative intensities and insignificant changes in the interplanar spacings over the entire composition range, were observed. As part of the series, the authors studied the system $Na_{1-x}Li_xZr_2(PO_4)_3$ (x =0.0,0.3,0.5,0.7 and 1.0), which is similar to the system under investigation , except for some of the compositions, and hence determined the variation of lattice parameters with increasing incorporation of Li in the system. However, they did not study the electrical properties of this composition in terms of impedance spectra and temperature dependent conductivity, though they were able to synthesize their compositions at a comparatively low temperature, this was achieved at a comparatively longer time period. One of the objectives of this study was to use shorter time (8h) without compromising the phase purity, among other parameters. The work is however not concerned with the investigation of radionuclide immobilization properties of the compounds, though the changes of lattice parameters with composition were also investigated and the results of the solid state synthesis

were important. They found, for example, that increasing incorporation of Li in the K system, which has higher radius than Na cation, lead to a systematic decrease in the a parameter and a limited decrease in the c parameter (for x=0.00-0.30), with subsequent increase in the parameter up to the end member $KZr_2(PO_4)_3$.

Similarly, Kazakevicrus *et al* (2004) synthesized and studied the system $Li_{1+x}Zr_{2-2x}Al_xTi_x(PO_4)_3$ (x=0.1-0.3) belonging to the NZP family with heat treatments at various temperatures varying between 8-24h, at the highest temperature, to study Li ion conduction by XRD, chemical analysis and impedance spectroscopy in the frequency range 1.0×10^6 to 1.2×10^9 Hz. The average size of the powder grains were found to be 1μm and the densities of the ceramics were 80-90% of theoretical density of the compounds with small amounts of ZrP_2O_2 detected in the samples as impurities. The substitution of Zr^{4+} by Ti^{4+} and Al^{3+} in the $LiZr_2(PO_4)_3$ was found to decrease the cell parameters a, c and V and a reduction in the density of the compound was observed. These have been attributed to the values of the atomic radii of Zr, Ti and Al atoms which are respectively, 1.6, 1.47 and 1.43Å. There was also an observation that an increase in the Li content in the system lead to an increase in the value of the grain boundary conductivity, σ_{gb} and a decrease of the activation energy, E_a.

The above study is one of the few in the GHz range of frequencies for impedance of NZP, although the composition is different from the one under investigation and the mobile ion is Li. There were also further substitutions in the Zr which were not investigated in the preswent work. The problem of longer time periods for the synthesis, which is a disadvantage, also persists, though the present

work also investigated the activation energy for conduction, together with the conductivity through grains and grain boundaries.

Ignaszak *et al* (2006) studied the effect of humidity on NASICON, $Na_{1+x}Zr_2Si_xP_{3-x}O_{12}$ samples, prepared by co-precipitation and solid state reaction methods, by heating the samples at 24h only at 1423K. The NASICON prepared by solid state reaction crystallized in the monoclinic phase, with mixture of monoclinic ZrO_2 phase and tetragonal $ZrSiO_4$ detected. The samples prepared by solid state method on the other hand, seemed to be more stable under humid conditions and were well densified. Leo et al (2002a) studied lithium conducting glass ceramic with NASICON structure, in which the ion conducting glass and glass ceramics, of composition $Li_{1.4}[Al_{0.4}Ge_{1.6}(PO_4)_3]$, were synthesized by solid state reaction. The samples were based on the original composition $Li_{1+x}[Al_xGe_{2-x}(PO_4)_3]$, for x=0.4. The material was characterized by XRD, SEM and impedance spectroscopy, in the frequency range 10mHz to 100kHz, as a function of temperature. No detectable impurity peaks were observed in the XRD patterns, indicating only NASICON phase formation. The study, similarly, demonstrated the effect of gold and silver electrodes on the impedance spectra and conductivity. Kang and Cho (1999) studied two different formulations of NASICON, by Von Alphen, $Na_{3.2}Zr_{1.3}Si_{2.2}P_{0.8}O_{10.5}$ and the Hong, $Na_3Zr_2Si_2PO_{12}$. The dependence of phase formation, sintering behaviour and electrical characteristics of NASICON, on the sintering temperature, time and cooling process was investigated. Such a study has not been carried out on the current system $Na_{1-x}Li_xZr_2(PO_4)_3$, and therefore the effect of shorter heat treatment times and higher sintering temperatures on the phase formation and microstructure have been investigated.

Lithium-conducting solid electrolytes have been found to be the most important in rechargeable battery applications, due to the special physical properties of lithium, such as its small size and low density, which gives it increased electrical conductivity on partial as well as full substitutions in the NZP system, hence the study of lithium substitutions. Other compositions have been obtained by replacing the Zr with Ge, Sc, In and Ti with the result that several orders of magnitude increment in conductivity at room temperature was obtained, amongst other substitutions for P. The substitution of Na has been found to be necessary since it is not a good ionic conductor for structural reasons (Wang and Zhou, 1998). NZP has been found to be thermally stable to 1773K (Brown, 2005), and NASICON, depending on its composition, has melting point higher than 2073K (Lee *et al*, 1996). Many studies carried out on the NZP materials reflects the current application challenges and indeed potential applications of the compositions, such as in corrosion–resistant coating material for silicon–based ceramics and thermal barrier coatings (Lee *et al*, 1996). Similarly, in the development of Carbon-Carbon (C-C) composites due to the matching of their thermal expansion properties (Agrawal *et al*, 1996) and as a nuclear waste immobilization host material (Hazen *et al*, 1987; Nakayama and Itoh, 2003; Volkov *et al*, 2003). Recently, new materials of the NZP family have been developed and structurally characterized that showed high ionic conductivity and optical property, an uncharacteristic property of these compounds. They include $Na_3Al_2(PO_4)_3$ with bulk conductivity of 5.10^{-2} S/cm at 873K (Brunet *et al*, 2003), $Rb_3Yb_2(PO_4)_3$ a cubic system (Carvajal *et al*, 2005) and $Pb_{0.5}Ti_2(PO_4)_3$, a hexagonal system of the R-3c space group (Bouari and Jazouli, 2004). Similarly, new NASICON-related Potassium Iron (III) Pyrophosphate has been synthesized and characterized (Gopalakrishna *et al*, 2005), with potential for many applications. A

typical member of such novel materials is rhombohedral $Li_3Fe_2(PO_4)_3$ (Andersson *et al*, 2000) and $Li_{2.5}V_2(PO_4)_3$ (Yin *et al*, 2004) which are potential electrode insertion materials in lithium polymer batteries, based on their good ionic conductivity and low cost.

There are many problems faced in the synthesis and characterization of NZP materials, both on the scientific fronts and for technological applications. Some of these include:

1 Optimizing the synthesis conditions to produce pure phase, homogenous, dense materials without ZrO_2 second phase and uniform distribution of grain sizes in the solid state reaction (Ahmadu *et al*, 2009).

2 Determination of the crystal structures of the relevant compositions, including lattice parameters, crystallite size and density in order to ascertain their structure–property relationships.

3 Evolution of methods to prepare NZP at low temperatures or shorter time periods without compromising microstructure and other physical properties.

4 Formulation of appropriate compositions of NASICON to enhance thermal properties suitable for low, near zero and negative thermal expansion and an understanding of the physics and chemistry of the thermal expansion anisotropy

5 Determining the thermal stability of various compositions through quantitative and qualitative analysis such as specific heat, heat of fusion and phase transitions observed in the materials.

6 In the medical field NZP are being explored for their low thermal expansion properties for the production of prosthesis coupled with their bonding

characteristics to tissues (Calcium-Titanium-Phosphate (CTP), $CaTi4(PO4)_6$ (Heinmann, 2002; Ribeiro, 2005).

7 Understanding the scientific basis and theoretical framework of the mechanism of electrical conductivity in these materials, given their different structures and microstructures and modeling of the conductivity through the grain boundary and bulk microstructure in polycrystalline materials.

8 Reducing the temperature of superionic conductivity towards ambient conditions from the current high temperature or enhancing the electrical conductivity of these materials by the formulation of various compositions or changes in microstructure and studying the subsequent structure-property relationships (Park *et al*, 2005).

9 Synthesizing, optimizing and processing of the NZP to produce microporpous microstructure suitable for use as thermal barrier coatings and heat filter.

10 Synthesizing the appropriate compositions of the NZP with relevant properties suitable for immobilization of radionuclide and reprocessing from nuclear wastes.

11 Using compositions of NZP materials that are cheap, environmentally friendly and abundant by reinforcements using various fibres for improved mechanical, optical, among other properties.

The objectives of the work were to:

1. Study the composition $Na_{1-x}Li_xZr_2(PO_4)_3$, (x = 0.00, 0.25,0.50 and 0.75), which has not been investigated nor fully characterized, in terms of specified characterization techniques, and obtain relevant data for the system.
2. Synthesize the system using solid state reaction by optimizing the processing conditions at lower heat treatment time (8h) and maximum sintering temperature of 1523K.
3. Determine and qualitatively describe the thermal stability of the system in terms of mass decay with increasing temperature, melting and structural transformations of the system through thermal characterization techniques DTA/TGA.
4. Determine the phases present, crystal structure, lattice parameters, crystallite size and microstructure of the system.
5. Determine quantitatively, and qualitatively describe the electrical properties, such as the dc conductivity (fitting to the Arrhenius equation) and impedance spectroscopy of the system using relevant theoretical framework such as Bricklayer Model (BLM), Jonscher's power law and the mechanism of electrical conduction as it affects the microstructure of the system.
6. Determine the suitability of the application of the system as electrolyte and related applications, based on the data acquired.

The search for new materials for emerging technological applications and as solution to existing problems faced in industry and for academic pursuit, has meant that the choice to study NZP was timely and tenable based on the following:

1 NZP ($NaZr_2(PO_4)_3$ has very unique structure and properties that have not been found in any known substance yet. Its three dimensional structure has structural holes that absorbs the effect of thermal expansion with tailorable near zero or negative thermal expansion coefficients that makes it suitable for many applications and research.

2 The interstitial sites in the framework which are interconnected and allow small ions like Na, Li to move freely, thereby providing electrical conduction in three dimensions under an applied electrical field at appropriate temperatures, make it suitable for applications as electrolytes in rechargeable battery applications.

3 Most of the superionic materials used for electrical conduction are one and two-dimensional in conductivity but NASICON is three dimensional and therefore makes it attractive for research.

4 The Na, Zr and P can be substituted by up to 40 atoms of different radii and oxidation states ranging from 1^+ to 5^+ without changing the basic crystal system but giving the compound different physical and chemical characteristics suitable for diverse applications, thus making it one of the most important and interesting materials to study. One can therefore substitute any atom (s) in the system, except oxygen, and determine their properties in other to find their appropriate applications.

5 In energy applications there are many existing challenges in the area of portable rechargeable batteries that are Li ion based (Manthiram, 2009), and grid level high power energy sources. This includes the search for Solid Oxide Fuel Cells

(SOFCs) for next generation cars, expected to mitigate the current energy crises and diversify our dependence on fossil fuel. What with the mobile phone industry that uses Li ion batteries, the need to carry out research in this area becomes imperative. Thus fostering the development of renewable energy sources by discovering new materials with enhanced properties. NASICON is a potential candidate in this development.

6 Similarly, electrochemical sensors based on Solid State gas sensors (Vera and Aragon, 2005) (based on NASICON) are also being developed. NASICON based gas sensors are promising for operation at low temperatures, compared to LISICON based ones (Jasinski *et al*, 2006). Solid State-based gas sensors are used for environmental detection of pollutant gases, such as CO_2 (Lee *et al*, 2004b; Akbar *et al*, 2006; Xu *et al*, 2006) and SO_2. NASICON-based ones are most sensitive and are portable. Because they are currently operated at high temperatures, the focus of research has been to reduce the temperature of operation and improve the electrical conductivity, since NASICON is thermally stable, including to the chemicals used as electrodes.

7 $LiFePO_4$, $Li_3V_2(PO_4)_3$, among others, are being considered as electrode material, another family of NASICON. The smallness of the Li ion and its lightweight offers greater conductivity comparable to Na-beta alumina, one of the best ionic conductors and therefore makes it favourable and important for research. Moreover, the need for increased charge capacity and to withstand charge–recharge cycles by electrochemical rechargeable cells are equally important and imperative.

8 Their extremely low thermal expansion and indeed tailorable expansion makes them very attractive for design of ceramic based block engines of cars, exhaust pipes and in use as optical components in space vehicles.

9 Their thermal properties are potentially useful in the design of micro porous NASICON materials to act as thermal barrier coatings and heat filters.

10 It has been demonstrated that the NZP family offers the best host materials to act as immobilization for many radionuclide wastes and also makes it easier for reprocessing.

11 Similarly, many chemical effluents that pollute the environment have been found to be easily absorbed by NZP based materials. Recent report has demonstrated that it can potentially be used in waste water treatment too (Wilmarth *et al*, 2007).

12 In medical applications, NZP materials are increasingly being considered as potential candidates in the manufacture of prosthesis for limbs due to the near zero tailorable thermal expansion and good mechanical properties in bonding to tissues, as has been demonstrated recently in some preliminary studies.

13 NZP materials are also applied in insulators due to their high resistance to thermal shock and the high degree of predictable dimensional stability when subjected to thermal active environments.

14 Some of the successful applications of NZP include, optical benches, semiconductor wafer fixtures, furnace support structures, fixtures for high-tolerance brazing, furnace baffles, and thermal insulation for diesel engine exhaust ports. Consequently the need for further work in the area.

15 In addition to these applications, a number of new development programs are currently active at the company SMAHT in the US in this direction, where NZP

ceramics are being developed for environmental and thermal barrier coatings under industry and government funded programs.

16 Reinforced-NZP ceramics which have potential for application in rocket engines and missile systems are also currently being developed. Figure 1.1 shows some of the products from NZP based compounds. All of the above reasons and others too numerous to mention, makes the case for studying this material expedient.



Figure 1.1:Processed NZP components (SMAHT Ceramics, 2004)

The work is limited to the synthesis of NZP compositions by the method of solid state reaction, phase identification, analysis of the microstructure of the compositions, including crystallite size, density and lattice parameter calculations of the structure. Similarly, electrical characterization, using the Arrhenius conductivity and impedance spectroscopy were undertaken. The use of equivalent circuit modeling for determination and analysis of the impedance spectra, in conjunction with the Brick Layer Model (BLM) for conductivity interpretation have been implemented. The calculation of relaxation frequencies for grain and grain boundaries have been undertaken together with their activation energies. The analysis also included the fitting of the observed conductivity spectra to appropriate theoretical models. Thermal analysis was limited to investigations of the thermal stability of the calcined compositions and phase transformations or changes. Specific heat capacities, heat of fusion, thermal expansion coefficients, etc. are out of the scope of the investigations. Lattice parameters' refinement, such as Rietveld refinement techniques for XRD are out of the scope of the work too. Similarly, the fitting of the dc component of ac conductivity and relaxation frequencies to the Arrhenius type equation were not undertaken.

1.4 Thesis Outline

The thesis is organized into five chapters. Chapter one is an introduction of fundamental concepts in ionic conductors. The basic definitions of the concept of superionic conductors, as it affects these materials have been presented. The classes, mechanisms of conduction, potential applications and defect characteristics have been discussed in relation to their conductivity. The chapter reviewed some studies that have been carried out on these materials, such as on impedance spectroscopy, structural characterization, synthesis and thermal analysiss. These discussions have been largely restricted to NZP and NASICON materials, being the materials of focus in the study. Also there is an intensive analyses of the peculiar structural properties of NZP and NASICON that have implications for their electrical conduction properties and substitutionability. The background that formed the imperative to carry out this study has also been provided on the selected system, $Na_{1-x}Li_xZr_2(PO_4)_3$, from which the scientific and technological problems requiring investigation, the objectives of the work and justification for the study have been enumerated. The chapter concluded by specifying the scope and limitations of the work.

Chapter two is a survey of the general theoretical framework upon which the study, particularly, the characterizations were based. Thus it reviewed the various theoretical models that have been applied in the study of superionic materials in general, with specific reference though, to NZP and NASICON. There is also a discussion of the theory of the solid state synthesis, X-ray powder diffraction measurements and the analysis of the results, together with a discussion of scanning electron microscopy technique for microstructure determination. The chapter concluded with discussions on dc conductivity

(Arrhenius type) and impedance spectroscopy analysis, theory, experiment, and models. These were carried out within the context of two mobile ions Na and Li, and investigated at high frequency in the GHz range. The analyses were largely within the context of relaxation frequency of the bulk and grain boundary as related to the use of the Brick Layer Model.

Chapter three is a discussion of the chemicals, materials and facilities used in the preparation and characterization of the samples, such as SEM, DTA/TGA, XRD and impedance spectroscopy. Their limitations and sensitivity have also been pointed out.

Chapter four is the presentation of the results from the work and their analyses. Hence these were carried out, for all the characterizations, within the context of the relevant theoretical framework in the field, models and literature surveyed.

Chapter five is a summary of the highpoints in the synthesis and characterization of the investigated materials. The fundamental findings from the research have been highlighted and their implications *vis-a-vis* the problems highlighted in their investigations and the set objectives. The chapter also presented some suggestions for improvement of the data obtained for future work. Finally, there is a recommendation for improving generally the research in material characterizations and for harnessing the results obtained from this work, due to its significance for national development, industry and academia.

CHAPTER TWO

THEORETICAL CONSIDERATIONS

2.1 Theoretical Models of Ionic Conductivity

There are several theoeretical propositions that have been put forward to study and explain the superionic phenomena.We shall review some fundamental ones including modelling and simulations techniques. Sunandana and Kumar (2004) have carried out an indepth review of various classes of superionic conductors, their properties and the theoretical models particularly, the AgX (X= Cl,Br,I) family. Most of the models have demonstrated a good correlation with experimental data, though in certain superionics such as glasses, non Arrhenius behaviour (AB) in their dc conductivities have been observed and appropriate theoretical models have been proposed that explained most of these observations (Maas *et al*, 1996). Kumar and Yashonath (2006) undertook a similar survey of these materials according to their classes, conduction mechanisms and characterization techniques. The authors emphasized the increasing power and use of simulation (Battacharya *et al*, 1998; Calleja and Dove, 2004) techniques such as Monte Carlo (MC), Molecular Dynamics (MD), among others, for studying the properties of NASICON and related ionic materials. Indeed there has been report of the simulation of the melting and crystallization process itself using MD simulation (Kerrache *et al*, 2008), amongst studies of many other phenomena. They also provided a significant review of the applications of these techniques in the determination of the electrical conductivity and phase transition temperatures of $LiZr_2(PO_4)_3$, among others. Very good results were obtained and compared to the experimental values. Such a simulation study carried out on CaF_2 showed a good

correlation (Allan *et al*, 2000) with the experimentally determined values. Similarly, one of the most widely studied ionic materials is zirconia, stabilized in its high temperature cubic form. Molecular dynamics simulation and static dynamics have been applied to study the grain boundary conductivity, producing a very good result which correlates with experimental values (Fisher and Matsubara, 1998) .

Various simulation techniques have also been discussed in detail by Yip (2005) and the mode of implimentation and conditions of use explained, together with their applications in highly disordered systems such as CaF_2, AgI, CeO_2, ZrO_2. These have provided very valuable data on the phase transition temperatures and conductivity. Some sudies have applied even quantum mechanical density functional theory (DFT) (Mao *et al*, 2002; Yip, 2005; Kumar and Yashonath, 2006; Holmstrom *et al*, 2010) have been applied in some cases in the molecular dynamics simulations of these materials and similar ones. Shimojo (2006) studied atomic dynamics in superionic conductors by *ab initio* Molecular Dynamics (MD) technique on CuI, Ag_2Se and successfully reproduced the ionic behaviour. Using MD simulation technique, he was able to reproduce the temperature dependence of the diffusion coefficient of the mobile ions, in good agreement with experimental data.

The determination of phase transition temperatures in superionic conductors is important as it is associated with large increase in conductivity and changes in specific heat, among other parameters that are affected. Many physical properties of materials change with structural transformations, however in superionic conductors a high conductivity is associated with this state and the increase in conductivity is abrupt and first order. However, not all NASICON members show structural transformations during the phenomenal increase in conductivity. For example, NZP

($NaZr_2(PO_4)_3$ is not associated with structural phase transformations at the high conducting state or specific heat changes. Studies have revealed that such a transition could be detected accurately using photo acoustic technique (Zurawaski, 2006). This has been applied successfully to many superionic materials of the AgX family and agreed well with literature data on superionic transition temperatures.

Research in superionic materials have also focused on how to increase the room temperature conductivity values to a value such as 10^{-1} to 10^{-3}S/cm (Kawamura *et al*, 2007) or 10^{-2} to 10 ohm-cm^{-1} (Ramasesha, 1999), the range that will make them suitable for applications in devices such as lithium ion batteries. However the reverse questions are also being asked, such as the factors that limit conductivity in these materials? In their work, Maliki *et al* (2006) have suggested that the non Arrhenius Behaviour (AB) observed, for example in glassy ionic conductors, which limits their conductivity, could be improved by annealing and densification of the electrolytes, as it reduces the saturation which may be responsible for the loss of Arrhenius behaviour.

Singh and Bhoga (1998) studied the ionic conductivity of $(1-x)Li_2SO_4:(x)Me_2SO_4$ (where Me=Na, K, Rb, and Ag; x= 0.025 to 0.09) and systematically investigated it by complex impedance spectroscopy. The partial replacement of Li^+ with Me^+ of bigger ionic size increases the conductivity due to lattice loosening. The maximum conductivity enhancement is achieved by Ag^+ substitution. A simple model based on change in entropy and Coulomb interaction is applied to understand the increase in conductivity. Their earlier investigations reveal that in addition to valence, the ionic size and electronic structure of doped cations do play an important role in ion transport through the solid. The mismatch in the ionic radii of host and guest cations alters inter-ionic distance, and so influences Coulomb

interactions and internal energy associated with lattice vibration. The former modifies the activation barrier height for ion migration, simultaneously, the latter governs the defect concentration. Similarly, Song *et al* (2008), and Tschope (2003) in their study of $BaCe_{0.8}Y_{0.2}O_{2.9-\delta}$ and Cerium oxide respectively, used the space charge potential model, to show that in ionic compounds, the composition at the surface or interface may differ from that in the bulk, resulting in a difference in electric potential between the grain boundary and the bulk. Due to the presence of excess ions at the grain boundary under equilibrium, a space charge potential is developed to compensate for these excess charges.

It is generally accepted that both structural and conduction energetic features are involved in the mechanism of superionic conduction. Therefore studies have highlighted the role played by carrier concentration, mobility, and temperature or the dynamics and composition of these complex materials to understand their surprisingly high values of ionic conductivity (Maliki *et al*, 2006).

Using a chemical bond approach, Aniya (2006) enumerated three conditions for a material to exhibit the superionic character: 1) it must have an open structure within which the mobile ion should have low coordination number; 2) the superionic conducting material must show a structural phase transition at relatively low pressures and 3) for a material composed of atoms A and B, a parameter defined as $Z^* = (Z_A \frac{Z_B}{\varepsilon_o})^{1/2}$ exhibit a small value, where Z_A, Z_B are the valances and ε_o is the static dielectric constant. These criteria have been fulfilled by many superionic materials from experimental data. There are otehr conditions spelt out, such as the fact that the empty and occupied sites should have similar energies, with a low activation energy for jumping between neighbouring sites; the requirement that the structure

should have a framework, preferably 3D, with open channels through which ions could migrate and that the anion framework should be highly polarisable (Slater, 2007), among others.

In order to improve the performances of devices based on ions, it is necessary to understand the ionic transport mechanisms, not only in simple one dimensional systems such as liquids and crystals, but in glasses, polymers, polycrystalline and three dimensional systems. One theory that has the potential for application to 3-dimensional systems is the concept of 'coupling and decoupling' by A. Angel (Kawamura *et al*, 2007) and is a guideline for searching for high ionic conductivity in complex materials. According to this concept the mobile ion should be decoupled from the surrounding other ions and molecules by optimizing the chemical bond strength and coordination number. There are exceptions though to this. A good example is found in the so-called 'mixed ion effect', where ionic conductivity shows drastic decrease when two mobile ions are mixed or present in the same substance , e.g, Na and Li in B_2O_3 glasses. The mobile ion is found to be decoupled from the surrounding counter anions to allow the ion to move fast. However, the observed conductivity shows very low values, almost insulating in some compositions. This anomalous behaviour of conductivity is believed to be related to a 'percolation transition', which is a special feature of the complex materials, not observed in simple liquids or single crystals of homogenous structure. Perhaps, it can be applied to NASICON. Further, no attempts have been made by researchers to explain fully the conductivity model in NASICON.

Aniya (1996a) has similarly, applied the Real Space Pseudo Potential method to study Cu and Ag Halides with the Zinc–Blende structure, using the Bond Model from the electronic theory of superionic conductors, and provided further insight into the concept of a ''mobile ion in a cage formed by the immobile ion''.

In a comparative study, Aniya (1992a) used the Pseudo Potential method to study AgI, a well known superionic conductor and GaAs, a well known semiconductor. The result showed that the bonding in AgI is mainly determined by the Iodine and suggests that the local electronic excitations from the bonding to the antibonding orbitals can trigger the migration of the mobile ion species and thus initiate the superionic transport. Recent interest in the electron substructure to explain the behaviour of superionic materials made Aniya (1992b, 1996b) to suggest that the change of bonding which occurs locally and fluctuates in time plays an important role in the understanding of the phenomenon of superionic conduction. This is because the fluctuation of the bond creates field of forces which move the ions and which in turn trigger new bond fluctuations. This model has been used successfully in the interpretation of many experimental observations. There are other studies such as the screening concept and strain (Grey-Weal, 2007) in ionic conductors that are relevant for the understanding of the defect and thermal properties of these compounds due to the relationship to conductivity, amongst many other studies. A discussion of the various models and their consequent theoretical implications show that many factors affect ion motion: concentration of charge carriers (defects or mobile ions), the distance between available positions, temperature, the correlation between charge carriers, the change of the thermodynamic potential of the motion of ions, and the change of thermodynamic potential of origin of defects (Vitioo, 1999).

488600

2.2 Methods of Synthesis and Thermal Analysis

NASICON can be synthesized by conventional ceramic methods including solid state reaction method (or powder mixing), solution–gel or hydrothermal methods. Ion exchanges are also employed. The sol-gel method is found to be better in most cases because the mixing of the components is achieved at a molecular level. The sol-gel has been most successful technique to get very fine powders, low sintering temperature and Na and P losses are minimized or completely avoided (Fuentes *et al,* 1999). Other advantages of sol-gel processing, include the ability to achieve oxygen and ionic stoichiometry during the formation reaction, to synthesize complex compositions, single phase materials, to form higher purity products through the use of high purity reagents, and to provide coatings over complex geometries including the insides of tubes (Nguyen, 1998). However, these advantages are to be put in balance with the raw materials' high cost, the long processing time involved, the non-uniformity of the films, and the formation of cracks upon drying.

The principle of sol-gel technique consists of converting the sol which is a suspension of colloidal or polymeric particles in a solvent, into a semisolid phase known as gel.The hydrothermal method, on the other hand, provides a low temperature route for synthesis of ultra fine powders of $NaZr_2(PO_4)_3$ (Kumar and Yashonath, 2006). In this work the method chosen for the synthesis is the solid state reaction and this is described briefly below. Recently however, a more powerful method has been applied using microwave heating. The products from this method exhibited high phase purity, good crystallinity, minimal loss of volatile constituents and has been used to prepare NZP compositions (Naik *et al*, 2004; Agrawal *et al,* 2006; Naik *et al*, 2010).

2.2.1 Solid State Synthesis

In the study of NASICON materials, it is important to synthesize the materials to be investigated due to the required changes in the atomic composition of the target materials. However, out of the many methods of synthesizing materials, Physicists prefer the solid state reaction method as it requires simply heating the dry powders in a systematic manner until they fuse and form the required compound, which are then checked by XRD,SEM and elemental analysis methods to ascertain whether the materials have been formed with the correct stoichiometry. Such work has been carried out by other Physicists (Nga and Son, 2004; Salkus *et al*, 2006a; Salkus *et al*, 2006b). Most inorganic solids are prepared by the reaction of a solid with another solid, a liquid (melt) or a gas usually at high temperatures. Many ''solid /solid' reactions, are actually 'solid'/liquid' reaction, because at high temperatures some of the solid can melt to form a liquid phase. It is therefore difficult to determine the physical phases involved in a given reaction.

In synthesizing multicomponent solid materials the oldest and most common method is the direct reaction of solid components at high temperatures which is called the 'ceramic method' or 'solid state reaction'. Because solids do not react with each other at room temperatures high temperatures are required to reach the suitable reaction rates. Under high reaction temperatures (between 873K and 1773K) of traditional solid state synthesis most of the inorganic phases are stable. High temperatures are used so that if there is a difference between the structure of the starting materials and the products all bonds in the starting materials must be broken and atoms must migrate before new bonds could form. This diffusion makes the reactions impossibly slow unless very high temperatures are used. As a rule of thumb,

two-thirds of the melting temperature of one component is enough to activate diffusion sufficiently and to enable solid state reaction (Ozmen, 2006).

Most compounds made at high temperatures are thermodynamically stable. However, the synthesis of new materials becomes very difficult at high temperatures due to other phases, intermediate or perhaps unreacted components that might be present. However, with the proper conditions, thermodynamically stable compounds may be prepared. The reaction between two solids may not occur even if thermodynamic conditions favour the formation of product. The rate of reaction between solids is affected by area of contact between the reacting solids (and hence their surface areas), the rate of nucleation of the product phase and the rate of diffusion of ions through the product phase. Therefore when applying the solid state reaction method the first step is to fine grain the starting compounds in order to maximize surface areas and hence reaction rates. This is done by processing the powder in pellets in order to provide intimate contact between grains which are the single crystals in a polycrystalline aggregate. Carbonates and others that decompose at high temperatures are often employed in traditional solid state reactions. The heating program depends very much on the form and reactivity of the reactants. For solid state reactions generally the choice of suitable container is very important which is chemically inert to the reactants at high temperatures. For synthesis of metal oxides generally, platinum, silica and stabilized zirconia or alumina are used. If one of the components is volatile or sensitive to the atmosphere, the reaction is carried out in sealed evacuated capsules.

The advantages of solid state reaction are availability of precursors (starting materials) and low cost for powder production on the industrial scale. The

disadvantages of the solid state reaction method are undesirable phases may be formed, the homogenous distribution of dopants is sometimes difficult to achieve and there are limited opportunities for *in situ* monitoring of the progress of the reaction, instead physical measurements such as XRD are periodically carried out. This difficulty results in mixtures of reactants and products frequently obtained. The separation of the desired product from these mixtures is generally difficult, if not impossible (Ozmen, 2006). Moreover, in many compounds, the reaction temperatures cannot be raised as high as necessary for reasonable reaction rates because one or more component of the reacting mixture may volatilize. In order to overcome some of these problems particularly to reduce the reaction times and to increase diffusion rates, it is necessary to optimize the critical parameters such as decreasing particle sizes and increasing surface area by grinding, performing the solid state reactions in molten fluxes or high temperature solvents. In this work, the reaction time is decreased by thorough grinding and remixing of the mixtures to decrease the particle size and hence surface area of contact. Also different materials have been tested to obtain alternate materials that will be suitable for the reaction since Platinum crucibles could not be obtained. In addition, the highest sintering temperature was fixed at 1523K to minimize the effect of P and Na volatilization at higher temperatures.

One of the thermal treatments necessary to bring about the formation of ceramics is sintering. This is a method of making materials from powder by heating the material below its melting point until its particles adhere to one another. It is traditionally used for ceramic objects, and is part of the firing process used in the manufacture of pottery and other ceramic objects. Some ceramic raw materials have a lower affinity and a lower plasticity index than clay, requiring organic additives in the stages before sintering. All the characteristic temperatures associated with phase

transformation, glass transitions and melting points occurring during a sinterization cycle of a particular ceramics formation can be easily obtained by observing expansion temperature curves during optical dilatometer analysis.

Sinterization is associated with remarkable shrinkage of the material due to the fact that glass phases flow when their transitions temperatures are reached and start consolidating the powdery structure and considerably reducing the porosity of the material. There are two types of sintering: with pressure known as hot-press sintering and without pressure .The sintering type used here is the latter, without pressure.

Calcination, also referred to as calcining, is also a thermal treatment applied to ores and other solid materials in order to bring about thermal decomposition, phase transition or removal of a volatile fraction. The process normally takes place below the melting point of the product materials. It is carried out in furnaces (Klins) of various designs. We have used a homemade gas furnace for this work and this was part of the synthesis process of the samples. Examples of calcination include the decomposition of hydrated minerals, decomposition of carbonate materials and volatilization of organic compounds. In calcination substances are subjected to the action of heat but without fusion for the purpose of causing some change in its physical or chemical constitution. The objectives usually include to: 1) drive off water present as absorbed moisture, water of crystallization and 2) drive off carbon dioxide, sulphur dioxide or other volatile constituents and to oxidize a part or whole of a substance (Wikipaedia, 2009).

2.2.2 Thermal Analyses Techniques

Thermal analysis measures physical or chemical changes in a material as a function of temperature. Two common complimentary techniques in this category are differential scanning calorimetry (DSC) and thermogravimetric analysis (TGA). These methods are typically used to determine the material properties of organic polymers as the sample is heated or cooled in a controlled manner or held isothermally for a specified time.

Differential thermal analysis (DTA) is a method similar to DSC, but performed at higher temperatures for metals, minerals, ceramics, and glasses. DSC measures heat flow to or from a sample as a function of temperature and time. A small portion of a sample is placed in an aluminium pan and heated and/or cooled in a controlled manner. A reference material, usually an empty aluminium pan, simultaneously undergoes the same programmed time/temperature routine also. Calorimetric measurements are made during the heating/cooling cycle.

There are two principal methods that are used for the calorimetric measurements. Differences in temperature between the sample and reference material can be measured as the same amount of heat energy (Joules) is added to both. Or, differences in the amount of heat energy added to both are measured as the temperature for both the sample and reference are kept constant. In both cases, the heat flow and temperature of the sample are monitored in comparison to the reference material. The analysis is usually performed in an inert gas atmosphere, such as nitrogen for example. The amount of energy absorbed (endotherm) or evolved (exotherm) as the sample undergoes physical or chemical changes (e.g. melting and crystallization) is measured in (calories or mW) as a function of the

temperature change. If the thermal event studied, such as smelting requires heat input to the sample (endothermic change) then a negative peak, endoderm appears in the DTA (Kutucktu, 2005). Any material reactions involving changes in heat capacity (e.g. glass transition) are also detected.

The thermal cycle for DSC typically can range from less than 223K to 573K or greater. The principles for differential thermal analysis (DTA) are similar to DSC, but the temperature range for DTA can reach temperatures greater than 1873K. DTA analysis is used for determining the temperatures for melting and solid state phase transformations in metals, minerals, and ceramics. In the DTA the heat flow to the sample and reference remain the same. When the sample and reference are heated identically, phase changes and other thermal processes cause a difference in temperature between the sample and reference. The DTA technique has been used in this work and the analysis is up to temperature of 1273K.

Thermogravimetric (TGA) analysis continuously measures the mass of a sample as a function of temperature and time. The sample is placed in a small pan connected to a microbalance and heated in a controlled manner and/or held isothermally for a specified time. The atmosphere around the sample may consist of an inert gas, such as nitrogen, or a reactive gas, such as air or oxygen. The heating program may start in an inert atmosphere and then be switched to air at a certain point to complete the analysis. Mass changes observed at specific temperatures correlate to volatilization of sample components, decomposition, oxidation/reduction reactions, or other reactions or changes. Fourier transform infrared spectroscopy (FT-IR) or mass spectroscopy (MS) may be used in conjunction with TGA to analyze and identify the evolved gases from constituents volatilized from the sample at specific temperatures.

As the TGA instrument measures the temperature and weight of the sample, thermally activated events are recorded. These events are expressed as weight change for a given time or temperature. They may also be expressed as a rate of mass loss too. The onset temperature for the mass loss is also recorded. These data correlate to and give information about such properties as: thermal stability, moisture or solvent content, additive or filler content, oxidation or decomposition temperatures and rate. Thermal events such as melting, according to Materials Evaluation and Engineering (MEE, 2006), glass transition temperatures and other changes are not detected because there is no change in sample mass associated with these events. Identification of the constituents driven off as evolved gases may be obtained when the TGA is used in conjunction with FT-IR or mass spectroscopy. Measurements of temperature changes are accompanied by measurements of the weight changes in the sample. If there is evaporation from the sample, it appears as mass decrease; if there is oxidation, it appears as mass increase in the TGA (Kutucktu, 2005). The experiment is performed in air and depending on the stability of the sample; it may be stable to oxidation so that weight increase may not be observed. The sample should have the same heat capacity over the entire temperature range of the TGA. Analysis in TGA measurements relies on a high degree of precision in three measurements: mass, temperature and temperature change. As many mass loss curves look similar, the mass loss curve may require transformation before results may be interpreted. A derivative mass loss curve may be used, for example to tell the point at which mass loss is most apparent.

TGA can be used to determine the degradation temperatures, absorbed moisture content of materials, the level of inorganic and organic components in materials. The TGA analyzer usually consists of a high precision balance with a pan

loaded with the sample. The sample is placed in a small electrically heated oven with a thermocouple to accurately measure the temperature. The atmosphere may be purged with an inert gas to prevent oxidation or other undesired reactions. A computer is used to control the experiment. Analysis is carried out by raising the temperature gradually and plotting mass versus temperature automatically. However, we have used mass as against mass for the analysis.

2.3 Structure and Physical Properties of NZP

The structure of NZP is such that the Na^+ are located in the interstitial sites in the framework and ionic conduction takes place when Na^+ ions move from one site to another through bottlenecks formed by oxygen ions (Dong–mei *et al*, 2007) with a strong covalent bond. The total electrical conductivity strongly depends on the density and nature of the grain boundaries. NASICON compounds exhibit a few crystalline forms depending on temperature and composition. The structural formula of NASICON can be written as $[M'_1][M''_3][A_2^{VI}][B_3^{IV}]O_{12}$, where M'_1,M''_3 are interstitial sites occupied partially or fully by Na or other substituting ions. A and B lattice sites are primarily occupied by Zr and P or by possible substituting ions. The crystallographic structure of the parent composition $NaZr_2(PO_4)_3$ was first determined by Hangman and Kriekgaad (Breval *et al*, 1995) in 1968. NASICONs are indeed solid solutions derived from $NaZr_2(PO_4)_3$, by partial replacement of P by Si, with Na excess to balance the negatively charged framework (Mouahid *et al*, 2001).

The network structure of NASICON can be modified by using double phosphates and silicates to give the general formula $Na_{1+x}Zr_2P_{3-x}Si_xO_{12}$ ($0 \leq x \leq 3$). In the skeleton of the complex anion $(Zr_2P_{3-x}Si_xO_{12})^{(1+x)-}$, each ZrO_6 octahedron shares its six corners with tetrahedra of PO_4 or SiO_4, and each tetrahedron shares its four corners with the octahedron. Thus each O^{2-} bonds strongly to a tetrahedral and an octahedral cation. The compound has two symmetries, in the range $1.8 \leq x \leq 2.2$, the material is monoclinic *C*2/c (figure 2.2(b)); the rest of x yields rhombohedral unit cells of the *R3-c* space group at room temperature, figure 2.2(d) . The x=2 has the highest conductivity. At higher temperatures (≈200°C), the NASICON takes the rhombohedral symmetry in the entire x-range and a phase transition involving rearrangement of Na^+ ion sublattice occurs. The geometrical features of the skeleton

and its interstitial space therefore satisfy the criteria for fast Na^+ ion transport. Figure 2.1 shows the structure of NASICON with the Na^{1+} ions in the interstitial sites within the ZrO_6 octahedron and PO_4/SiO_4 tetrahedra and figure 2.2(a) is the structure of NZP, with the atomic positions of various atoms shown, the Oxygen is seen bridging the P and Zr polyhedra. The counter ion Na^{1+} is located in the specific M(1) site inside the framework.

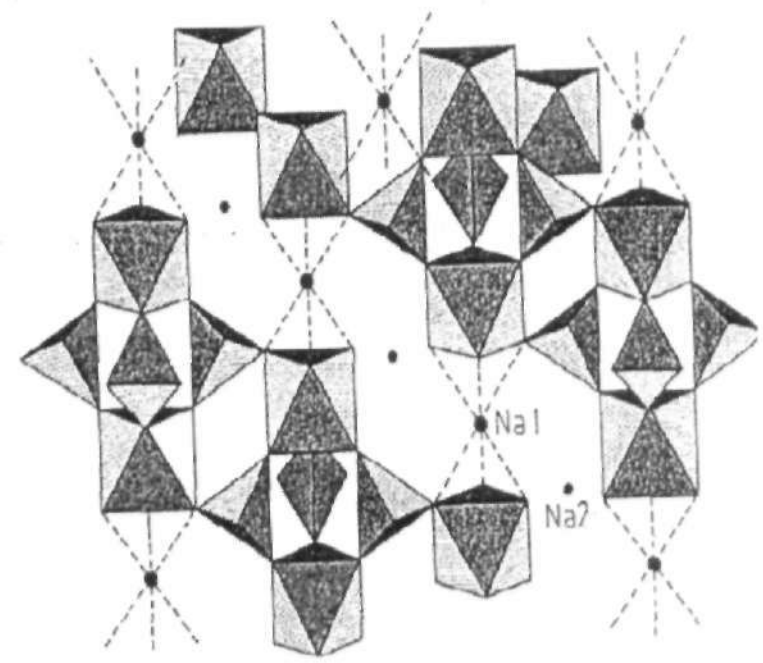
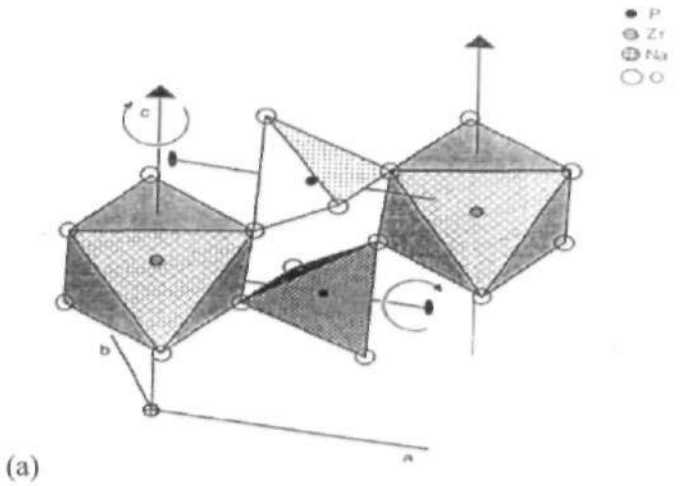
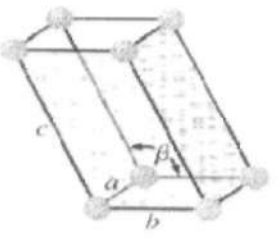


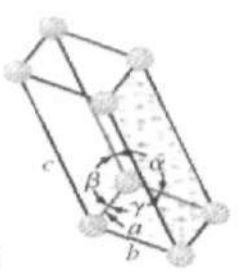
Figure 2.1: View of the rhombohedral *R*-3*c* structure of NASICON showing (ZrP_3O_{12})-units parallel to c axis and Na+ ions in Na1 positions (interstices) octahedrally coordinated by O_2- ions. The Na1 positions are also octahedrally coordinated by empty Na2 positions in the same basal planes as the nearest-neighbour O_2- ions (Gautham, 2006).



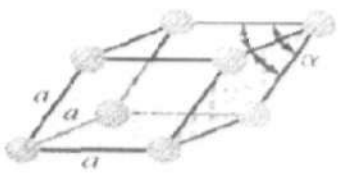
(a)



(b)



(c)



(d)

Figure 2.2(a-d): (a) Corner shared ZrO_6 octahedra and PO_4 tetrahedra in the NZP structure.(Chen, 2003); (b) simple Monoclinic unit cell with $a \neq b \neq c \neq$ and $\alpha = \gamma = 90° \neq \beta$; (c) simple triclinic unit cell with $a \neq b \neq c$ and $\alpha \neq \beta \neq \gamma \neq 90°$ and (d) simple rhombohedral unit cell with $a = b = c$ and $\alpha = \beta = \gamma \neq 90°$ (Paul, 2007).

Another way of representing the general structural formula of NZP in order to reflect the atomic sites is simply M (I) M(II) M(III)$A_{2n}(XO_4)_{3n}$, in which $[A_{2n}(XO_4)_{3n}]^{m-}$ is the rigid framework and M(I), M(II) and M (III), the three distinct empty sites in the framework. Depending on the composition of the material, the symmetry may be lower from R-3c to R-3,C2/c, etc. (Kutucktu, 2005). In compounds with the highest symmetry R-3c, the MI site has three symmetries and coordination number is 6 and lies on the c-axis and this site is generally fully or partially occupied (Leo *et al*, 2002b). The M (II) site has two symmetries and the coordination number is 14 and it lies between the columns and is connected to the M (I) allowing ionic conductivity. It has also been reported that the Na+ cations occupy the MI sites while the MII sites , situated outside the chains-polyhedra-remain empty (Woodcock *et al*, 1999).

Further, as the M (II) is very big, in some cases two cations may fit into the site. The M (III) site is a trigonal prism and has 32 symmetries. It can only accommodate small ions and in most cases it is empty. A and X can be substituted with many different elements, forming hundreds of different compositions (Kutucktu, 2005).The M can be substituted with H^+,Li^+,Na^+,K^+,Rb^+,Cs^+...and A can be substituted with Nb^{5+},Ta^{5+},V^{5+},Sb^{5+},Ti^{4+},Zr^{4+},Hf^{4+},Ge^{4+},Sr^{4+}...and X can be substituted with A^{5+},Si^{4+},Ge^{4+},S^{6+},Mo^{6+},Al^{3+}.Substitution of monavalent Na cation by a divalent Ca or Sr creates an ordering of cations and vacancies in the M1sites, lowering the symmetry to R3bar (Woodcock *et al*, 1999).When substitution of Na by a larger cation is made, such as by K, forming KZP, the unit cell contracts in the a direction and expands in the c direction. This is also true when the Na is substituted by NH^{4+}, the a parameter decreases and the c parameter increases (Kormaneni *et al*, 1986). Similarly, when the Na-O bond length increases with Ti,

coupled rotations of the TiO_6 and PO_4 polyhedra, lead to an expansion in the c and contraction in the a directions.

The different compositions give several different properties to the structure, e.g. ionic conductivity, low and negative thermal expansion, ability to immobilize radioactive nuclides, ferroelectricity and catalytic property. The substitution of M site ions can be done at relatively low temperatures (573K) and the framework ions A and X can be done at higher temperatures >1073K. As the oxidation state of A and X gets higher the framework becomes stronger and the number of different substitutions to the M site increases. Inside the framework $[A_{2n}(XO_4)_{3n}]^{m-}$,$M1^+$ counter ion fully occupy the M(I) vacancy which is located in the c-axis, between two ZrO_6. Zr^{4+} ion has radius which is variously given as 0.72Å and 0.87 Å (Wang and Zhou, 1998; Wu, 2005) respectively. In addition, as the $M1^+$ ion gets bigger the c-axis expands and PO_4 tetrahedra distorts. This distortion increases the O-P-O angle through c-axis and shortens the axis. In an ion exchange study by Mouahid *et al* (2001) on $Na_{1+x}Ti_{2-x}Al_x(PO_4)_3$ (x = 0.60-0.80), in which the Na was substituted by Li, two mobile ions were present in the structure and affected the lattice parameters a, c and other physical properties like conductivity differently, depending on their position on the M sites. The Li entered the M (II) sites which decreased the length of the a axis. The c axis is however more sensitive to the M (I) site composition and therefore the presence of Na in this site caused a variation of the length of the c axis upon ion exchange to be negligible. The presence of Na in the MI site is very important as it results in the' mixed alkali effect', or 'mixed cation effect', as it has been variously referred to. Since the occupancy of Na at the M (I) site is high this made the conductivity due to lithium cations highly difficult across M(I)-M(II) bottlenecks, as the Na^+ may block Li^+ diffusion along the M(I)-M(II) pathway, which may be related

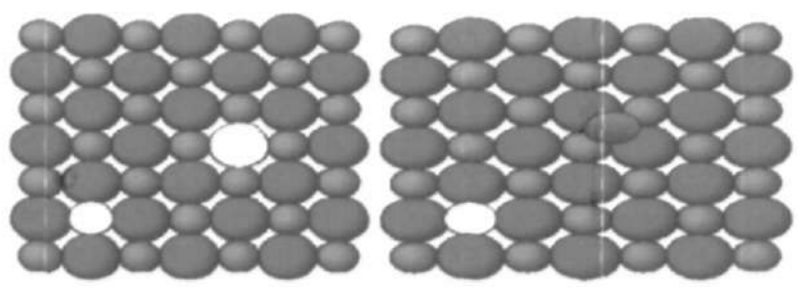
to the 'mixed cation effect' studied mainly in glasses. It has been reported that a pronounced reduction in conductivity is observed in oxide glasses with two or more types of different alkali components when compared to the analoqoue single oxide glasses.

2.3.1 Defect Structure and Ionic Substitution

The understanding of ionic conductivity requires an understanding of defect structure of crystals. Ionic conductivity is due to the presence of defects in the material, impurity or lattice defects that provide conducting channels for ion motion. Understanding of the defects structure is related to the atomic stoichiometry (reaction proportions) of the crystal system and the balancing of thc charges in the system to produce an overall neutral system. It takes energy to create defects in crystals. The presence of defects increases entropy of crystals. Above absolute zero of temperature there are always some intrinsic defects. These defects may occur in isolation due to increase in entropy (disorder) of the crystal, which is called intrinsic point defect, or may occur in isolation to balance the effect of some impurity, called extrinsic point defects. It may also occur throughout the crystal, an effect known as extended defect.

There are two types of intrinsic point defects: Schottky and Frenkel. A Schottky defect consists of a charge balancing cation and anion vacancy found, for example in NaCl. A Frenkel defect is a charge balancing interstitial and vacancy and it consists of cation and anion Frenkel defects. For an ion to move through a crystal, it must hop from an occupied site to a vacant site. Thus ionic conductivity can only occur if defects are present. The two simplest types of point defects are Schottky and Frenkel defects. Frenkel defects may occur either on the anion or cation sublattice.

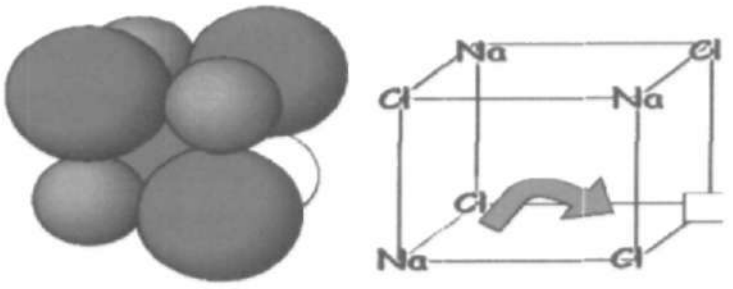
Cation Frenkel defects are common than anion defects, because cations are smaller than anions and easier to accommodate in the interstitial positions. Cationic impurities when introduced into a solid and the dopants does not have the same valence as the cation it is replacing, may result in extrinsic defects being introduced. Real crystals therefore contain both intrinsic and extrinsic defects and the dominant defect type therefore depends on temperature and doping or non stoichiometry level. Examples of Schottky and Frenkel defects are shown in figures 2.3(a-b) for NaCl and AgCl respectively.



(a) **(b)**

Figure 2.3:(a) Schottky Defect in NaCl and (b) Frenkel Defect in AgCl) (Woodward, 2003)

The ion migration, i.e., Schottky Defects, is shown in the figure 2.4(b). Consider the movement of Na^+ ions in NaCl via vacancies originating from Schottky defects. The Na^+ ion must squeeze through the lattice, inducing significant local distortion/relaxation. This is one factor that limits the mobility of ions. A second factor that contributes is the relatively high probability that the ion will jump back to its original position, leading to no net ionic migration.



(a) (b)

Figure 2.4: (a) cubic atomic arrangement for NaCl and (b) the migration of Na ion in the lattice, showing Na ion vacancy (Woodward, 2003).

To get across the unit cell into the vacancy, the Na^+ ion must hop through the center of the cube where it squeezes by 4 Cl^- and 2 Na^+. The energy of this "transition state" will determine the ease of migration. The ion migration (Frenkel Defects) in AgCl can migrate via two mechanisms, as shown in figure 2.5(a-b) and figure 2.6 (a-b) respectively, of direct interstitial and interstitialcy mechanisms.

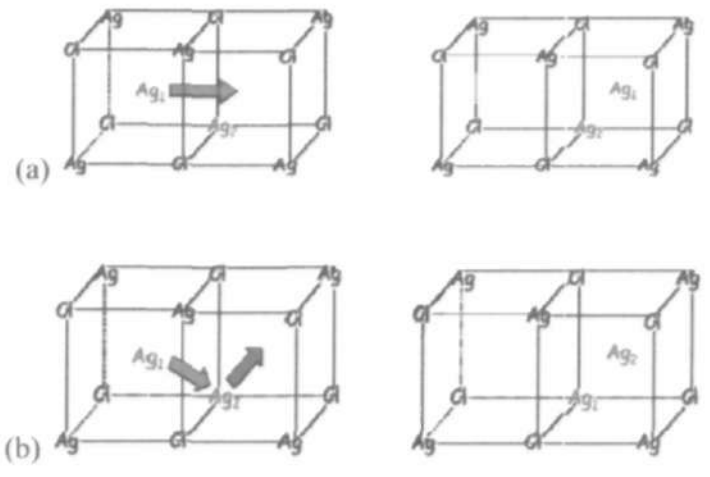


Figure 2.5: (a) Direct Interstitial Jump and (b) Interstitialcy mechanism in AgCl

It must be mentioned that in many compounds it is possible to replace a metal atom or ion with another element that has similar size and bonding requirements.

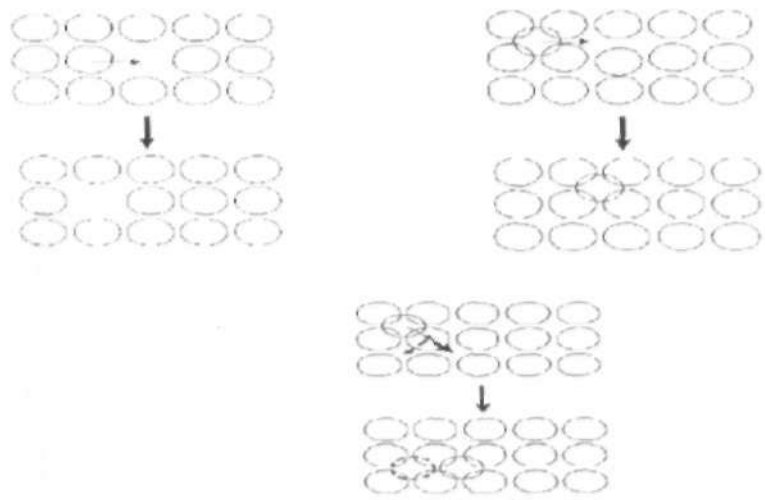
Extensive solid solution formation is favoured by high temperature due to the disorder associated with the solid solution. A homogeneous crystalline structure in which one or more types of atoms or molecules may be partly substituted for the original atoms and molecules without changing the structure is a solid solution (Wikipedia, 2009).

For an ionic solid, typically the ion size difference should be less than 15-20% (Woodward, 2003) to get complete solid solution formation. Greater than 30% size difference usually precludes solid solution formation. The end member of solid solution should have same structure if complete solid solution is to form. Sometimes the solid solution involves the insertion of atoms into interstitial sites in a parent structure, as is the case with the NZP. In the system, the Li replaces some of the Na at the various interstitial sites that are three-dimensionally interconnected channels.

When an ion is replaced by one with different oxidation state (aliovalent substitution) there has to be a charge compensation mechanism. For example, cation vacancies are produced when calcium is doped into NaCl, and this will be represented as-$Na_{1-2x}Ca_{2x}V_xCl$. Interstitial ions aliovalent substitution are not common due to limited size of interstitial sites. However aliovalent anion substitution vacancies are important in ionic conductors such as $Zr_{2-x}Ca_xO_{2-x}$, , where Ca^{2+} is substituting the Zr^{4+} with subsequent insertion of vacancies in the anion sublattice of oxygen to compensate for charge.

In this work Na is being substituted by Li at the interstitial positions and has the same oxidation state with Na, there is no compensation of charge required. The evidence for the formation of a solid solution in such a system is typically by measuring the lattice constants of the materials using X-ray diffraction. The lattice

constants typically vary linearly with solid solution composition. With the aid of density determination, the mechanism of solid solution formation may be worked out. Both defects, Frenkel or Schottky result in the presence of vacant sites in the crystal and any ion in the immediate vicinity can jump to one of the vacant sites, leaving the previous site of the ion vacant, which could now host another ion. There are three mechanisms, as indicated in figure 2.6(a-b) for ion motion, leading to conductivity: *vacancy migration*, *interstitial migration* and *interstitialcy mechanism*- which is a co-operative mechanism involving a chain of ions.



b)

Figure 2.6: (a): Vacancy and interstitial atom and (b) interstitialcy mechanism showing two possible locations of ions after movement (Gautham, 2006).

Ion conductors are classified in various ways, based on the parameters used in describing the materials: cationic/anionic, morphological, crystalline/non-crystalline and diffusion/conduction mechanisms. However, one useful method is by Kumar and Yashonath (2006) which is based on concentration of defects, classified them into three types. Type I Ionic conductors have low concentration of defects ~ 10^{18} cm^{-3} at

room temperature and are found in poor ionic conductors, e.g. NaCl, KCl, etc. In Type II, the solids have high concentration of defects ~10^{20} cm^{-3} at room temperature, e.g. ZrO_2, CaF_2 and are generally good ionic conductors at room temperatures and fast ion conductors at higher temperatures. Type III are reserved for the best superionic conductors like Na-β alumina and $RbAg_4I_5$ in which the mobile ion concentration is typically 10^{22} cm^{-3} and at least one type of the ions contained in the crystal is highly delocalized over the available sites.

The structure of materials is readily studied by diffraction methods. Structural properties are often responsible for several physical and chemical properties such as electrical conductivity, chemical stability and toughness. X-ray diffraction methods are some of the most powerful characterization tools known by scientists. In Solid State Physics they are needed for structural characterizations, lattice parameter and phase determination and can be used for single crystals, powders and amorphous materials.

2.4 X-ray Powder Diffraction

All crystalline solids have their characteristic powder diffraction patterns which are used as their 'finger printing'. However, powder diffraction can be used for study of polymorphism, phase transitions, solid solutions formation, particle size measurements and phase diagram measurements (Ozmen, 2004). There are many forms of crystalline solids, such as single crystal that is pure and free from defects and where structure can be modified by defects and specific impurities; a powder, that is a large number of crystals, polycrystalline solid pieces, e.g. pellet or ceramic tube in which a large number of crystals are present in various orientations or a thin film. Non crystalline solid materials can be amorphous or glassy. The characteristic powder pattern of most known inorganic solids can readily be identified.

X-ray powder diffraction methods can be used to study the degree of crystallinity of a material, to obtain the basic structure of the material and to evaluate the degree of purity and crystallinity of sample under study. In most cases CuKα radiation is used for studies of powders. The samples are usually moved at angles 2θ of 5-60° or larger. A proportional counter is often used as a detector and the intensities of the diffraction peaks are recorded on a chart recorder or stored on a computer.

X-ray powder diffraction can be used for quantitative determination of mineralogical components in a mixture provided that appropriate standards are used. The detection limit of x-ray powder diffraction is usually around 5%. A random orientation of the powder is required in order to observe all of the diffraction peaks. Once the 2θ values are collected they can be converted to θ and by using Bragg's law values of the d-spacing can be obtained. If the substance is a common type then the

experimental X-ray diffraction pattern can be compared to known published patterns such as those found in the ASTM (American Society for Materials and Testing) tables or PDF (Powder Diffraction File database). If a powder pattern has never been collected before analogies to known structural types can be made. During the analysis it is important to compare the peak positions, relative intensities and the general shape of the background signal.

X-ray powder diffraction patterns are a set of lines or peaks each of which are in different intensities and positions (d-spacings) or Bragg angles θ on a strip of photographic film or chart paper. For a given substance the line positions are fixed and characteristic for that substance. The intensities may vary from sample to sample depending on the method of sample preparation and the instrument. In x-ray powder diffraction the average crystallite size in a powder sample and the average diameter is less than 2000Å (2×10^{-7}m) (Ozmen, 2004). The lines in a powder diffraction pattern are of finite breadth but if the particles are very small the lines are broader than usual. The broadening increases with decreasing particle size. The limit particle size to be seen is between 20 to 100Å (Ozmen, 2004).Crystalline solids give a number of patterns that have a number of sharp lines. Phase identification using XRD relies on the positions of the peaks in the diffraction profile, and to some extent on the relative intensities of these peaks. The shape of the peaks, particularly, the width, is a measure of the amplitude of thermal oscillations of the atoms at their regular lattice sites, they can also be a measure of vacancy and impurity element concentrations. Any factor which results in a distribution of d-spacings (Sakuma, 2006). Crystallite size can also cause peak broadening, as explained by the Scherer equation. Crystalline solids like glasses and gels give diffraction patterns that have a small number of very broad lines with low intensity. The thermal motion of atoms, which is inevitably present in all

substances above absolute zero, causes a reduction in peak intensity and an increase in the background radiation. This is mostly noticed at high temperatures and as the melting point is approached.

The X-ray diffraction pattern for this work was collected using difractometer MD-10 in the 2θ range 16-70°. The information in an XRD pattern is a direct result of two factors: 1) the size and shape of the unit cells, which determine the relative positions of the diffraction peaks and 2) the atomic positions within the unit cell, which determine the relative intensities of the diffraction peaks (Kalu *et al*, 2008). There are many X-ray data refinement software that are used to refine various parameters of the structure such as Rietveld refinement using the GSAS (General Structure Analysis System) suite of programs (Larson and Von Dreele, 2004) or its newer and improved version RIETAN, which was developed to simplify and eliminate certain problems in the GSAS (Izumi, 1989; Mascocchi, 1997; Kleeberg, 2005). However, refinement is excluded from this work due to the limited XRD 2θ range acquired. The X-ray beam are normally produced from a special X-ray tube that emits monochromatic radiation. The wavelength depends on the metal used for the target of the X-ray tube. When the monochromatic beam strikes the sample some of the X-rays are diffracted from certain planes of the crystal lattice of the specimen; the angles at which they are diffracted are unique to the spacing of the atoms in the crystal of the material. The diffraction process occurs when the Bragg's law (condition) is satisfied and is expressed as: $n\lambda = 2dsin\theta$, where λ is the wavelength of X-rays, d is the interplanar spacing, θ is the X-ray angle, n is an integer.

2.4.1 Determination of Structure of NZP

In order to determine the structure of the system, which was indexed based on a hexagonal lattice, a geometric analysis of the structure is necessary. In this case the hexagonal closed-packed (HCP) structure geometry is presented as follows. The HCP structure is represented as an atom at each of 12 corners of a hexagonal prism, 2 atoms at top and bottom face and 3 atoms in between top and bottom face, figure 2.7 (a-c), where (a) is the schematic of the crystal structure (b) hard sphere model and (c) an isolated unit cell. Atoms attain higher Atomic Packing Fraction (APF) by attaining HCP structure than simple hexagonal structure. The coordination number is 12, Atomic Packing Fraction, APF = 0.74.

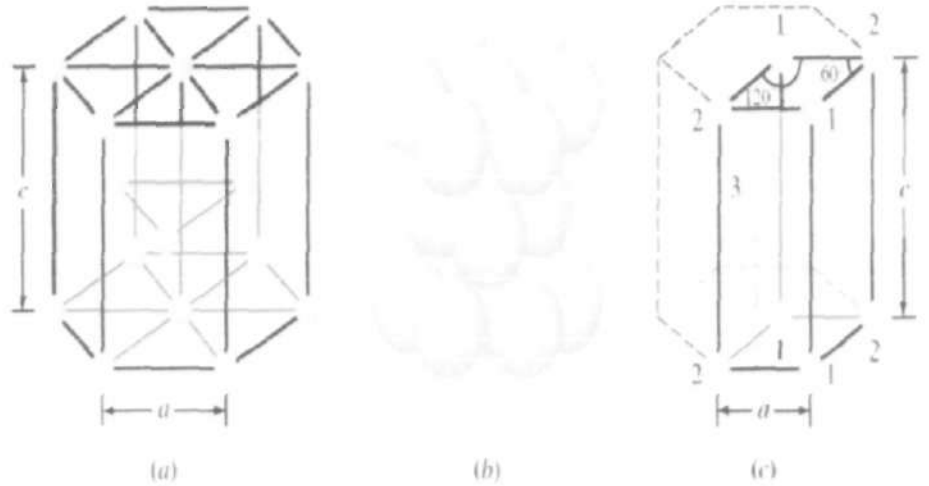


Figure 2.7 : Each atom has six 1/6 atoms at each of top and bottom layer, two half atoms at top and bottom layer and 3 full atoms at the middle layer. Therefore each HCP unit cell has (2 x 6 x 1/6) + (2 x ½) + 3 = 6 atoms (a) schematic of the crystal structure b) hard-sphere model c) isolated unit cell schematic (Paul, 2007)

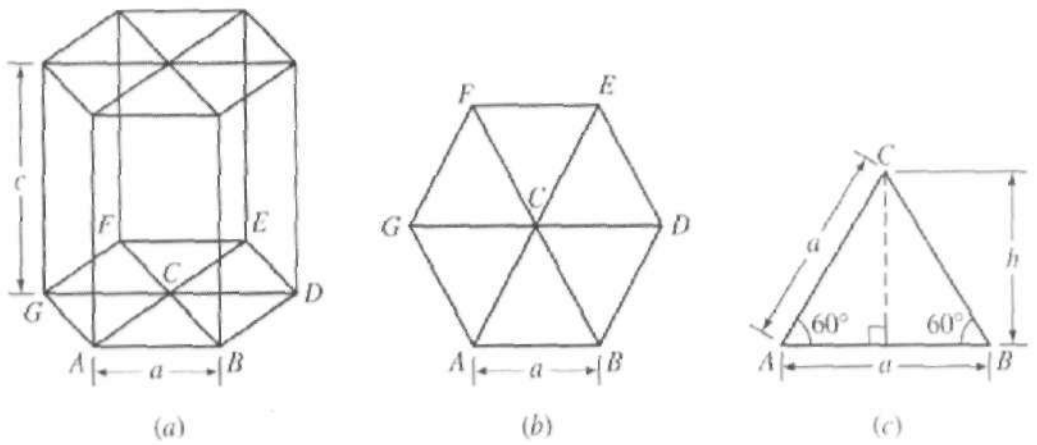


Figure 2.8 (a-c): Geometrical dimensions of the hexagonal cell (Paul, 2007).

X-ray diffraction process occurs when the Bragg's law (condition) is satisfied and it is expressed as:

$$n\lambda = 2dsin\theta \qquad (1)$$

where λ is the wavelength of X-rays, d the interplanar spacing, θ the X-ray angle and n is an integer. For a hexagonal system (assuming n=1), the d-spacing is given by

$$\frac{1}{d^2} = \frac{4}{3}\left(\frac{h^2+hk+k^2}{a^2}\right) + \frac{l^2}{c^2} \qquad (2)$$

Squaring equation (1) :

$$\lambda^2 = 4d^2sin^2\theta \; OR = \frac{\lambda^2}{4d^2} \qquad (3)$$

Combining (2) and (3):

$$\frac{1}{d^2} = \frac{4}{3}\left(\frac{h^2+hk+k^2}{a^2}\right) + \frac{l^2}{c^2} = \frac{4sin^2\theta}{\lambda^2} \quad (4)$$

Rearranging the equation:

$$sin^2\theta = \left(\frac{\lambda^2}{4}\right) = [\frac{4}{3}\left(\frac{h^2+hk+k^2}{a^2}\right) + \frac{l^2}{c^2} \quad (5)$$

Since a, c are constants for any given diffraction pattern

$$sin^2\theta = A(h^2 + hk + k^2) + Cl^2 \quad (6)$$

Where

$$A = \frac{\lambda^2}{3a^2} \text{ and } C = \frac{\lambda^2}{4c^2} \quad (7)$$

The values of A and C when determined analytically, are constants on which the lattice parameters a and c depend. Thus the lattice parameters of the hexagonal cell can be calculated. Since h, k, and l are always integers, $h^2 + hk + k^2$ can only have values like 0, 1, 3, 4, 7, 9, 12... and l^2 can only have values like 0, 1,4, 9, ...That is by substituting various combination of values of h,k and l.

2.4.2 Determination of Density and Crystallite Size

Theoretical density of the sample can be calculated from :

$$\rho = \frac{nA}{V_c N_A} \tag{8}$$

where n is number of atoms associated with each unit cell and it is equal to 6, A is atomic weight of $Na_{1-x}Li_xZr_2(PO_4)_3$, V_c is volume of the unit cell ($V = abc\ \text{Å}^3 = a * 2\sin 60 * c\ \text{Å}^3$),$N_A$ the Avogadro's number (6.023 x 10^{23}atoms/mol). The theoretical density was calculated for all the compositions using the Microsoft EXCEL Program.

The average crystallite size from the Scherer equation is given as:

$$t = \frac{K*\lambda}{B*cos\theta_B} \tag{9}$$

where, t *is* thickness of crystallite, K the constant, dependent on crystallite shape (0.89), λ *is the* X-ray wavelength, B *the* FWHM (full width at half max) or integral breadth, and θ_B the Bragg angle ,where $B = (2\theta\ High) - (2\theta\ Low)$ and is the difference in angles at half maximum of peak diameter. Scherer's Formula is used when crystallite size <1000 Å. Peak broadening may be observed which may be due to factors such as, Size, Strain and Instrument as observed earlier. If breadth is consistent for each peak, then broadening is due to crystallite size. K depends on definition of t and B and is within 20-30% accuracy at best (Tennyson, 2009).This value was also calculated based on the XRD results from the Microsoft EXCEL Program for each 2θ value.

2.4.3 Scanning Electron Microscopy

Scanning electron microscopy (SEM) is a method for high-resolution imaging of surfaces. The SEM uses electrons for imaging, much as a light microscope uses visible light. The advantages of SEM over light microscopy include much higher magnification (>100,000X) and greater depth of field up to 100 times that of light microscopy (MEE, 2006). Qualitative and quantitative chemical analysis information is also obtained using an energy dispersive X-ray spectrometer (EDX) with the SEM. The principal components of the SEM system are shown in figure 2.9.

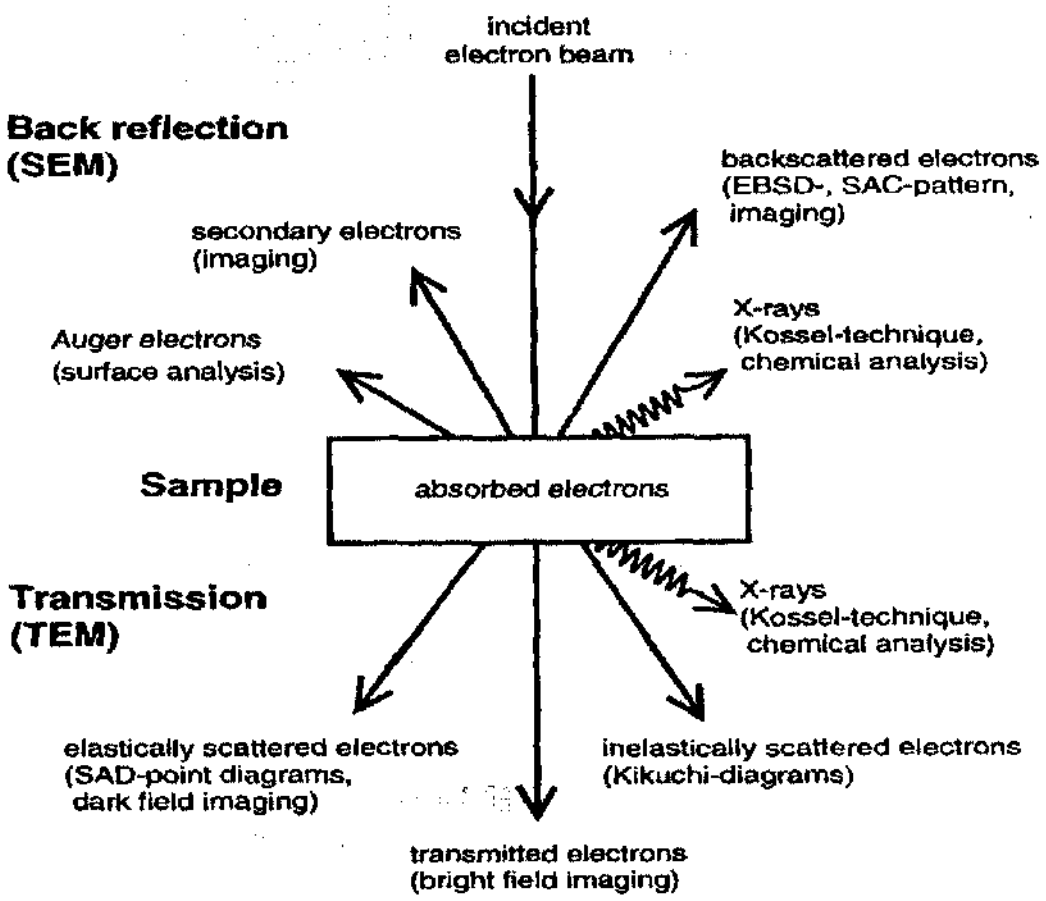


Figure 2.9 : Summary of the various signals obtained by interaction of electrons with matter in an electron microscope (Rollet and Kalu, 2008).

The SEM generates a beam of incident electrons in an electron column above the sample chamber. The electrons are produced by a thermionic emission source, such as a heated tungsten filament, or by a field emission cathode. The energy of the incident electrons can be as low as 100 *eV* or as high as 30 *keV* depending on the evaluation objectives. The electrons are focused into a small beam by a series of electromagnetic lenses in the SEM column. Scanning coils near the end of the column direct and position the focused beam onto the sample surface. The electron beam is scanned in a raster pattern over the surface for imaging. The beam can also be focused at a single point or scanned along a line for X-ray analysis. The beam can be focused to a final probe diameter as small as about 10 Å.

The incident electrons cause electrons to be emitted from the sample due to elastic and inelastic scattering events within the sample's surface and near-surface material. High-energy electrons that are ejected by an elastic collision of an incident electron, typically with a sample atom's nucleus, are referred to as backscattered electrons. The energy of backscattered electrons will be comparable to that of the incident electrons. Emitted lower-energy electrons resulting from inelastic scattering are called secondary electrons. Secondary electrons can be formed by collisions with the nucleus where substantial energy loss occurs or by the ejection of loosely bound electrons from the sample atoms. The energy of secondary electrons is typically 50 *eV* or less.

To create an SEM image, the incident electron beam is scanned in a raster pattern across the sample's surface. Electron microscopy provides a versatile technique capable of providing structural information over a wide range of magnifications. The SEM studies the texture, topography and surface features powder or solid pieces. The resulting pictures have a three–dimensional quality. Figure 2.9.1

is the SEM image from a metal Foam. The resolution of SEM is approximately between 100Å and 10μm (Ozmen, 2004).

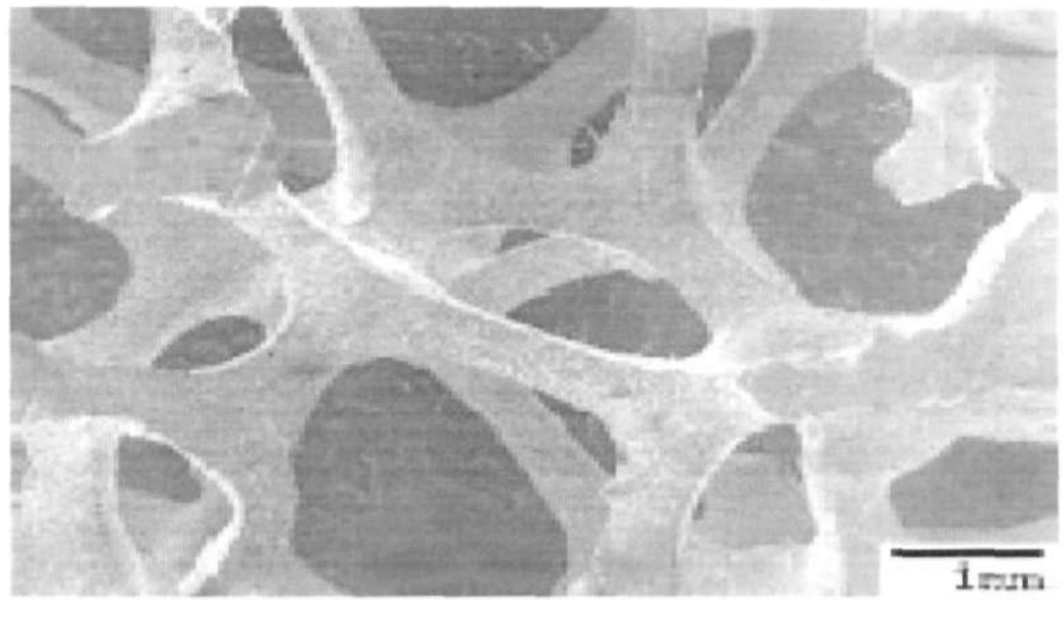


Figure 2.9.1: SEM Image of Metal Foam Structure

2.5 Arrhenius Conduction

Some methods of measuring ionic conductivity include, far Infrared and Raman spectroscopy, where the vibration of the atoms can provide hop attempt frequencies and motional narrowing of the NMR absorption lines, among others (Smith, 2005). These however, are non ac methods. The discussion shall be limited to dc and ac electrical conductivity (Jaeger *et al*, 1998) measurements and to some extent NMR.

Conductivity may be fully or partly ionic. In the former case it may be due to the positive and negative ion species, while in the latter case it may be due to electronic contribution due to negative electrons and positive holes that may be present. Thus total ionic conductivity may not be the true bulk ionic conductivity due to factors, such as electrode–material contact resistance, generally of negligible fraction of total resistance in high resistance samples. This is useful only if it is

ensured that the signal makes the electrode-material system linear. There is also the problem of grain-boundary resistance whose only solution is to carry out measurements on single crystals (Kumar and Yashonath, 2006). For most superionic conductors the art of growing single crystals is far from developed, measurements are therefore carried out on pressed pellets. Grain boundaries can either increase or decrease the conductivity, depending upon whether or not the activation energy for conduction for the grain boundary is less or more than the bulk conduction. In dc conduction, polarization effects at the nearby electrodes are a major problem in the evaluation of ionic transport. However, static fields are useful in separating electronic components of conductivity. Table 2.1 is a comparison of electrical conductivity of various ionic materials and that of metals, while figure 2.9.2 shows the Arrhenius plots of typical ionic conductors with that of NASICON indicated with an arrow, it exhibits high conductivity at relatively low and high temperatures.

Taking into account the geometrical aspects i.e. the thickness (t) and the surface area (A) of the solid electrolyte, the conductivity was calculated from according to the formula:

$$\sigma = \frac{t}{AR} \tag{10}$$

where R represents the real part of the complex impedance measured at different temperatures. The factors that influence conductivity in the solid state include concentration of charge carriers, temperature of the crystal, the availability of vacant accessible sites, and the ease with which an ion can jump to another site. The most important is the last, which is a measure of the activation energy because of its exponential relation to temperature. Ionic conductivity, σ_i arises when an electric field

E is applied to an ionic solid. A current density J, developed in the material is given by:

$$J = \sigma_i E \tag{11}$$

σ_i is related to mobile ion density N, Z the atomic number, the mobile ion charge (Ze) and the velocity of the mobile ion per unit electric field or ion mobility, μ

$$\sigma_i = N(Ze)\mu \tag{12}$$

ion mobility changes with temperature as

$$\mu = \mu_\circ \exp\left(-{}^{E_a}/_{kT}\right) \tag{13}$$

thus,

$$\sigma T = \sigma_\circ \exp\left(-{}^{E_a}/_{kT}\right) \tag{14}$$

where ,

$$\sigma_\circ = NZe\mu_\circ \tag{15}$$

and E_a is the electrostatic energy barrier(activation energy) that the ion has to overcome in order to hop from one site to another in the crystal. Eq. (14) is called the Arrhenius equation. The activation energy can be determined from the plot of $ln\ (\sigma T)$ $Vs\ {}^{1}/_{T}$, (the Arrhenius plot), where T is the absolute temperature.

Table 2.1: Comparison of electrical conductivities of different materials (Paul, 2007).

	Material	Conductivity ($S\ m^{-1}$)
Ionic conductors	Ionic crystals	$< 10^{-16} - 10^{-2}$
	Solid Electrolytes	10^{-1}-10^{3}
	Liquid electrolytes	10^{-1}-10^{3}
Electronic conductors	Metals	10^{3}-10^{7}
	Semiconductors	10^{-3}-10^{4}
	Insulators	$< 10^{-10}$

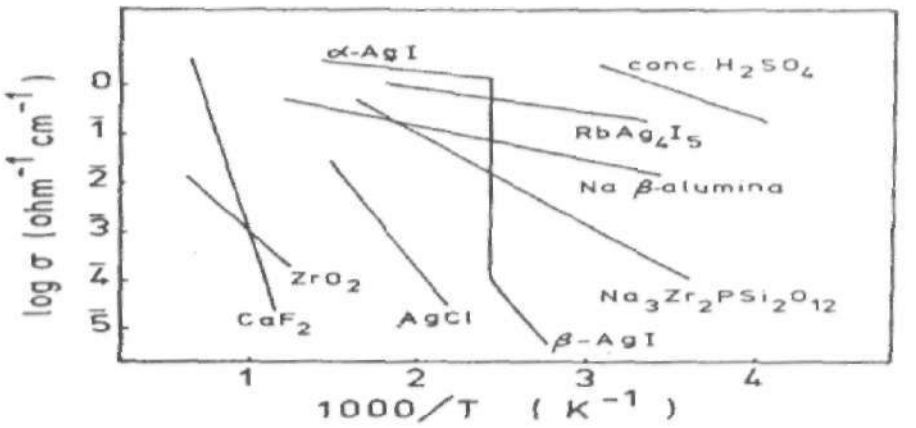


Figure 2.9.2: The Arrhenius conductivity plots for different materials at different temperatures (Woodward, 2003).

2.5.1 Impedance Spectroscopy

Impedance spectroscopy (IS) is a relatively new and powerful tool for characterizing many of the electrical properties of materials and their interfaces with electronically conducting electrodes. It can be used to investigate the dynamics of bound or mobile charge in the bulk or interfacial regions of any kind of solid or liquid material: ionic, semiconducting, mixed electronic–ionic, and even insulators (dielectrics). Impedance measurement can also be used at the microscale level by use of microscale impedance devices (Lee *et al*, 2004) with various applications. These devices can be fabricated to interrogate femtolitre subdomains within nanolitres of total sample solutions (Ayliffe *et al*, 1999). IS has also been used in the study of mixed electronic ionic conductor (MIECS), coatings, bioelectrical processes and corrosion (Lai and Haile, 2005).The method has similarly, been used to assess the viability of the rapid chloride test for determining concrete conductivity such as Portland cement paste (Synder *et al*, 2000).

Impedance spectroscopy is carried out over a wide range of frequencies in order to identify all the time constants in the circuits, usually ten frequencies per decade are used (Lasia, 1999). There are several programs for modeling IS. Although it should be stressed that IS is a very sensitive technique, as it does not provide a direct measure of physical phenomena, other electrochemical experiments have to be carried out, together with good physical knowledge of the system (surface composition, thickness, porosity, the presence of various layers, etc.). Interpretation of impedance data requires the use of an appropriate model. This is quite a difficult task that must be carried out very carefully. The modelling may be classified as (1) physicochemical, process, or structural, modelling and (2) measurement, formal, or mathematical modelling. Process modelling links measured

impedances with physicochemical parameters of the process (kinetic parameters, concentrations, diffusion coefficients, sample geometry, conditions, etc.). Measurement modelling explains the experimental impedances in terms of mathematical functions in order to obtain a good fit between the calculated and experimental impedances. In the latter case, the parameters obtained do not necessarily have a clear physicochemical significance. One such modelling is the so-called complex nonlinear least squares (CNLS) fitting. Experimentally obtained impedance data for a given electrode–materials system may be analyzed by using an exact mathematical model based on a plausible physical theory that predicts theoretical impedance or by a relatively empirical equivalent circuit whose experimental impedance predictions are given (Macdonald and Johnson, 2005). In either the case of the relatively empirical equivalent circuit or of the exact mathematical model, the parameters can be estimated and the experimental impedance data compared to either the predicted equivalent circuit impedance or to the theoretical impedance. The method chosen here is to model it to an equivalent electrical circuit.

Analysis of experimental data that yield a full semicircular arc in the complex plane can lead to quantitative estimates of conductivity, relaxation times, and interfacial capacitance. In practice, however, experimental data are only rarely found to yield a full semicircle with its centre on the real axis of the complex plane. There are three common perturbations which may still lead to at least part of a semicircular arc in the complex plane:1) the arc does not pass through the origin, because there are other arcs appearing at higher frequencies, 2) the centre of an experimental arc is frequently displaced below the real axis, because of the presence of distributed elements in the material–electrode system. The relaxation time is then not single

valued but is distributed continuously or discretely around a mean value. The angle by which such a semicircular arc is depressed below the real axis is related to the width of the relaxation time distribution and as such is an important parameter; the 3) arcs can also be substantially distorted by other relaxations whose mean time constants are within two orders of magnitude or less of that for the arc under consideration. The experimentally obtained spectra often differ strongly from the idealized ones presented. The semi-circles may overlap, and the degree of overlapping depends on the relative time-constants. The closer they are, the bigger is the mixing (Vladicova, 2003).

In an ideal polycrystalline sample, the Nyquist plot exhibits an arc at high frequency (first semicricle), a second (second semicircle) arc at lower frequencies, and a linear portion at the lowest frequencies, as shown in figure 2.9.3(a). The corresponding circuit model is shown in figure 2.9.3(b). Two parallel *RC* circuits and a constant phase element (Q_e) (used as equivalent circuit element instead of the conventional capacitance and the property varies from that of resistance and indutor also, depending on the value of some expeonent, section 2.5.2). The absence of this component has been attributted to the reason why impedance arcs terminating at the origin (Anantharamulau, 2008). The frequency is increasing from right of the smaller semicircle to left of the bigger. The first circuit (R_1, C_1) is assigned to represent the grain interior behaviour, the second one the grain boundary (R_2, C_2) behaviour, while the third one is the electrode (Q_e) behaviour. ω_o is the relaxation frequency, and is the freqquency at the maxximum imaginary impedance, section 2.5.2. R_bC_b is the time constant τ of the circuit, while the symbols represent the bulk resistanvce and capance, respectively.

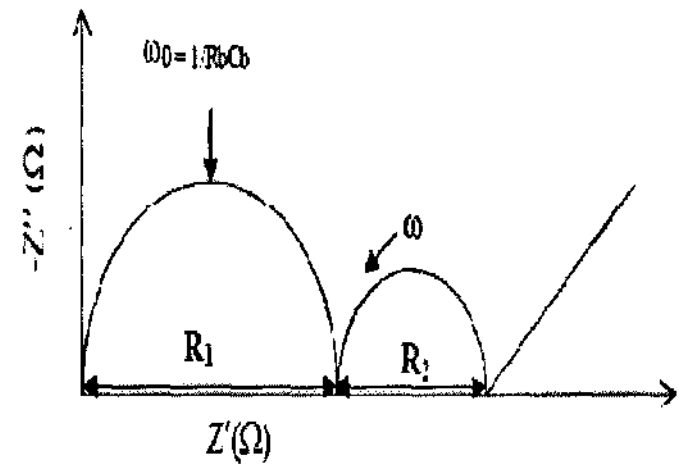


Figure 2.9.3(a): A typical Nyquist plot for a polycrystalline material. The real and imaginary components of impedance are plotted as parametric functions of frequency

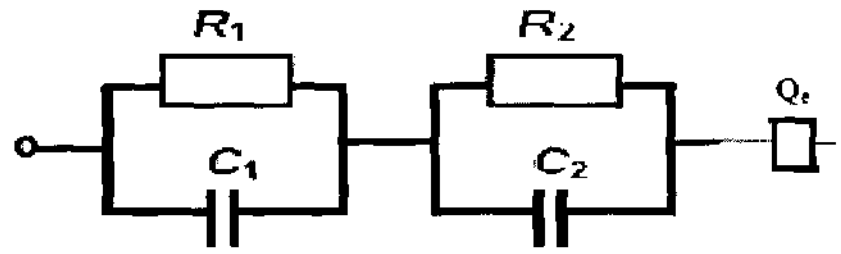


Figure 2.9.3(b): Equivalent circuit model of a polycrystalline material in which components in parallel have been lumped together

The measurement of the bulk conductivity is straightforward from the Nyquist plot, while the measurement of specific grain boundary conductivity requires knowledge of the grain size and grain boundary thickness. In order to determine the grain boundary conductivity without detailed micro-structural and electrical information, a "Brick Layer Model" (BLM) has been adopted (Bonanos *et al*, 2005), as shown in figure 2.9.4,

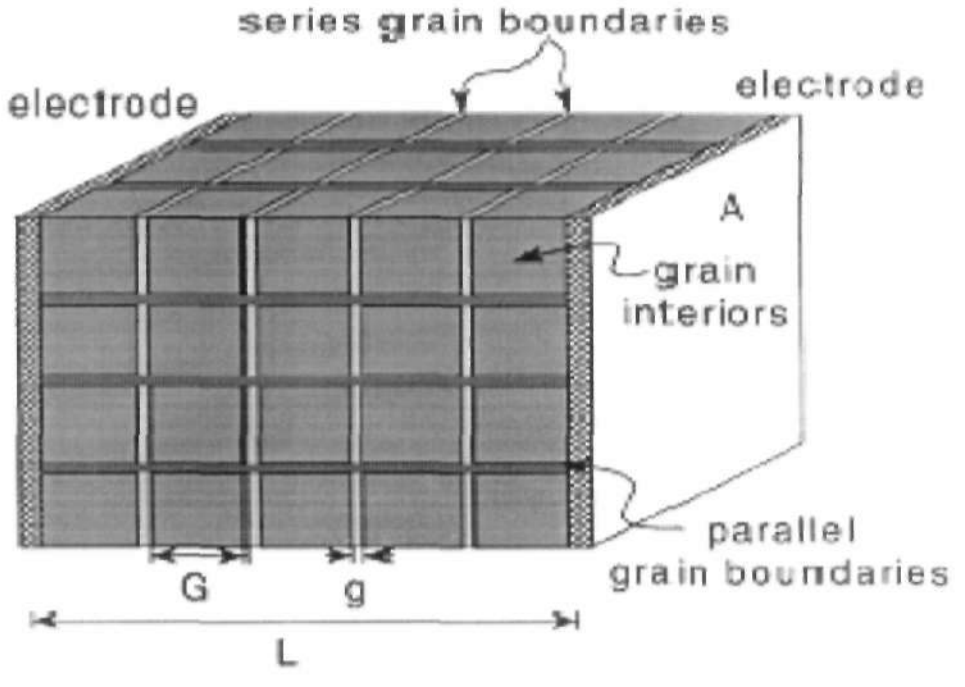


Figure 2.9.4: Brick Layer Model of a polycrystalline material. Grains are assumed to be cube-shaped, and grain boundaries to exist as flat layers between grains.

where L is the sample length, A is the sample cross sectional area, G is the edge length of the grains and g is the grain boundary thickness. This model is used owing to its high symmetry and the simplicity of the grain shape. Though the validity and limits of the Brick Layer Model has been highlighted too (Fleig and Maier, 1998; Fleig *et al*, 2000). Here, the conclusions that have been derived from the BLM analysis will be used in this study and have been summarized below.

Define σ_{bulk} and σ_{gb} as the specific conductivity of the bulk and grain boundary, respectively. For the situation where $\sigma_{bulk} > \sigma_{gb}$ and $g << G$, the bulk conductivity is described as :

$$\sigma_{bulk} = \frac{L}{A}\ \frac{1}{R_1} \tag{16}$$

while σ_{gb} can be obtained in terms of the ratio $R1$ to $R2$ and $^{g}/_{G}$

$$\sigma_{gb} = \left(\frac{g}{G}\right) \frac{R_1}{R_2}\, \sigma_{bulk} \tag{17}$$

The parameter $^{g}/_{G}$ is available from the dielectric constant of the bulk and grain boundary:

$$\frac{g}{G} = \frac{C_1}{C_2} \tag{18}$$

where $C = {}^{1}/_{R\omega_\circ}$, as described in figure 2.9.3(a). The capacitnaces of the bulk and grain boundary are represented by C_1, C_2. The grain boundary conductivity derived by this means is called "specific grain boundary conductivity."

Polycrystalline materials with uniform composition of the grains and grain boundaries show only one bulk and one grain boundary semicircle regardless of the fact whether the grains and grain boundaries are of uniform thickness or not. That conclusion comes from the independence of the characteristic time-constant on the thickness (Vladicova, 2003). Macdonald and Johnson (2005) have reported that the effects of densification by sintering a polycrystalline electrolyte will reduce the magnitude of the resistance across the grain boundaries and simultaneously decrease the surface area associated with the interface capacitance.

Impedance spectroscopy measurement can be carried out by the application of a small periodic voltage perturbation (sinusoidal) while registering the magnitude and

phase shift of the corresponding current over a wide range of frequencies. For a sinusoidal varying perturbation of the form:

$$V(t) = V_0 e^{j\omega t} \tag{19}$$

where, V is a vector quantity, the resulting current response has in general the form:

$$I(t)) = I_0 e^{(j\omega t - j\emptyset)} \tag{20}$$

The complex admittance Y is defined as the ratio of the complex current $I(t)$ over the complex voltage perturbation $V(t)$ applied to the system. The complex impedance Z is the reciprocal of the complex admittance. Thus considering (21) and (22):

$$Y(t) = {I(t)}/{V(t)} \tag{21}$$

$$Z(t) = (Y^{-1}) = {V(t)}/{I(t)} = {V_o}/{I_o e^{(j\emptyset)}} \tag{22}$$

If the real and imaginary parts of the admittance and impedance are known, the complex admittance and impedance are well defined. Alternatively, the admittance and impedance vectors could be realized if the phase angle and modulus are known.

The real and imaginary parts of Z are:

$$Re\ (Z) = Z' = |Z| \cos \emptyset \tag{23}$$

$$Im(Z) = Z'' = |Z| \sin \emptyset \tag{24}$$

The phase angle and modulus are:

$$\emptyset = \tan^{-1}(Z''/Z') \tag{25}$$

$$|Z| = \sqrt{(Z')^2 + (Z'')^2} \tag{26}$$

Impedance is generally a complex quantity and is only real when $\emptyset = 0$, that is purely resistive, in that case it is also frequency independent. As mentioned earlier, the interface, electrode-electrolyte can be regarded, to a first approximation as a parallel plate capacitor, the rate of charging of which is determined by the bulk ionic resistance of the electrolyte. Tsagarakis (2004) has explained in detail the electrode effects of impedance measurement, a topic which will not be considered here. A typical impedance spectrum for a zirconia based O^{2-} conducting electrolyte (Gautham, 2006) with Pt/O_2 electrodes is shown in figure 2.9.5(b), is characterised by two semicircles in the Z' and Z'' plane, the so called Nyquist plot. The semicircles shown in figure 2.9.5(b) have been attributed by Bauerle (Kidner, *et al*, 2005) to the grain boundary (left semicircle) and the electrode reaction taking place at the interfaces of the solid electrolyte and electrodes (right semicircle), respectively. The equivalent circuit is shown in figure 2.9.5(a) and corresponding impedance spectrum (b). The values of R_1, R_2 and R_3 depicted in figure 2.9.5(a) respectively, represents the grain, grain boundary and of the electrode reactions. This is the conventional way

to assign the observed semicircles followed in most of the reports in the literature. However, it is worth mentioning that Näfe pointed out that the unambiguous assignment of the semicircles is doubtful. Moreover, it is often not feasible to interpret the obtained impedance results in terms of the simplified electrical equivalent circuit (Macdonald, 1987).Thus for this analyses the models of figures 2.9.3(b) and 2.9.6(a and c) have been used based on the analyses of the processes at the relevant frequency domains.

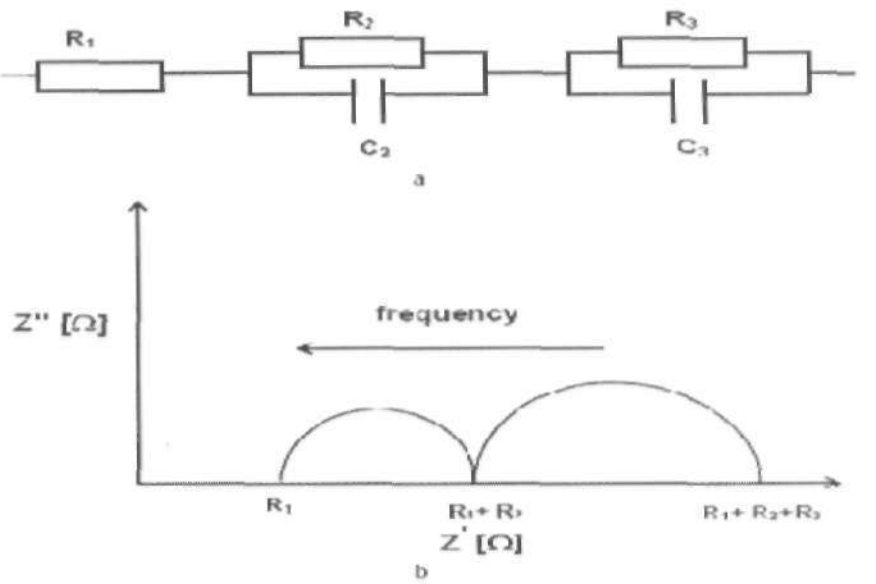


Figure 2.9.5: Typical equivalent circuit (a) and corresponding impedance spectrum (b). The values of R_1, R_2 and R_3 depicted in (a) represents the resistance of the electrode reactions, grain (R_g) and grain boundary (R_{gb}), respectively.

Another anlyses of the impedance spetra has been provided by Furusawa (2006) and is described briefly below (figure 2.9.6). The frequency ω is increasing from right to left as shown by the arrow on the semicircle. It should be noted that the grain semicircle started from the origin (small arc). This has implication for the meaninings of various components of the resistances. The model considers the

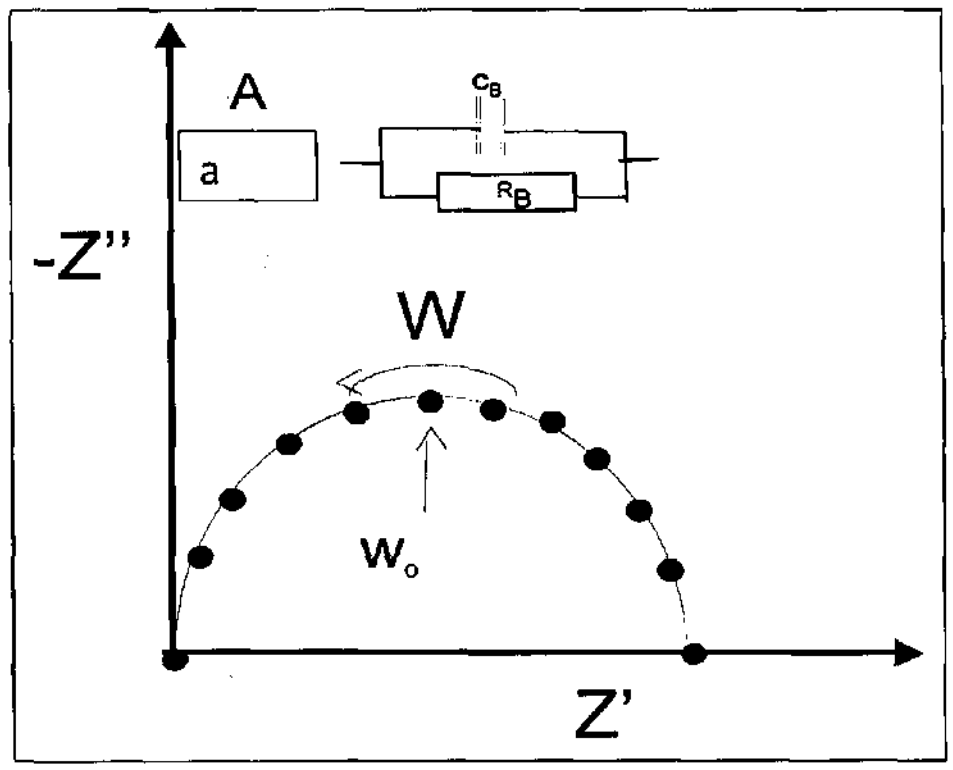
treatment of the simplest case of an ionic conductor as a parallel circuit consisting of a bulk electronic resistance R_B and capacitance C_B which is determined by the dielectric constant ε. According to this model complex impedance $Z^*(\omega)$ at angular frequency ω is:

$$Z^*(\omega) = \frac{R_B}{1+j\omega C_B R_B} \tag{27}$$

Where the real and imaginary component of the impedance can be obtained by multiplying the numerator and by the complex conjugate of the denominator.Thus the real part is :

$$R_e Z^*(\omega) = Z'(\omega) = \frac{R_B}{1+(\omega C_B R_B)^2} \tag{28}$$

and the imaginary part is:



$$ImZ^*(\omega) = Z''(\omega) = -\frac{\omega C_B {R_B}^2}{1+(\omega\, C_B R_B)^2} \qquad (29)$$

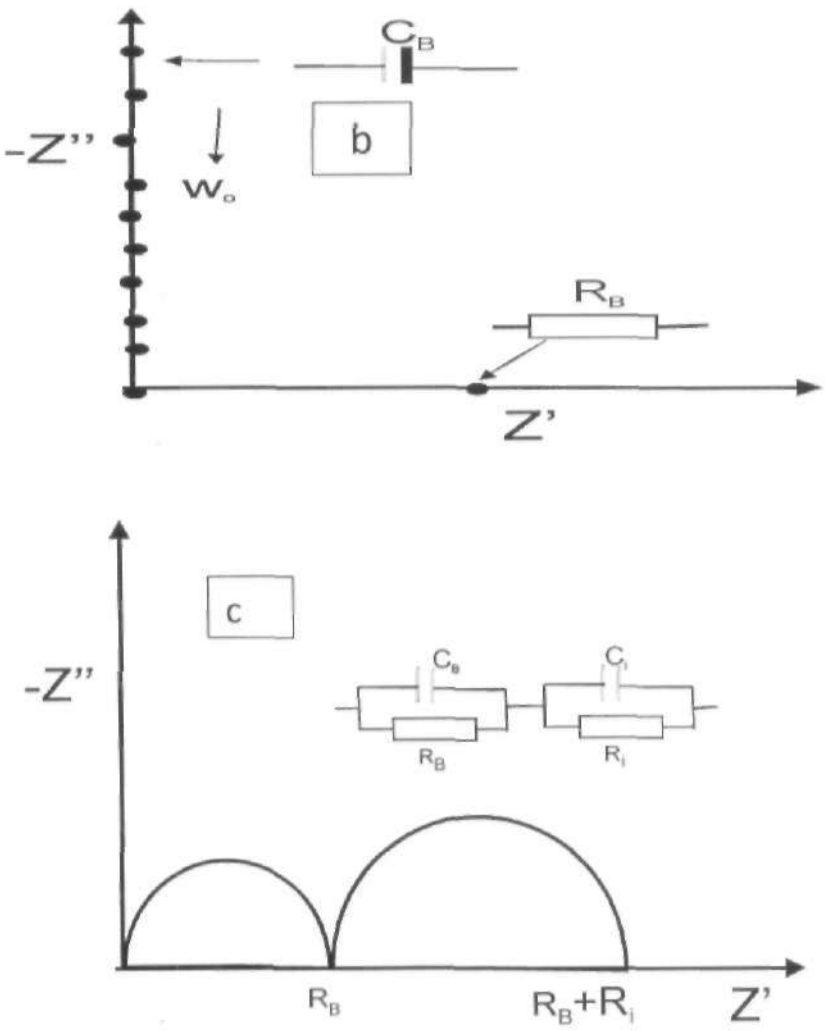


Figure 2.9.6: Comparison of equivalent circuit and impedance plot, a) parallel circuit consisting of a bulk electric resistance R_B and capacitance C_B, b) impedance plot for a single capacitance) and c) typical equivalent circuit which contains the contribution of ionic conduction at interface region (Furusawa, 2006).

Eliminating w from Eq. (28) and Eq. (29), one can obtain,

$$\{Z'(\omega) - \frac{R_B}{2}\}^2 + Z''(\omega)^2 = \left(\frac{R_B}{2}\right)^2 \qquad (30)$$

Geometrically the equation Z' vs $-Z''$ plot is a semicircle radius $\frac{R_B}{2}$ and centre $(\frac{R_B}{2}, 0)$ and thus d.c. resistance R_B can be estimated from the impedance plot. The angular frequency ω_{max} (or ω_O) which gives the top of the semicircle is equal to the reciprocal of the time constant, $\frac{1}{R_B C_B}$. From the value of R_B and ω_{max}, it is possible to estimate C_B. In the case of $R_B << \frac{1}{\omega C_B}$, Eq. (27)$\approx Z^* \approx R_B$, it becomes equivalent to a single resistance and the impedance plot is given by figure 2.9.6(a) (inset). Such a curve is observed in high conductivity materials such as semiconductors and metals. However, in the case $\frac{1}{\omega C_B} \ll R_B$, Eq. (27) becomes $\approx Z^* \approx -j(1/\omega C_B)$, which is equivalent to a single capacitance, figure 2.9.6(b) (in-set). Such a curve is observed in insulators such as quartz and alumina. A typical example of equivalent circuit for contribution of ionic conduction at interface region such as grain boundary is shown in figure 2.9.6(c). In this case the complex impedance Z^* at angular frequency ω is given as:

$$Z^*(\omega) = \frac{R_B}{1+j\omega C_B R_B} + \frac{R_i}{1+j\omega C_i R_i} \qquad (31)$$

Here R_i and C_i are the resistance and capacitance at the interface region, respectively. The real and imaginary compeonents of the impedance can be determined by similar method as described for Eq.(27). The complex impedance plot is shown in figure 2.9.6(c) . Each component can be separated clearly when the time constant $R_i C_i$ is 2 or more order of magnitude larger than $R_B C_B$ (Furasawa, 2006).

However, when the time constant R_BC_B and R_iC_i are close, each process cannot be separated and the impedance plot traces become a distorted semicircular arc. The low frequency region of the impedance is also largely affected by the formation of electronic double layer capacitance and electrochemical reaction around the ionic conductor–electrode interface region. In the case of the blocking electrode the IS spectrum is greatly affected by the electric double layer (C_{dl}) capacitance at the electrode. Thus the IS of the electrode is also given by parallel circuit resistance R_i and capacitance C_i corresponding to an electric double layer capacitance and a leakage current, respectively which cannot be ignored.

Impedance Spectra may be plotted in two ways, the Nyquist representation, where the negative imaginary part of the impedance, Z'' is plotted vs. the real part of the impedance Z' (also called Cole-Cole plot). Or on the other hand, using the Bode representation where the absolute impedance $|Z|$, as well as the phase shift ϕ is plotted vs. the angular frequency ω. Both representations however, contain essentially the same information and can be transformed into one another. One or the other may be preferred due to specific details which may be resolved more precisely (Bierberle, 2000), both are however considered in analysis. However, the Cole-Cole , or rather Nyquist representation shall be used for the analysis of all data.

The polarisation resistance parameter which is the purely Ohmic part of the electrode resistance can be determined from both plots. Similarly, the electrolyte resistance caused by the contribution of the electrolyte can also be determined from the high frequency part of the Nyquist plot at the intersection of the impedance data with the real axis. The relaxation frequency ω_0 is defined as the frequency at the maximum imaginary impedance value (Bierberle, 2000). Where there are several

498600

relaxation processes taking place, there exists several relaxation frequencies which may be identified as the local maxima in the Nyquist plot. The relaxation frequency can be determined from the equivalent circuit elements and gives information about the time constants of single processes. The relaxation frequency of RC unit is defined:

$$\omega_{\circ} = \frac{1}{RC} \tag{32}$$

Whereas for constant phase element (CPE), the relaxation frequency is :

$$\omega_{CPE} = \sqrt[n]{\frac{1}{RQ}} \tag{33}$$

In the interpretation of IS results, it is often found necessary to invoke the concept of *constant phase element* (CPE). This is used as equivalent circuit element, instead of the conventional capacitance, where conventional capacitive impedance is defined as:

$$Z_C = \frac{1}{j\omega C} \tag{34}$$

Here, j is an imaginary unit, ω the frequency and C the capacitance.

2.5.2 Frequency Dependence of Conductivity

At low frequencies, the long range displacements of carriers give the frequency independent (dc) conduction σ_o. As the frequency increases the conductivity gradually increases and over a frequency range from mHz to GHz it is well approximated by, according to Jonscher and Almond:

$$\sigma(\omega)= \sigma_o \left[1 + \left(\omega/\omega_c\right)^s\right] \tag{35}$$

where, ω_c is the frequency of the onset of ac conduction and s is a variable parameter. This equation treats the ac and dc as independent phenomena. However, both contributions should supposedly, arise from the same microscopic mechanism. Vijayakumar and Selvasekarapandian (2004) for example, in their dc and ac *impedance study of mixed conduction in lithium* Vanadate, $Li_xV_2O_5$(x=0.4-1.4), provided another form of the Jonscher's power law to describe the ac behavior as:

$$\sigma(\omega) = \sigma(o) + A\omega^{\alpha} \tag{36}$$

The conductivity spectra of all the samples studied were expected to fit the law. $\sigma(o)$ is the dc conductivity, A is a temperature-dependent parameter and α has been found to take values between 0 and 1.This law is a universal property of the materials and is related to the dynamics of hopping conduction. The parameter α can be expressed as:

$$\alpha = \left(\frac{b_r}{s_r}\right) \tag{37}$$

where b_r and s_r are the back hop rate and the site relaxation rate respectively.

It should be noted however, that in certain compounds the above expressions are inadequate for the description of the conductivity model and additional power terms have to be added, particularly in the *GHz* region and above. The hypothesis is that the ac conductivity behavior would fit these forms of the power law, hence we shall not discuss the others. According to Raistrick *et al* (2005), making use of Jonscher's empirical expressions, gave an expression of the ac conductivity as :

$$\sigma(\omega) = K\omega_p \ + K(\omega_p)^{1-n}\omega^n \qquad (38)$$

where ω_p is the hopping frequency and K depends on the concentration of the mobile charge carriers. According to this model, the high-temperature limiting value for ω_p should be equal to the attempt frequency of ion motion. Once ω_p is known, then the carrier concentration and activation entropy can also be deduced. In a number of materials, however, the low-frequency region is not independent of frequency and a second CPE term must be included.

Jonscher assumed the origin of the frequency dependence of the conductivity to be due to relaxation of the ionic atmosphere after the movement of the particle. This idea, and the earlier concepts, have been developed into a quantitative model suitable for solids by Funke. According to the model, immediately after an ion hops to a new site (a new minimum in lattice potential energy), it is still displaced from the true minimum in potential energy, which includes a contribution from other mobile defects. At long time periods, the defect cloud relaxes, until the true minimum coincides with the lattice site. The model predicts upper and lower frequency-limiting conductivities and a region in between of power law (CPE) behaviour.

2.5.3 Impedance Spectroscopy using the GHz Technique

The above discussion were based on the traditional techiques for measuring impedance in the MHz range of frequencies and lower. However, for the GHz technique an entrirely new approach has to be adopted and has been desribed in detail by Karasik and Mcgrath (1997) and Kezionis *et al* (2010), the foregoing is the summary of the essentail details. High-frequency impedance spectrometry is used to investigate solid electrolytes and distinguishes itself by two important features: first, one can directly measure specific conductivity of solid electrolytes, excluding blocking effects of the junction between sample and electrode, second, one can estimate the intra-grain and grain-boundary impedances of highly conductive ceramics. The majority of the published methods (Kezionis *et al*, 2010) for investigating of electrical properties of solid materials using radio frequency band at high temperatures used the so-called open-ended coaxial probe. It requires a large-size specimen and large high-temperature zone, which consequently causes a large and hardly controllable elongation of coaxial line in high-temperature zone,leading to large phase measurement errors. Sample holding coaxial waveguide is made of the platinum covered refractory ceramics, which distinguishes itself by low thermal expansion; this enables accurate impedance measurement at high temperatures.

Coaxial line are used for the measurements of the impedance in the frequency range 300 kHz - 3 GHz (radiofrequency range). The central conductor of the line is devided into two parts and a sample can be inserted in between, figure 2.9.7(a). s-parameters of the line are measured by Agilent Network Analyser E5062A. The coaxial line (waveguide) can be analysed as three T-matrixes corresponding to 3 cascaded two-port networks. T_x is a matrix describing the sample,

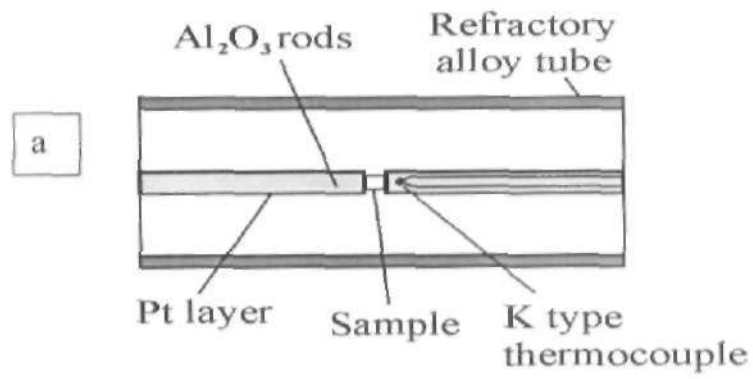
for an equivalent circuit in figure 2.9.7(b) (where Z=x) it is |1-x x| (it is also written in the figure). Tleft is a matrix of the coaxial line on left from the sample and T right – from the right. a_1, a_2, b_1, and b_2 are incident and reflected waves. Once the set of equations are solved and after transformation from T- parameters to s- parameters are done it can be shown that

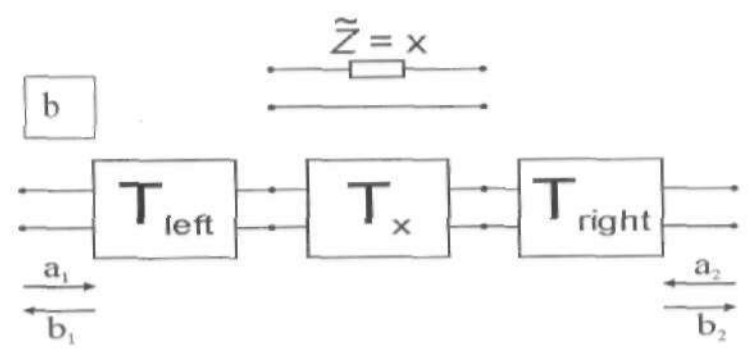
$$X = \frac{{}^{1}/_{S21} - {}^{1}/_{S_{21short}}}{A} \tag{39}$$

where $S_{21} = {}^{b_2}/_{a_1}$ the transmission coefficient of the coaxial line with the inserted sample, $S_{21short}$ is a transmission coefficient of the line when the central conductor is short circuted and constant

$$A = \frac{{}^{1}/_{S_{21}} - {}^{1}/_{S_{21short}}}{X_{cal}} \tag{40}$$

where S_{21cal} stands for transmittion coefficient of the coaxial line with the inserted sample of known capacitance and resistance and x_{cal} is impedance of the known callibration sample.





$$\begin{vmatrix} a_1 \\ b_1 \end{vmatrix} = \begin{vmatrix} T_{11l} & T_{12l} \\ T_{21l} & T_{22l} \end{vmatrix} \begin{vmatrix} 1-x & x \\ -x & 1+x \end{vmatrix} \begin{vmatrix} T_{11r} & T_{12r} \\ T_{21r} & T_{22r} \end{vmatrix} \begin{vmatrix} a_2 \\ b_2 \end{vmatrix}$$

Figure 2.9.7: Central conductor and the coaxial line as sample holder (a) and the coaxial line represented as three T-matrixes corresponding to 3 cascaded two-port networks (b). T_x is a matrix describing the sample, for an equivalent circuit.

This arrangment therefoe measures intrinsic complex impedance (small letter z) defined as:

$$z^* = 1/\sigma^* \qquad (41)$$

Where the σ^{**} means complex conductivity.

Hence the real part of intrinsic complex impedance is defined as

$$z' = \frac{\sigma'}{\sigma'^2 + \sigma''^2} \tag{42}$$

and σ' and σ'' are the real and imaginary components of conductivity respectivley.The imaginary part of the intrinsic complex impedance is therefore defined as :

$$z'' = \frac{\sigma''}{\sigma'^2 + \sigma''^2} \tag{43}$$

Where the actual impedance (capital letter), Z=z*l/S and has the same uinit as rho (ρ), resistivity. The measurement technique is based on measurement of S-parameters of the coaxial line with the sample.

Based on the S-paramters therefor the the real and imaginary components of impedance Z can be calculated from:

$$Z' = {}^{l}/_{\sigma' * S} \tag{44}$$

$$Z'' = {}^{l}/_{\sigma'' * S} \tag{45}$$

Where l is the sample lenght and S is the electrode area and σ', σ'' are the real and imaginary components of the impedance.

CHAPTER THREE

MATERIALS AND METHODS

3.1 Sample Preparation and Synthesis

The preparation of the samples was carried out at the Centre for Energy Research and Development (CERD), O.A.U. Ile-Ife. Basic materials of analytical grade (> 99%) used were $Na_2CO_3.H_2O$, ZrO_2, Li_2CO_3 and $NH_4H_2PO_4$.This was to ensure that the materials were of high purity and of known impurity concentration. Stoichiometric amounts of these materials were mixed and thoroughly ground in an agate mortar for about five hours in each case. The samples were then dried in air for about four (4) hours. Acetone was added in appropriate quantity to homogenize the mixture. Pellets of discs of 13mm diameter and 6mm thickness were prepared for sintering purposes under pressure of 7.42 x $10^5 N/m^2$. The sintering was carried out at the National Metallurgical Development Centre (NMDC), Jos. All the samples were placed inside a gas-heated furnace for eight hours at successive temperatures 573, 773, 1323,1373,1423K,1473 and 1523K, respectively. Between each temperature, the samples were allowed to furnace-cool to room temperature and the samples were thoroughly ground, re-mixed, pelletized and placed back into the furnace for the next round of heating. The first two temperatures were to allow for the volatilization of by-products, ammonia, water and carbon dioxide. The other temperatures were for sintering to allow for the systematic study of the formation temperature of the NZP and provide for regrinding to improve homogeneity, since a uniform heat treatment time of only 8hours was used. The maximum sintering temperature was 1523K. Table 3.1 is a summary of the stoichiometric compositions used in the preparation of the samples.

Table 3.1: Mass Equivalents in grams of starting materials used for the preparation of samples of $Na_{1-x}Li_xZr_2(PO_4)_3$.

	Samples			
Materials	x=00	x=0.25	x=0.50	x=0.75
$Na_2CO_3 H_2O$	62.00	46.50	31.00	15.50
ZrO_2	246.44	246.44	246.44	246.44
Li_2CO_3	-	15.50	31.00	46.50
$NH_4H_2PO_4$	345.09	345.09	345.09	345.09

Preliminary tests were carried on the pelletized samples before the beginning of the experiments, in order to test the behaviour of the samples and sample holders under high temperatures. This was to enable an understanding of their thermal properties particularly, between room temperature and 773K. Different refractory materials (as listed below) were tested to determine their thermal stability and to make sure they would not react with the materials nor cause them to stick. This aspect of the work was carried out at the National Metallurgical Development Centre (NMDC), Jos. The tested materials included: Porcelain crucibles, Fireclay bricks, Silica bricks, ZrO_2 and Nickel. Platinum crucibles are the ideal under these circumstances, however due their unavailability these tests had to take place to obtain alternative materials. The samples showed good air stability. The temperature controller was a pyrometer (model SAVTI) with maximum temperature of 1673K. However, the maximum sintering temperature used was 1523K.

Lithium carbonate (Li_2CO_3) is a colourless salt, molar mass 73.89g/mol, density 2.11g/cm^3, melting point 723°C and boiling point (decomposition temperature) 1583K. Sodium carbonate (Na_2CO_3) occurs in crystalline forms which effloresces to form white powder, the monohydrate. It has a molecular mass of 105.99g/mol, a white solid with density 2.50g/cm^3, its melting point is 1124K and decomposes. Ammonium dihydrogen phosphate, $NH_4H_2PO_4$, molar mass 115.03g/mol; the melting point is 463K with density of 1.80g/cm^3 at 291K. It is colourless , odourless crystalline–white powder granules (Wikipedia, 2009).

Specimens of the virgin powder samples were used for the measurement on DTA machine NETZCHDTA404PC in air, at the Centre for Energy Research and Development (CERD), O.A.U. Ile Ife. The readings were conducted between room temperature and 1273K at heating rate of 20.0K/min. The results are shown in Figures 4.1-4.4. The TGA was performed on virgin powder specimens from room temperature to about 1273K on an TGA Pyris 6 (Perkin Elmer, USA) thermal analyser in air at a heating rate of 20.0K/min at the Mechanical Enginering department, University of Witwatersrand, South Africa. The procedure has been explained in detail in section 2.2.2. The results are shown in figures 4.5-4.8. Both the DTA and TGA data were automatically acquired from the machines and the data plotted in the case of DTA. However, the temperature (°C) data was reconverted to Kelvin (K) unit in the TGA and replotted using the Microsoft EXCEL Program .

3.2 Structure, Microstructure and Phase Characterization

X-ray diffraction measurements were carried out at the Centre for Energy Ressearch and Development (CERD), O.A.U., Ile-Ife, using a precision mini XRD diffractometer MD-10, Version 2.0.4 by Radicon Ltd (figure 3.1). The 2θ range used was 16-70° and the working power was 25kV using 20 minutes acquisition time and CuKα radiation λ =1.5406Å.The calibration standard was Corundum (crystalline form of aluminium Oxide, Al_2O_3, with traces of iron, titanium and chromium). The samples were thoroughly ground and it was ensured that the grains were uniformly sized and randomly oriented, to ensure that it produced accurate intensities which reflect the compositions and phases in the specimen powders. Four compositions of the sintered powder samples were subjected to XRD measurements. All the analyses of the XRD data were carried out using Microsoft EXCEL Program. These include lattice parameter determination, crystallite size and the calculation of density.

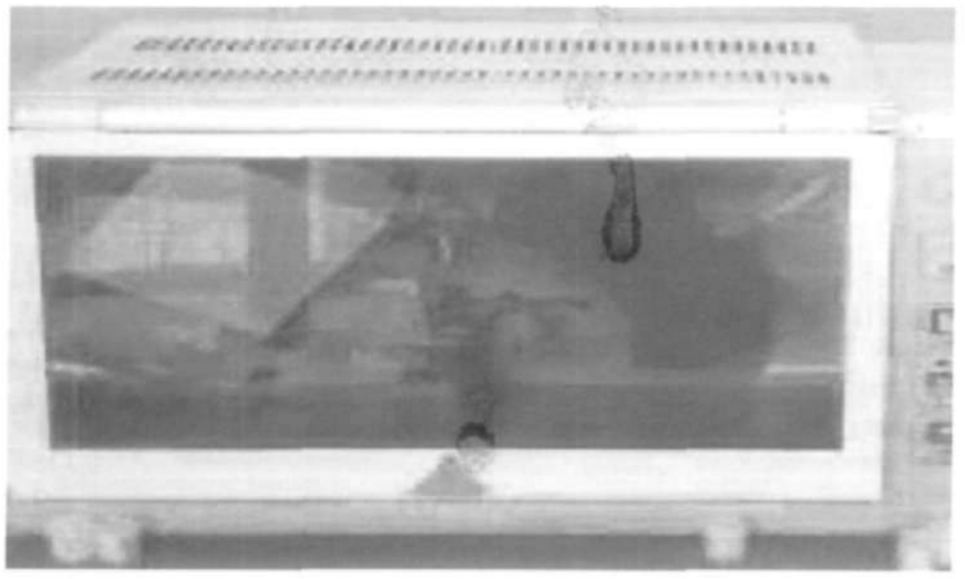


Figure 3.1: The X-ray diffractometer used, version MD-10.

The SEM micrographs were obtained using a small power TMEC scanning electron microscope machine working at 5kV, at different magnifications from 4000

to 20,000, on sintered specimen samples of $Na_{1-x}Li_xZr_2(PO_4)_3$.The working distance was 12800μm and was carried out at the National Institute for Electronic and Computer Technology, Thailand. A miniature thin film sputtering apparatus was used to form thin films of gold layers on all the surfaces of the samples (Rollet and Kalu, 2008) before being finally placed inside the SEM for analysis, since the samples are insulators. This was done to avoid charging of the sample surface during examination in the SEM. The gold layer was made as thin (10-100nm) as possible under the constraint that it be continuous in order to provide a conducting path to ground. It was also ensured that they did not obscure fine details of the specimen.

3.3 *Arrhenius Conductivity and Impedance Spectroscopy*

The Arrhenius conductivity was calculated from the Nyquist plots at different temperatures automatically, using MathLab Program during the impedance measurements, at the Faculty of Physics, Vilnius University, Lithuania. The bulk and total resistance were deduced from the real Z' impedance arcs at different temperatures, using intrinsic impedance. The samples were pelletized (diameter and height as discussed below) and sintered at the maximum temperature of 1523K. A die of 8mm (as this was the size available) was used for the pelletization at 300 MPa. Platimum paste (GVENT Electronic Materials LTD) was applied on both surfaces of the pellets to form electrodes. Measurements were taken from 300-600K. The calculated conductivity values were then fitted to the Arrhenius equation (Eqn. (14)) at different temperatures for the samples 0.0,0.50 and 0.75.

The electrical characterization of the materials was carried out for three samples x =0.00, 0.50 and 0.75 respectively. Different parameters were determined

and plotted: impedance spectroscopy ($Im\,Z''$) Vs ReZ' , frequency dependence of conductivity (σ' Vs f) and σ'' *versus* σ'. The electrical measurements were carried out at the Faculty of Physics, Vilnius University, Lithuania. The samples were pelletized with dimensions as follows: $Na_{0.25}Li_{0.75}Zr_2(PO_4)_3$ electrode surface area 9.08 mm^2, length 1.5 mm. $NaZr_2(PO_4)_3$ electrode surface area 3.46 mm^2, length 1.4 mm. $Na_{0.5}Li_{0.5}Zr_2(PO_4)_3$ electrode surface area 6.16 mm^2, length 1.5 mm. and sintered at the maximum temperature of 1523K. A die of 8mm was used for the pelletization at 300 MPa. The control, acquisition of data and analyses of the electrical properties were carried out automatically using MathLab software, on an Agilent Network Analyser E5062A, in the frequency range 300 kHz to 3 GHz (at 16 points per decade of frequency), and temperature range 300 to 600K. Measurement were performed every 10K, on heating the sample at 1K per min using a voltage of 200mV. The experimental set up is as shown in figure 3.2.

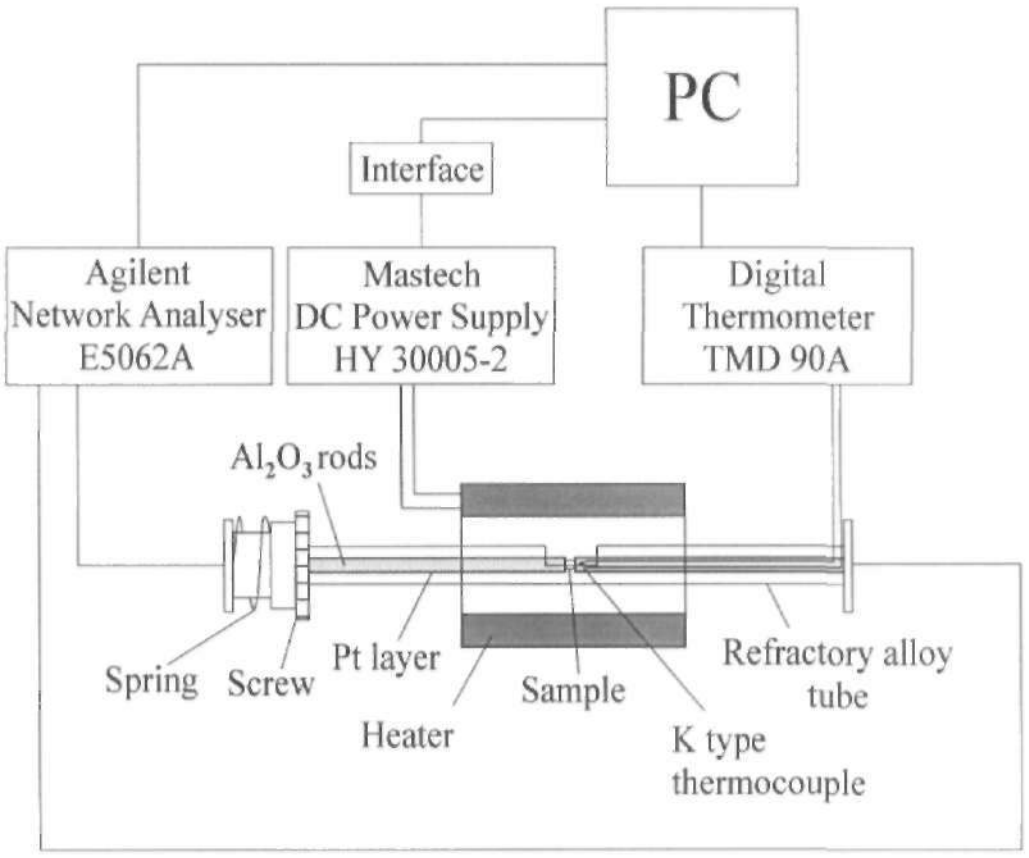


Figure 3.2: Impedance spectrometer set-up operating in the frequency range 300 kHz - 3GHz.

Coaxial line was used for the measurements of the impedance in the frequency range 300kHz to 3GHz. The central conductor of the line is divided into two parts and a sample can be inserted in between, as shown in figure 3.2.

CHAPTER FOUR

RESULTS AND DISCUSSIONS

4.1 Thermal Analyses

The results of the thermal analysis carried out on the samples are presented in figures 4.1-4.8. figure 4.1 is the DTA plot of sample x=0.00. It has only one exothermic peak at 471K, which began from 413-493K in the DTA plot. This can be attributed to the loss of water and water of hydration. Loss of water has been found to be around 573 (Wu, 2005). The heat absorbed increased, until it reached a plateau between 953-933K, indicating synthesis completion. This shows that the sample is stable in this region and is confirmed by the TGA plot in figure 4.2, where the sample showed stability from 873K to 1273K.

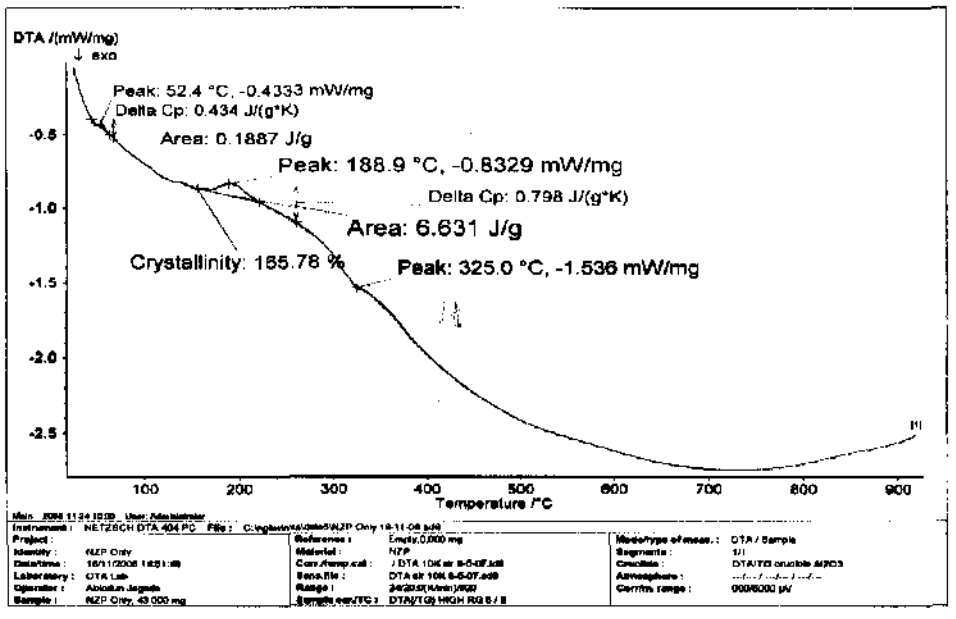


Figure 4.1: DTA plot of powder mixture of sample x=0.00 showing the exothermic peak at 461.9K (188.9°C).

Similar work by Naik *et al* (2004) on the sample has about eight peaks in the DTA plots, three are endothermic and the rest are exothermic. They attributed the endothermic (largest) peak which they found at 393K to the elimination of water from the mixture. Generally mass losses in the range 372-473K have been attributed to loss of water (Simmer *et al*, 1998). Similarly, mass losses occurring at 873-973K have been attributed to loss of ammonia (NH_3) (Kormaneni *et al*, 1986). The work by Pet'kov *et al* (2008) however, did not observe any thermal effects on the samples studied within the same temperature range, though with different precursors. Similarly, the work did not show any special features in its heat capacity. Their work and others showed that using different precursors leads to different effects, particularly, the peaks and their positions.

In the system $Li_{1+x}Ti_{2-x}Al_x$ $(PO_4)_3(0.5<x<0.9)$ the DTA did not show any structural changes on heating, though melting is observed above 1073K (Mouahid *et al*, 2001). Similarly, Oda *et al* (2007) observed the DTA peaks in a temperature region different from the TG in $Li_{1+x}GaTi_{2-x}$ $(PO_4)_3$ with x=0.1-0.9. It has been reported (Bothe and Brown, 2005) in a study of NZP (x=0.00) and by sol-gel preparation, that similar results were obtained, one exothermic peak in the DTA at 543K, in the range 493-553K. Overall mass loss of 29% (room temperature-1273K) is observed, with approximately four temperature regions that show stability from 873K.

The corresponding TGA plot for sample x= 0.00, is depicted in figure 4.2. The mass loss was 7% in the first region, approximately 5% in the second, 15% mass in the third and 2% in the fourth. The mass loss is greatest in the third and is within the region of the exotherm, as observed in the DTA. Overall, there is a mass loss of about

29%, from room temperature to about 1273K. The TGA result indicates that the sample is stable from around 873K, which is in agreement with that of Naik *et al*(2004) and Naik *et al*(2010). Also the general characteristics of the plots is the same, in terms of mass losses in the various regions. This implied the formation reaction of the product is complete at this temperature. This was also found to be in agreement with the DTA results discussed above for the sample. In their study of $Li_{1+x}Ti_{2-x}Al_x(PO_4)_3(0.5<x<0.9)$ (Mouahid *et al*, 2001) did not observe any mass losses in the TGA from room temperature up to 1073K.

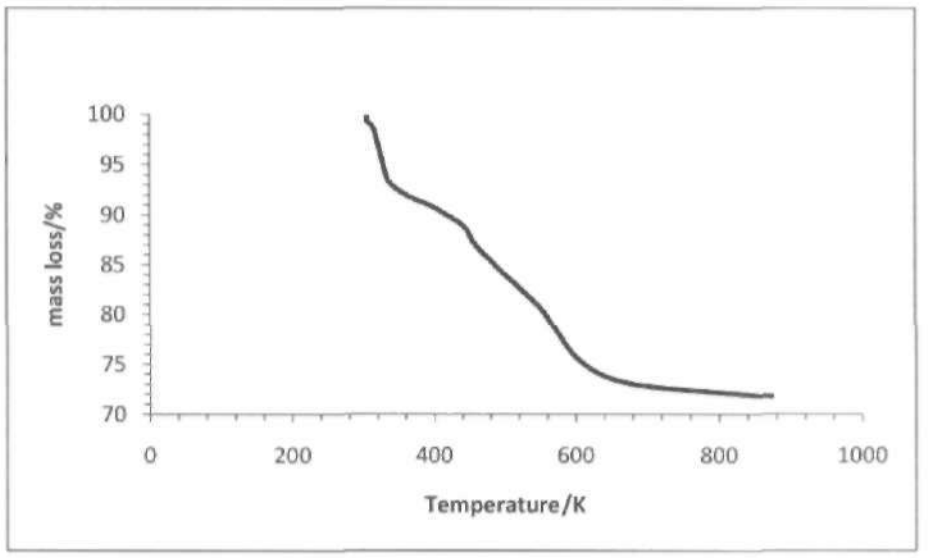


Figure 4.2: TG Plot of of the powder mixture of sample x=0.00 showing the four temperature ranges for mass losses.

In figure 4.3, sample x=0.25 has one sharp exothermic peak at 473K, starting from 453-523K which is also ascribed to the loss of water and water of hydration. A plateau exists from 943-1033K showing that the stability region for this sample began at an earlier temperature. This means that the increment of lithium content in the sample increased the thermal stability of the compound, compared to the x=0.00 sample, depicted in the DTA plot in figure 4.1.

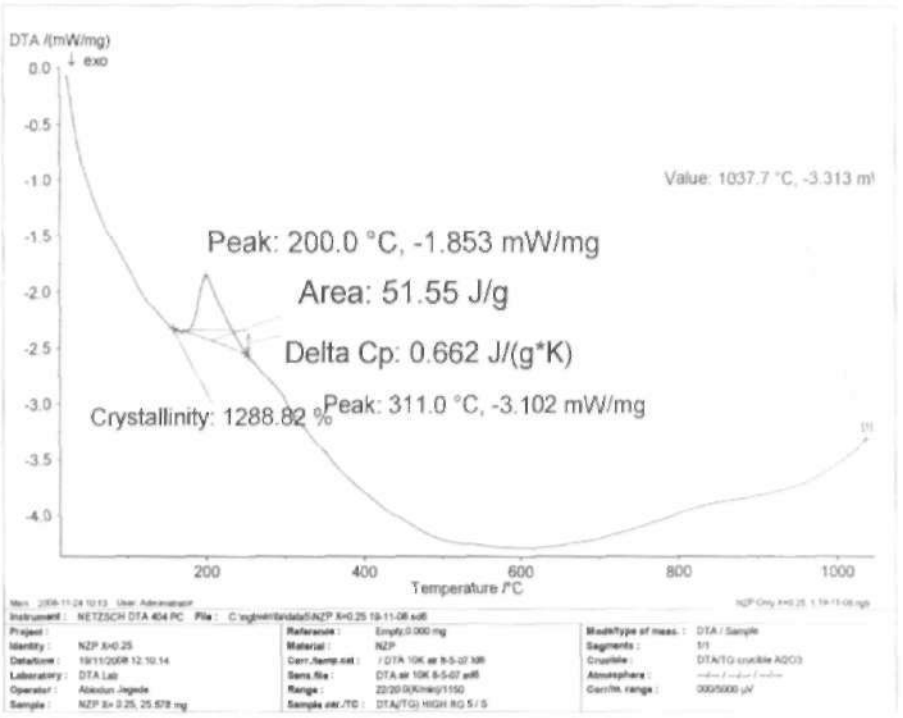


Figure 4.3: DTA plot of powder mixture of sample x=0.25 showing the exothermic peak at 473K(200.0°C).

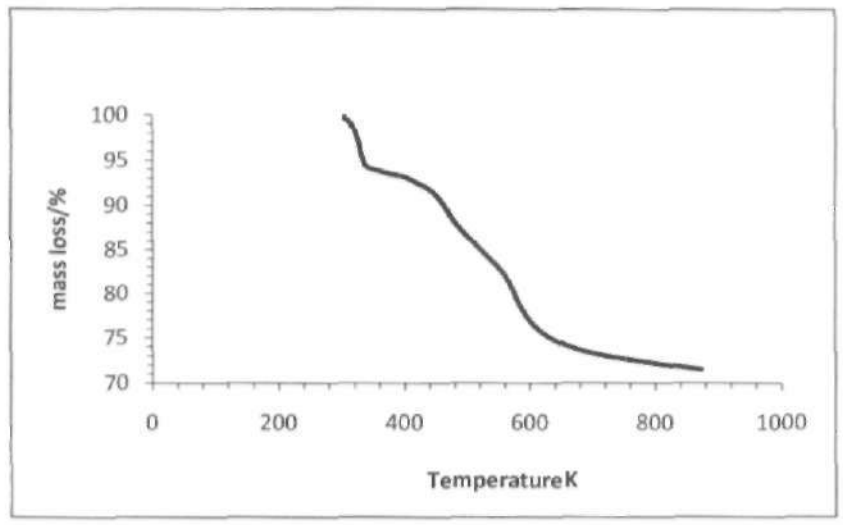


Figure 4.4: TGA Plot of powder mixture of sample x=0.25 showing the four temperature regions of mass losses

Figure 4.4 shows the TG plot of sample x= 0.25. As can be seen, in the same region, the mass losses are 6%, 4%, 16% and 2.5% respectively. Similarly, the mass loss is the greatest in the third region, almost the same amount with the x=0.00 sample. Overall mass loss is approximately 29%, figure 4.4, as in the sample x=0.00 and correlates with the sample x=0.00 in terms of the greatest mass loss in the third region. Similarly, the rate of mass loss with increasing temperature decreased, showing that the material has become more stable with increase in lithium content.

In the case of sample x=0.50, depicted in figure 4.5, there is a sharp exothermic peak at 469K, from 436-523K, which is also attributed to the loss of water of hydration and moisture. A plateau is observed between 853-973K, which is wider than the previous samples. There is a broad exothermic peak at about 973K, which may indicate the start of the crystallization process.

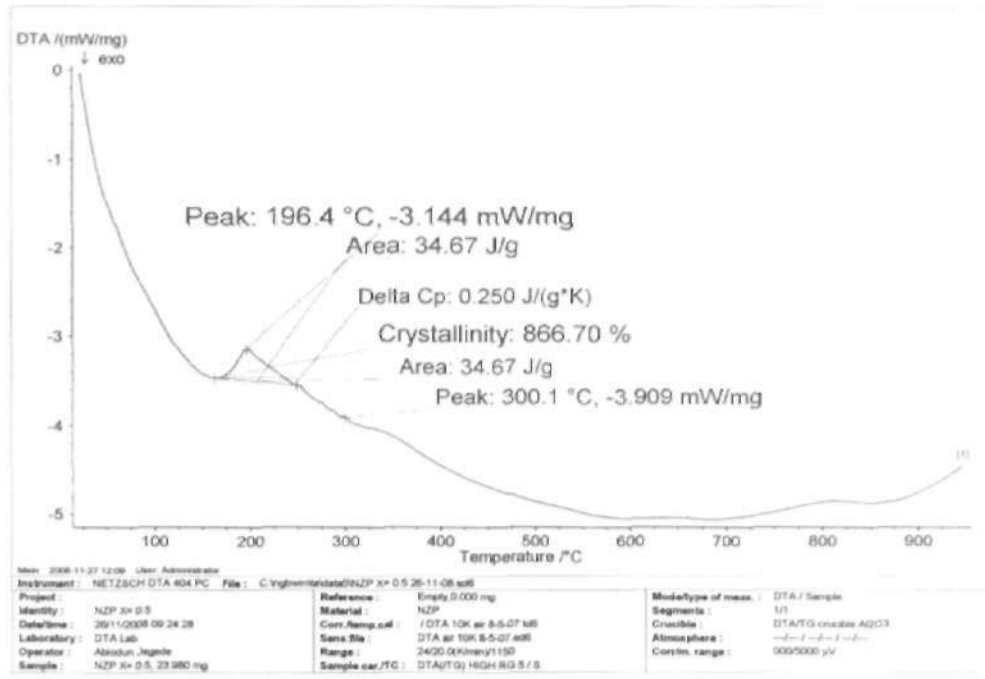


Figure 4.5: DTA plot of powder mixture of sample x=0.50 showing the exothermic peak at 469.4K(196.4°C).

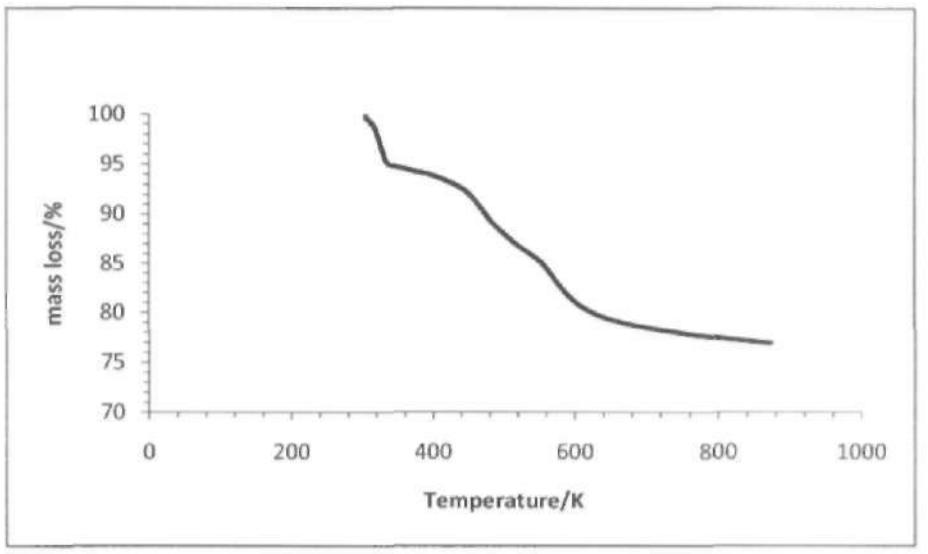


Figure 4.6: TGA Plot of powder mixture of sample x= 0.50 showing the four temperature regions of mass losses.

The corresponding TGA plot for sample x= 0.50, is shown in figure 4.6. The respective mass losses in the regions are 5%, 3%, 13% and 2%, confirming further, the activity in the exothermic region, i.e. , third region. Again there is a slight decrease in the rate of mass loss with changing temperature compared to the earlier samples. Overall mass loss is 23%, further evidence of the comparative stability of this sample.

The last sample, x=0.75, depicted in figure 4.7, has the largest and broadest exothermic peak at 475.6K, between 413-523K, showing the loss of water and water of hydration. Similarly, a plateau at 923-993K is observed which is the widest region of stability compared to the others. This is a confirmation of the fact that increasing lithium content brought about thermal stability of the sample, by decreasing the rate of loss of mass of the sample, as confirmed by the TGA results. Also the positions of the exothermic peaks are shifted towards higher temperatures with increasing lithium content.

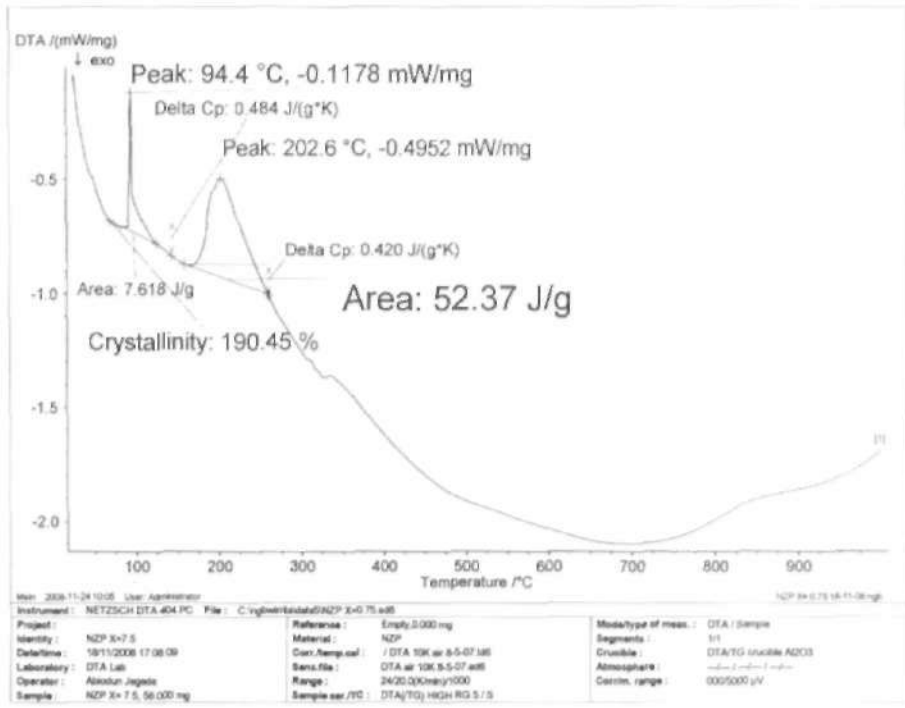


Figure 4.7: DTA plot of powder mixture of sample x=0.75 showing the exothermic peak at 474K (202.6°C)

The position of the peaks shifted with increased lithium content, implying that the lithium increased the thermal stability of the samples, delaying the temperature at which these losses occur. This is confirmed by the TGA plot in figure 4.8.

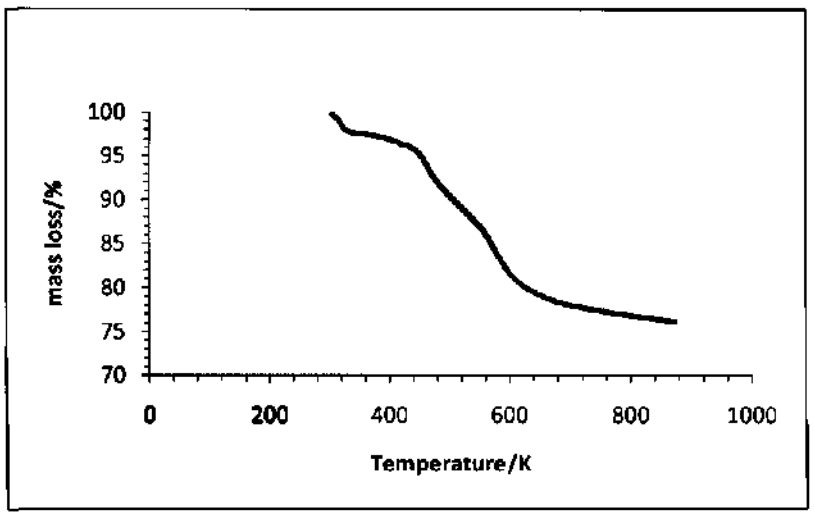


Figure 4.8: TGA Plot for powder mixture of sample x=0.75 showing the four temperature regions of mass losses.

Figure 4.8 represents the TGA plot for sample x= 0.75, with respective mass losses being, 2%, 2.5% and 5% in the regions, and overall mass loss of 25%. The mass loss has drastically reduced in the third region to only 5% and beyond, showing that the lithium content at this level has dramatically increased the stability of the sample with the rate of mass loss with increased temperature being the lowest. The results showed an increased stability of the samples with increased lithium content.

A detailed analysis of the system has been provided by Ahmadu *et al* (2010). The TGA for all the samples have the same character, and can be approximately broken into four temperature ranges: 1) room temperature-333K, 2) 333-453K, 3) 342-633K and 4)

633-1273K. In all the samples 873-1273K was the thermal stability region, as the mass loss is about 1% only. The rate of mass loss decreased with increasing temperature through the regions, until it became virtually constant from 873K upwards in all the samples.

The losses occurred at about the same temperature range, representing the systematic variation in the compositions. Within the temperature range room temperature-333K, x=0.00 showed the highest mass loss of about 30%, with x= 0.75 being the least. Similarly, between room temperature-633K, the plots maintained a particular order in terms of mass loss with x=0.75<0.50<0.25<0.00. The mass losses decreased with increasing lithium content. Beyond this temperature the mass loss for the x=0.00 > x = 0.25 up to about 773K, thereafter they maintained virtually the same mass loss. Whereas the x= 0.50 sample became more stable, with less loss in mass than x= 0.75 and beyond 633K. The x= 0.50 and 0.25 have the same mass loss from room temperature-443K, about 5%. The fourth region has the least mass loss in all the samples and almost the same magnitude. Although the authors (Pet'kov *et al*, 2003a) have studied in detail the compositions $Na_{1-x}Li_xZr_2(PO_4)_3$, x=0.0,0.50,0.8 and 1.00 by TGA/DTA and other characterizations, they did not provide the plots for comparison nor did they provide adequate description of the various effects. The systematic increase in lithium content of the samples leads to the compound formation at lower temperatures. The exothermic peaks are observed to shift towards higher temperatures with increased lithium content just as the process itself shifted towards higher temperatures from its lower temperature limits. Consequently, the thermal stability regions become wider with increased lithium content.

4.2 Phase, Structure and Lattice Constants Determination

The XRD patterns for all the samples are presented in figures 4.9(a)-4.9(d), for samples x = 0.00, 0.25, 0.50 and 0.75 respectively, while figure 4.9.1 shows the patterns plotted on the same scale. All the plots show similar patterns, with the samples mainly in single phase, with presence of minor phase of tetragonal ZrO_2 in some cases. All the samples did not show the presence of any unreacted starting materials, which is an indication that the reaction is complete. The results showed that the samples are polycrystalline with the sample x=0.00, shown in figure 4.9.4(a), having the additional phase of ZrO_2(tetragonal) and a liquid–like (glassy) monoclinic $NaPO_3$. This amorphous glassy phase are seen in the diffuse peaks at high 2θ values, from 55^0 and above.

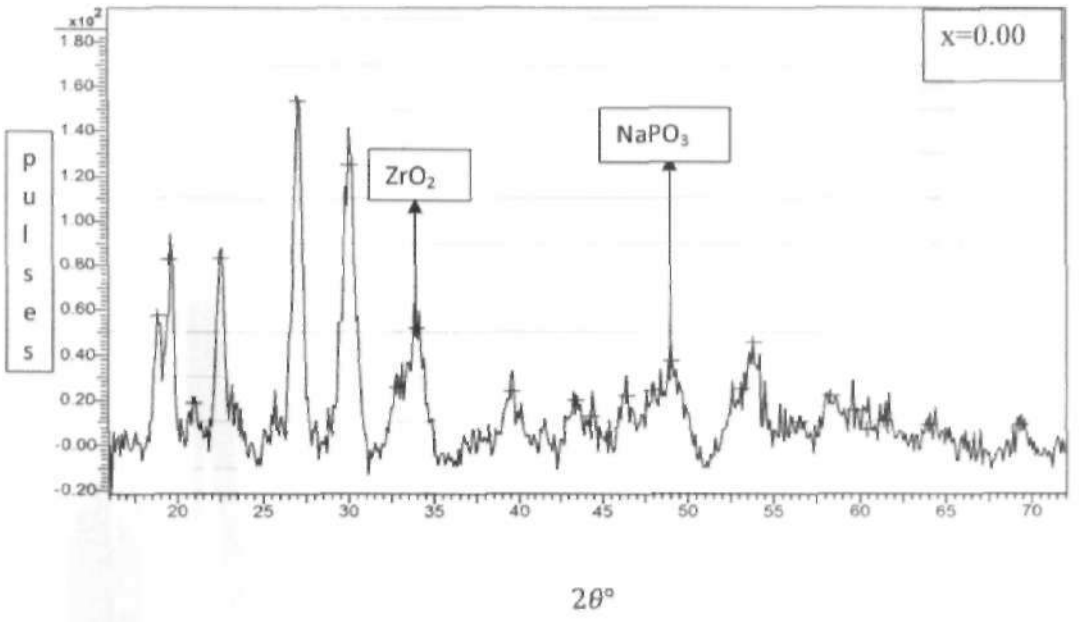


Figure 4.9(a): XRD pattern of sintered sample x =0.00 with ZrO_2 and $NaPO_3$ additional phases.

These are represented by the d-lines at 33.99° and 48.96° respectively as indicated in Appendix A. ZrO_2 is normally precipitated in solid state reactions (Kang and Cho,1999; Fuentes *et al*, 1999; Lee *et al*, 2004a; Nga and Son, 2004) due to the high temperature used resulting in the segregation of Zr^{4+} during volatilization of Na and P at the grain boundaries (Fuentes *et al*, 2004; Lee *et al*,2004a). However, it is not clear whether the ZrO_2 was exclusively segregated after P or Na losses at high temperatures or on the other hand it is inherent to equilibrium (Fuentes *et al*, 2004). At the sintering temperature and time used for the preparation (1250°C at 8h) the ZrO_2 may react with the liquid leading to the formation of zzirconium phosphates (Fuentes *et al*, 2004). The $NaPO_3$ is a glassy material and has also been observed in the synthesis of NASICON (Lee *et al*, 2004a). It has been found to act as flux in the grain boundaries, it enhances sinterability and has the effect of reducing the resistance of polycrystalline materials, thereby improving the connectivity between grains, leading to an increase in conductivity (Lee *et al*, 2004a; Forsyth *et al*, 1998). The patterns generally have their 2θ values similar with slight shifts with the substitution of Na by Li.

Appendix A shows the XRD data for the 2θ values, intensities, calculated d-spacing and their corresponding hkl values. The theoretically calculated (d-cal) and the experimentally observed (d-obs) d-spacings are very close, this indicates that indexing the crystal system in the hexagonal lattice is appropriate. At 2θ=33.99°, 48.96° there is coexistence of ZrO_2 (with relatively intense peak) and $NaPO_3$ phases in addition to the NZP respectively. These are minor impurity phases since there are no other peaks and therefore their effect can be assumed minimal. The intensity of the peaks is seen to increase smoothly with increasing x, with x=0.75 having the highest

intensity. This demonstrates the effect of increasing substitution of Lithium in the unit cell.

The sample x= 0.25,whose pattern is shown in figure 4.9(b), reveals the presence of ZrO_2 and a second phase of NZP, rhombohedral $Na_5Zr(PO_4)_3$ belonging to the R-3c space group, coexisting with the NZP. This is represented by the d-line at 34°, as indicated in Appendix B. It is the only peak and it is therefore expected that the distortion it will introduce to the lattice will be minimal. The compound has been synthesized both by solid state and sol-gel methods and characterized by Pet'kov *et al* (2008).

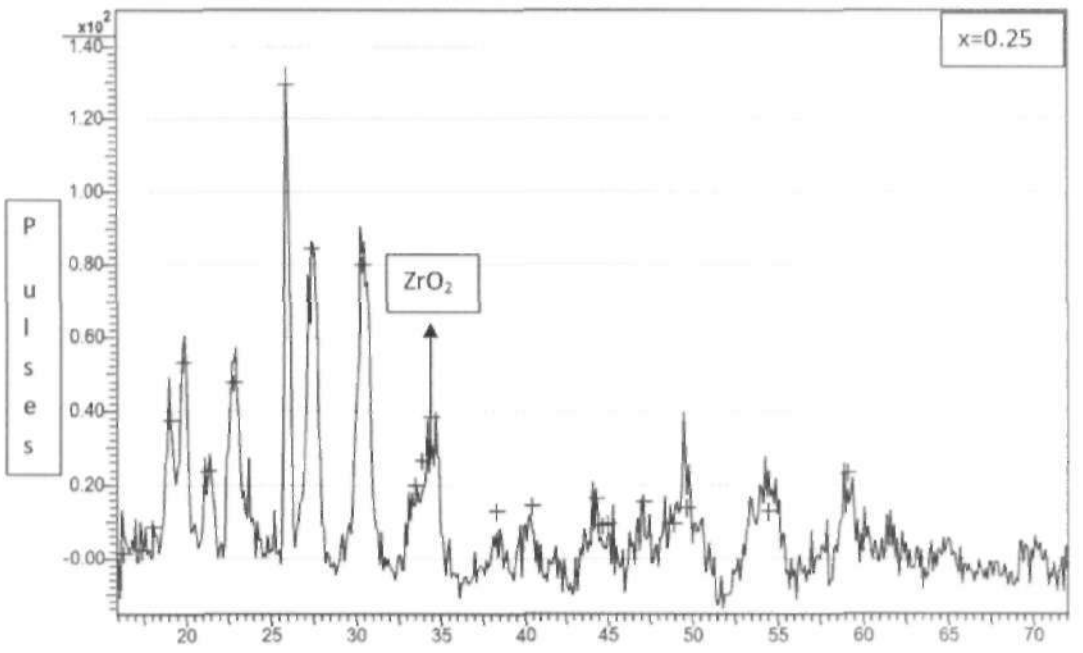


Figure 4.9 (b): XRD pattern of sintered sample x=0.25 with only one phase , ZrO_2.

The pattern for the sample x=0.50 is shown in figure 4.9(c). It also has the phase $Na_5Zr(PO_4)_3$, at 27.12° and no presence of ZrO_2 was detected. This shows that the synthesis in this sample was better. The data is similarly shown in Appendix C with the computed d-spacings, both observed and calculated and their hkl values..

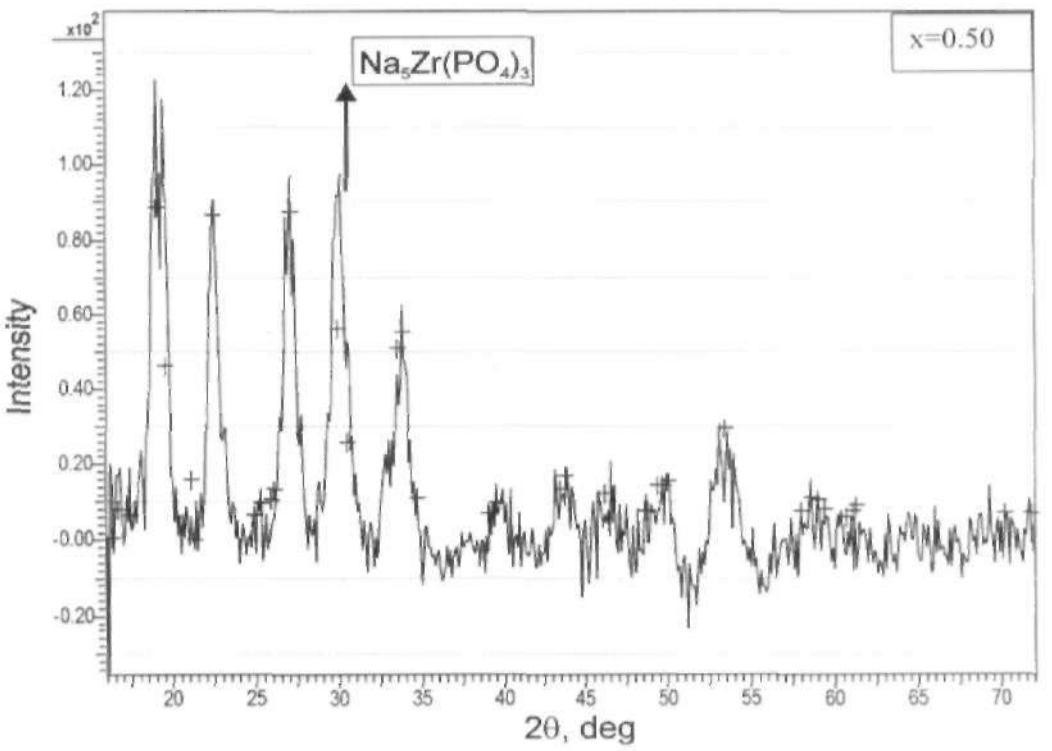


Figure 4.9 (c): XRD pattern of sintered sample x=0.50 with additional phase of $Na_5Zr(PO_4)_3$.

The final sample x=0.75, which is shown in figure 4.9(d), also has only the phase $Na_5Zr(PO_4)_3$ coexisting with the NZP material and has the highest intensity for 2θ values. The calculated d-spacings and those obtained from XRD data, as shown in Appendix D, have similar values and hence is evidence that indexing the system on the hexagonal lattice is appropriate.

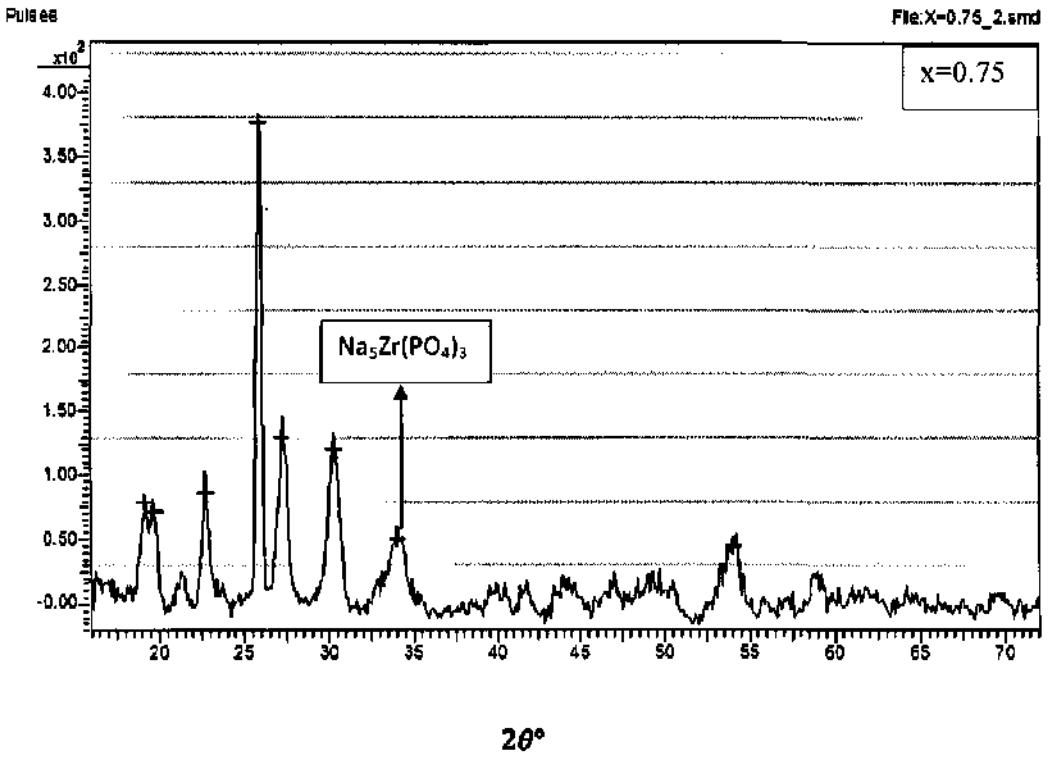


Figure 4.9 (d): XRD pattern of sintered sample x= 0.75 with additional phase of $Na_5Zr(PO_4)_3$

All the samples belonged to the rhombohedral crystal system with the R-3c space group based on a hexagonal unit cell lattice. There was no unreacted starting materials detected showing that the reactions were complete and have no impurity reactants. Impurity phases have been detected in some compositions in the study of $Li_{1+x}Ga_xTi_{2-x}(PO_4)_3$ (x=0.1-0.9). It was demonstrated that these do not affect the electrical properties of the material (Oda *et al*, 2007). Table 4.1 is a summary of the most important results determined from the XRD data: lattice parameters, densities (theoretical and calculated), average crystallite size, calculated from (the Scherer) Eqn. (9), in comparison with published data.

Table 4.1: Summary of X-ray diffraction results for $Na_{1-x}Li_xZr_2(PO_4)_3$ (x =0.00-0.75) and comparative compositions

Sample	Lattice Parameters						
	a, Å	c, Å	V Å^3	d_{x-ray} g/cm^3	d-cal g/cm^3	Average Crystallite size Å	Reference
x =0.00	9.0796±0.0471	22.6960±0.0765	1618.8431	3.02±0.05	1.94(61%)	1.8666	Present Work
	8.803(1)	22.764(1)	1527.8(2)	-	-	-	Kotelnikov *et al* (2001)
	8.8000	22.8600	1534	-	-	-	Petkov *et al* (2003a), **Kotelnikov *et al* (2009)**
	8.8048	22.7572	1527.88	3.20	-	-	ICDD, PDF-2 (33-1312)
x =0.25	8.9661±0.0257	22.4466±0.0824	1563.0683	3.10±0.05	2.16(68%)	15.0687	Present Work
x=0.30	8.7780	23.2580	1552	-	-	-	Petkov *et al* (2003a)
x=0.50	9.1153±0.0558	22.7457±0.1336	1626.61982	2.92±0.03	2.12(67%)	2.3016	Present Work
x=0.50	8.7630	23.4590	1560	-	-	-	Petkov *et al* (2003a)
x =0.75	9.0291±0.0260	22.5647±0.0782	1588.48314	2.98±0.03	-	2.3090	Present Work
x=0.70	8.7420	23.6980	1568	-	-	-	Petkov *et al* (2003a)
x=1.00	8.8077	22.7150	1526.05	3.10	-	-	Salkus *et al* (2006a)

The result of the determination of the lattice parameters, based on indexing on a hexagonal lattice, from the International Crystal Diffraction Database (ICDD) Powder Difraction File [PDF-2(33-1312)] has 80 reflections and shows that the sample x=0.00 belongs to the rhombohedral crystal system with a hexagonal unit cell lattice a=8.8048Å =b and c = 22.7572Å, $\alpha=\beta=90^{o}$ and $\gamma=120^{o}$ and density of 3.198g/cm^3. The result from the present work, Kotelnikov *et al* (2001), Pet'kov *et al* (2003a) and Kotelnikov *et al* (2009) are shown in table 4.1 for comparison.

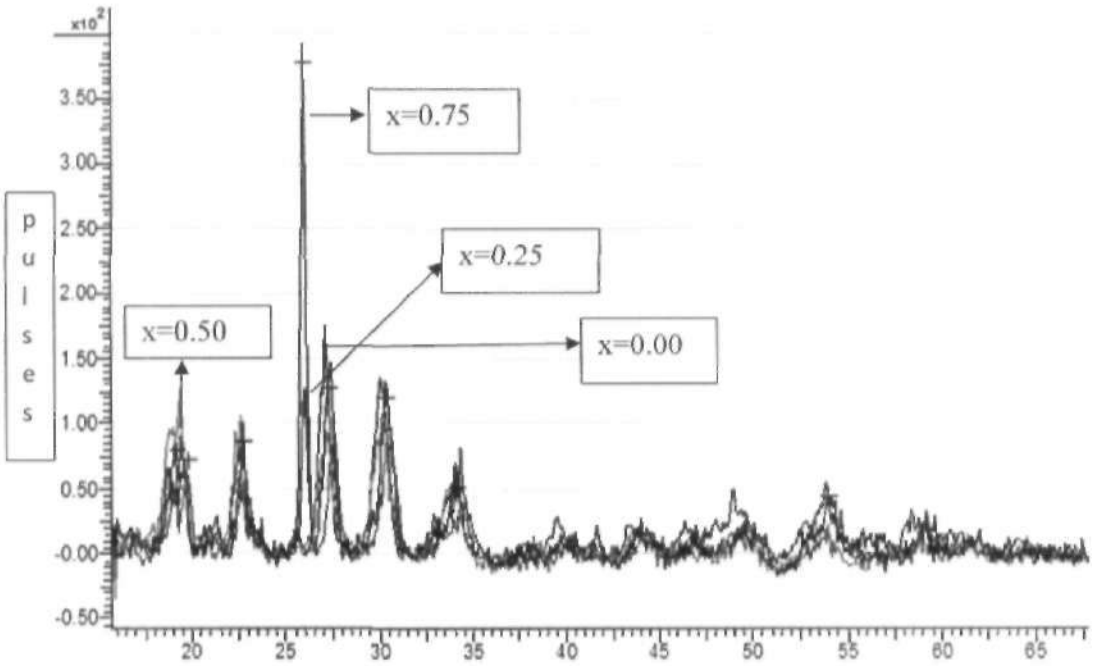


Fig.4.9.1(a): Composite XRD patterns of sintered compositions of $Na_{1-x}Li_xZr_2(PO_4)_3$ on the same scale for x=0.00-0.75.

Figure 4.9.1(a) is the composite plots of the compositions frpom the XRD data on the same scale. It can be seen that the 2θ values of the peaks, for all the samples, fall virtually on the same point, except for slight shifts due to the substitution

of Na by Li and the consequent changes in lattice parameters and unit cell dimensions, which is expected (Forsyth *et al*, 1998; Best *et al*, 1998). Table 4.1 shows that the result from the present work is highest in the a parameter than all the references for sample x=0.00. It is also larger than that of sample of other comparative compositions 0.50 and 0.70, from Pet'kov *et al* (2003a). This could be due to a systematic error resulting from the inability to perform the XRD in step scan mode so that 2θ values at steps of 0.02^{o} or 0.028^{o} (Best *et al*, 1998) for example, could be carried out, thereby causing some of the reflection peaks to be missing, particularly from the lower 2θ values, since these are important in the determination of the a parameter. It has been observed that a shift in 2θ values, towards lower values is as a result of ion difference between dopants with higher ion radius than host (Wu, 2005). This is pristine sample however, such a situation is not expected. However, Mouahid *et al* (2001) have reported a case in which Al, which was intended for substitution at the octahedral sites of NASICON only, was also detected at the tetrahedral sites too, with implications for stoichiometry and unit cell dimensions. This may also be the case. However, further investigation such as NMR and full structural analysis is required to confirm this. It is also noteworthy that the crystallite size for x=0.00 is the smallest, 1.87Å and could have affected the accuracy of the 2θ values obtained.

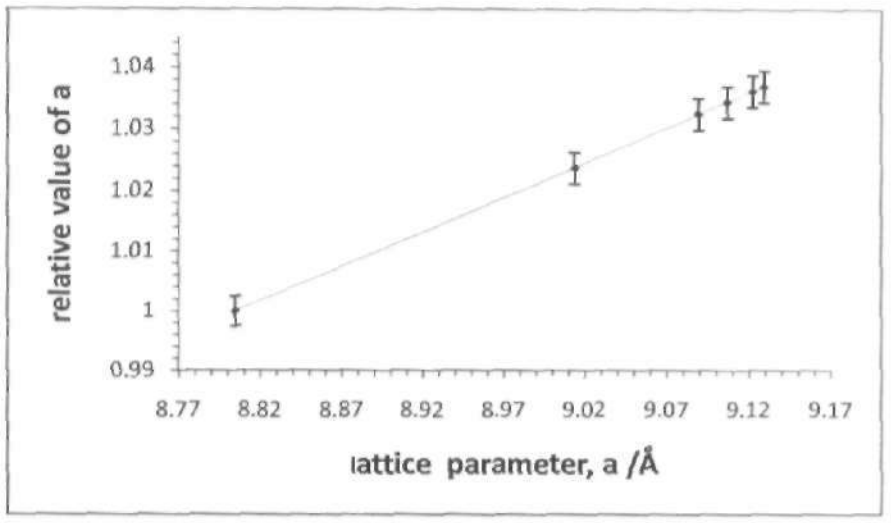


Figure 4.9.1(b): Relative value (with respect to PDF-2:33-1312) of lattice parameter a plotted against the XRD determined lattice parameter and their error bars for sample x=0.00.

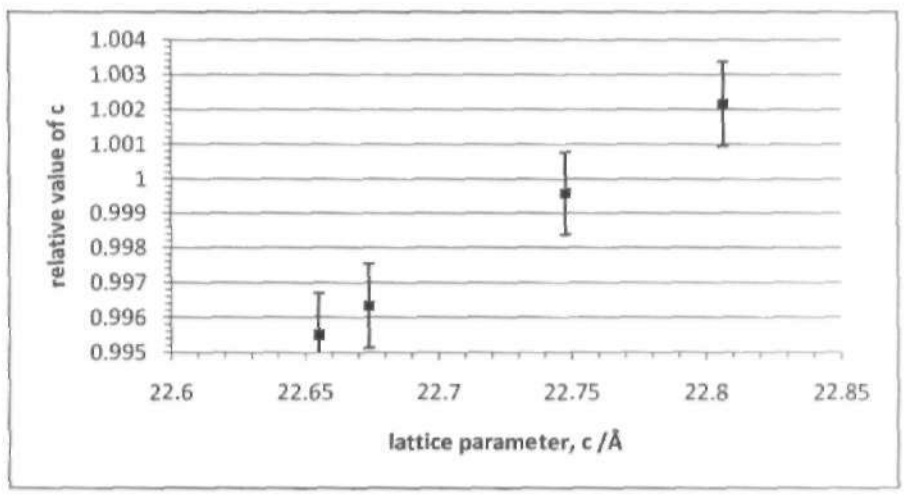


Figure 4.9.1(c): Relative value (with respect to PDF-2:33-1312) of lattice parameter c plotted against the XRD determined lattice parameter and their error bars for sample x=0.00.

The variation of the relative values of the lattice parameters a and c for sample x=0.00, are shown in figures 4.9.1(b)-4.9.1(c) and with their error bars. It can be seen that while the a parameter was systematically higher, the c parameter, on the

other hand, was smaller. It is possible that it is due to the synthesis characteristics, such as microcracking, although the grain size for the sample is less than the critical size for the phenomenon to be observed. Increasing incorporation of Li^+ cation into the appropriate lattice is supposed to decrease the c parameter. However, further incorporation is expected to increase the a parameter, due to the contraction of the structure in the c direction, with its subsequent extension in the a direction. A similar study, which is the reverse of this investigation, (substitution of Potassium, K, of larger radius than Na, Li) has been studied by Pet'kov *et al* (2003a) where potassium was substituted for Na in $NaZr_2(PO_4)_3$. Though specific analysis of the Na occupancy sites was not available, since full structural analysis was not carried out. Their results show that the effect of substitution and the subsequent variation is not smooth in terms of increasing c parameter with increase in K content (Kotelnikov *et al*, 2001; Pet'kov *et al*, 2003a). At a particular composition x, a decrease in a is observed on the contrary, due to the position the K may occupy on the possible occupancy sites. Figure 4.9.1(d) shows that with increase in lithium, the cell volume initially decreased (x=0.25), then at a particular composition x, it increased, with subsequent decrease as x increased to the maximum. The increase in cell volume may be explained in terms of the site occupancy of the Li and Na ions. If both are on the same site, say on the M1 site, there should be an increment in the c axis, with a corresponding decrease in a axis. This could lead to the 'mixed cation effect' with subsequent implication for the electrical conductivity of the sample. This will be discussed further later.

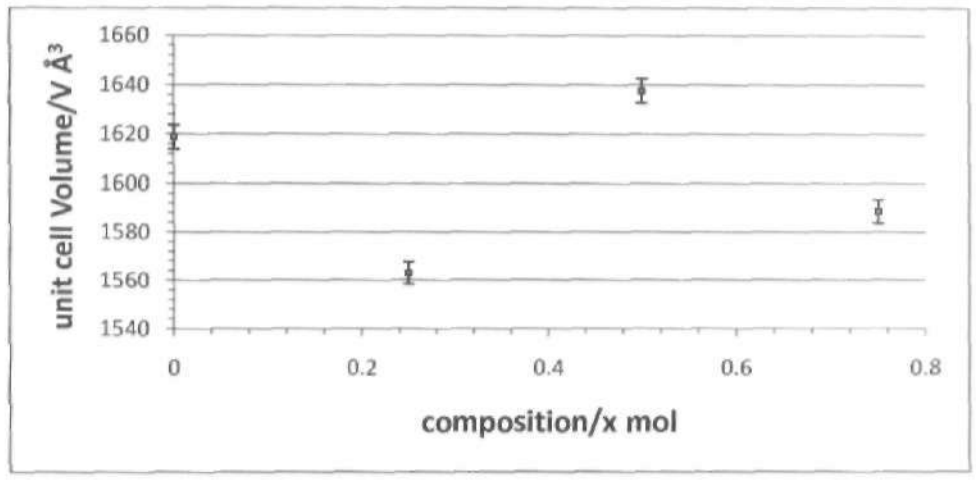


Figure 4.9.1(d): Variation of unit cell volume versus composition and the error bars for sample x=0.00-0.75.

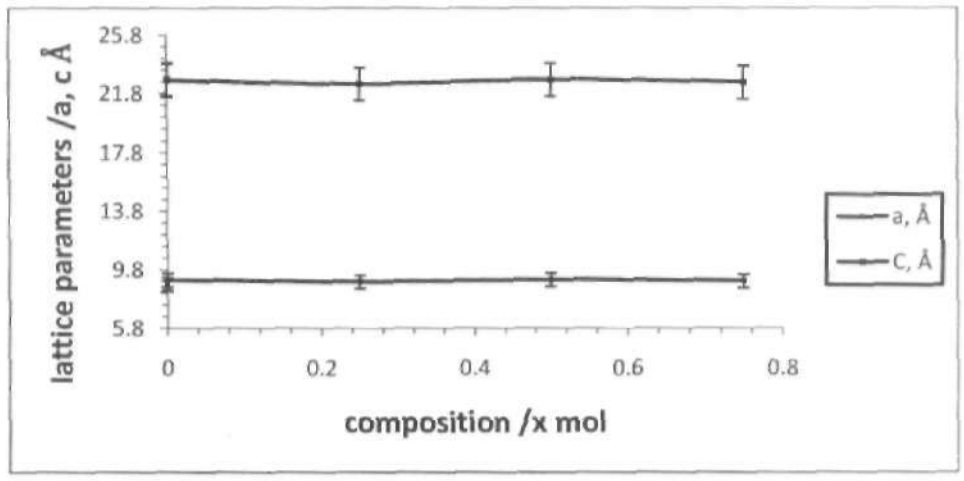


Fig.4.9.1(e): Plots of experimentally determined lattice parameters a (lower) and c (upper) against composition (x) with error bars for samples x=0.00-0.75.

Figure 4.9.1(e) is a plot of the variation of lattice parameters a and c with increase in lithium content for all the compositions. It shows that there is little variation in lattice parameters with increase in lithium content. At about x=0.25 we observe a slight decrease in both a and c parameters. There are very few studies of coupled mobile ion in NASICON systems, and in particular the effect of their substitution on site

occupancies. One such study on Na-Li exchange of $Na_{1+x}Ti_{2-x}Al_x(PO_4)_3(0.6\leq x\leq 0.9)$ NASICON series, shows that partial Li exchanges (substitutions) in the system leads to a decrease in the length of the a axis, whereas the change in the c-axis is negligible, as it is more sensitive to the MI site. Further, the Li is found located in the MII site while the MI site has both Na and Li. However, in the fully exchanged samples, the c axis decreased while the a axis increased (Mouahid *et al*, 2001). In the NASICON system, the MI site is completely filled by Na ions while the MII site is empty. This is also expected of this system, however, with less degree of the changes in the lattice dimensions since the substitution is limited to x=0.75. Detailed structural analysis and NMR for this system is necessary to confirm this hypothesis .

The theoretical density of sample x=0.00 is 3.20g/cm^3 and is very close to that calculated from the XRD data which is 3.02g/cm^3. The result obtained from experimental data by measuring the dimensions of the pellet was however lowest for the x=0.00 sample, i.e. 1.94g/cm^3, with a degree of compaction of 61%. This is probably due to the sintering conditions and microstructure of the materials. Although there did not seem to be porosity as such to explain the low density. However, it may be the result of the low sintering time of 8h used at 1250°C. Figure 4.9.1(f) depicts the variation of the average density of the samples, calculated from the XRD data, against the compositions (x). This must be understood within the context of the variation of the unit cell volume earlier discussed. The initial increment in the density is in accordance with the decrease in the unit cell volume observed for x=0.25. Subsequently, there has been a decrease in density with further lithium incorporation, which is a result of the lower density of lithium compared to Na.

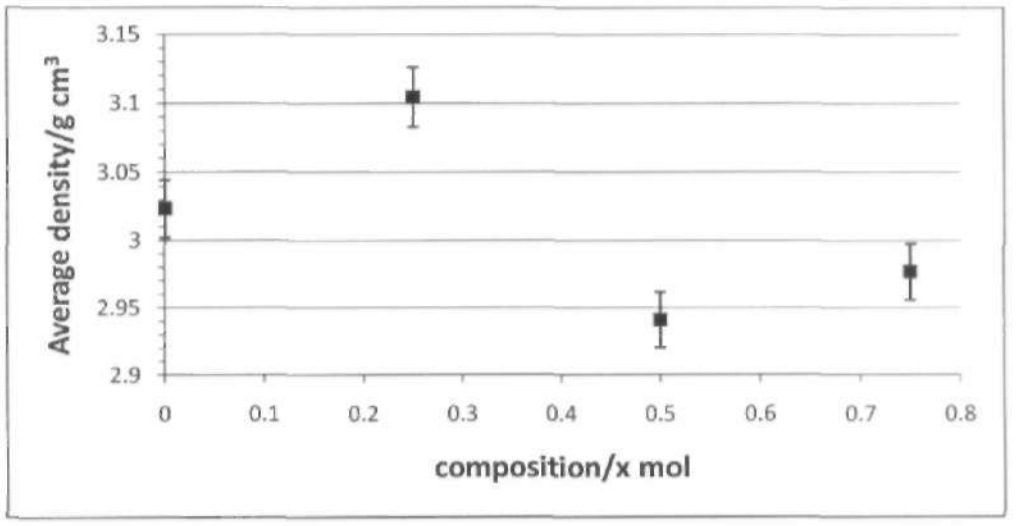


Figure 4.9.1(f): Variation of density with composition and error bars for sample x=0.00-0.75.

The result of the effect of the substitutions of Na by K (larger radius) of selected compositions, on lattice parameters and density, has been provided for comparison in table 4.1 from Pet'kov *et al* (2003a), since no result for lithium substitution in the appropriate composition is available. The densities showed a decrease with increasing incorporation of lithium which should be expected due to the lower density of lithium compared to Na that is being replaced. The value of c parameter however generally decreased with increasing lithium incorporation and this should be expected too as Li has smaller ionic radius than Na. The value should be contrasted with that from the total substitution of Li (x=1.00) in the system given by the lattice parameters from Salkus *et al* (2006a) of $LiZr_2(PO_4)_3$ which is further evidence that the x=0.75 sample's c parameter is appropriate. The volume V of the unit cell should actually decrease with increasing substitution of Li in the system, however it was generally higher because of the consistently high values of the a parameter which made the volume of the cell to increase instead. It should be observed that exact data is available only for the x=0.50 for comparison.

The average crystallite size calculated from the Scherer's formula for the x=0.00 sample is 1.8666Å. The sample x=0.25, with crystallite size of 15.0686Å is the largest and expectedly gave a better result, in terms of the lattice parameters, a=8.9660Å and c =22.4460Å. Similarly, it is expected to have the highest electrical conductivity due to the largeness of its crystallite size.

4.3 Microstructure Determination

The SEM micrographs were obtained using a low power TMEC scanning electron microscope machine, working at 5kV at different magnifications up to 20,000. Micrographs of selected samples are shown in figures 4.9.2(a)-4.9.2(h). It shows samples having different particle sizes with virtually no pores, showing that there was appreciable densification.

The microstructure results for sample x=0.00 are shown in figures 4.9.2(a)-4.9.2(b) at different magnifications, showing liquid-like phases, which were confirmed by XRD to be glassy $NaPO_3$. However, at both the top and right hand corners are seen well crystallized small grains between 1-1.5μm. The bright crystallites are ttetragonal ZrO_2. Many studies have observed the presence of Monoclinic ZrO_2 instead, which may be due to the sintering temperature used. There were also no excessive grain growth observed. The range of the particle sizes were consistent with the value of the crystallite size obtained from XRD for this sample which was the smallest. It has been reported that phase formation at lower temperatures often leads to smaller grain sizes (Simmer *et al*, 1998) and that the particle with lower particle size has the lower crystallite size (Suuol and Escoda, 2007).

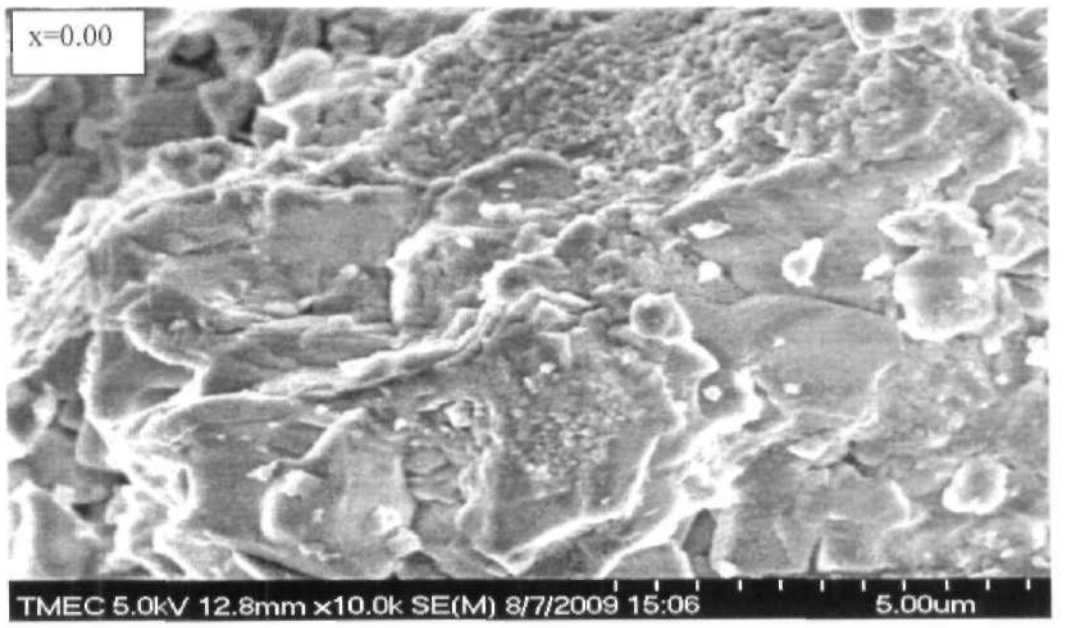


Figure 4.9.2(a): Micrograph of sintered sample x=0.00 with liquid–like phases and well formed crystallites at the top left corner.

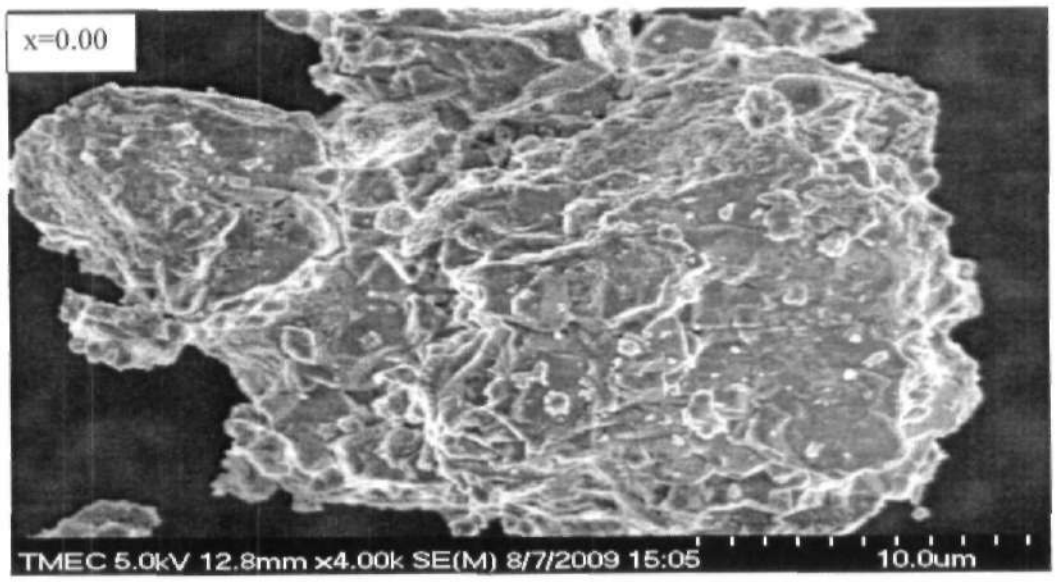


Figure 4.9.2(b): Micrograph of sintered sample x=0.00 at lower magnification with liquid–like phases.

The micrograph for sample x=0.25 is depicted in figures 4.9.2(c)-4.9.2(d) at two magnifications. It shows well crystallized grains of large size with a narrow range of size distribution of about 1-2 μm. It also has very few pores. The bright spots are tetragonal ZrO_2 and $Na_5Zr(PO_4)_3$ detected by XRD. Because the crystallite size was largest, from the XRD results, it is consistent with well formed particles in the SEM.

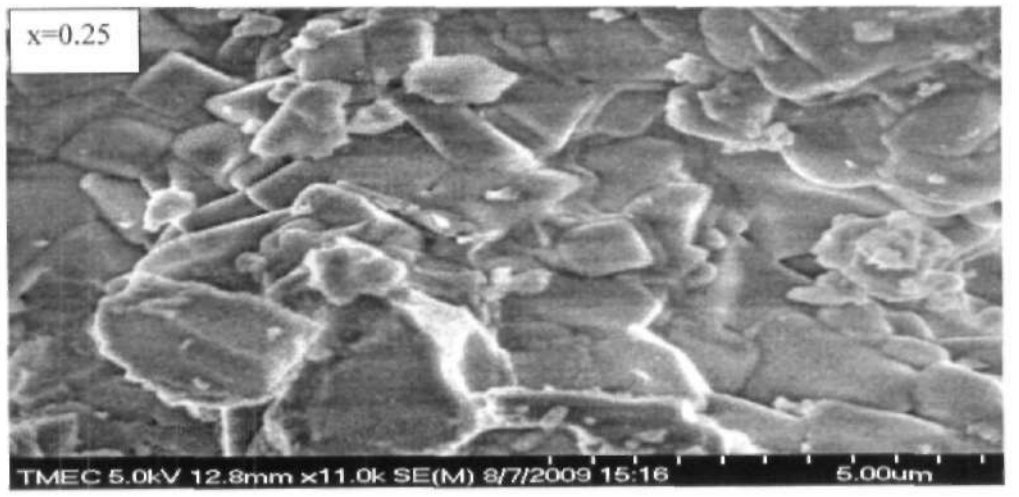


Figure 4.9.2(c): Micrograph of sintered sample x=0.25 at higher magnification showing well formed grains of different sizes and virtually no porosity .

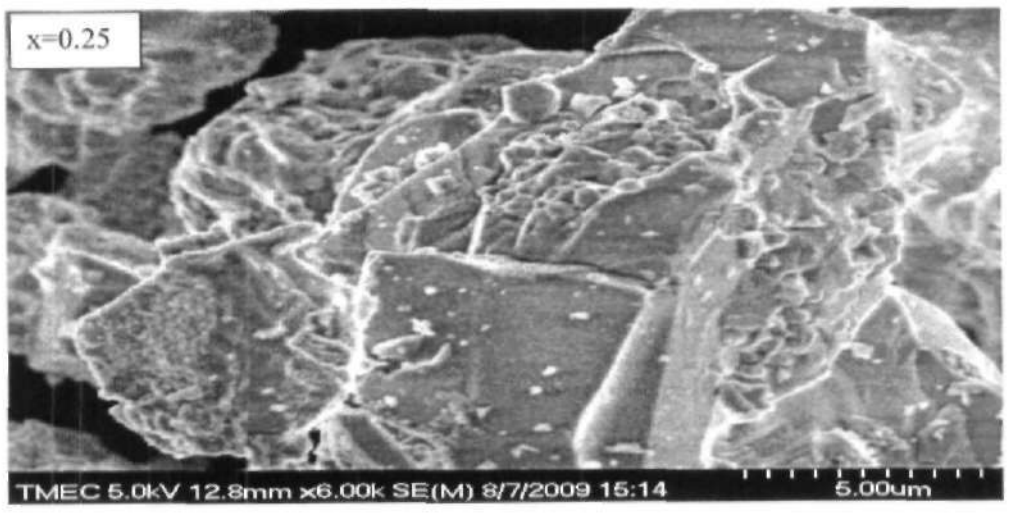


Figure 4.9.2(d): Micrograph of sintered sample x=0.25 at lower magnification showing large grains.

The SEM micrograph for sample x=0.50 is depicted in figures 4.9.2(e)-4.9.2(f). It has larger grain sizes little pores and well crystallized .One can also observe a fairly narrow size distribution, in the 3-7μm range , with no trace of ZrO_2, rather the presence of $Na_5Zr(PO_4)_3$ as indicated from the XRD results.



Figure 4.9.2(e): Micrograph of sintered sample x=0.50 at higher magnification with large grains and fairly uniformly sized and no porosity.

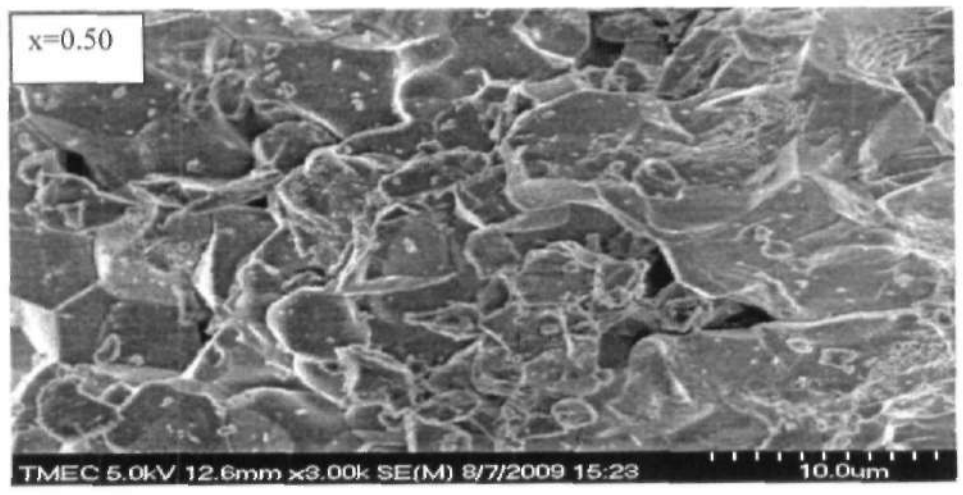


Figure 4.9.2 (f): Micrograph of sintered sample x=0.50 at lower magnification showing distribution of sizes in grains and some porosity.

Similarly, the last sample x=0.75 also showed evidence of good synthesis with a fairly large grain size of 3-6μm, similar to x=0.50, and a wider size distribution. This is in accordance with the similar crystallite sizes, approximately 2.3Å. There was also no evidence of the presence of ZrO_2, however the presence of $Na_5Zr(PO_4)_3$ is in agreement with the XRD data. The sizes of the crystallites seemed to be similar to that of x= 0.50 and there was general increase of the grain sizes with increase of lithium content and this may be related to the synthesis conditions which may have favoured the formation of larger particles due to favourable thermal properties of lithium. Since the conditions for the preparation of the samples were the same, it appeared that lithium substitution favoured grain growth. Such a characteristic has been observed in the study of $Li_{1+x}Ga_xTi_{2-x}(PO_4)_3$ (x=0.1-0.9) (Oda *et al*, 2007) with increasing Ga^{3+} substitution.

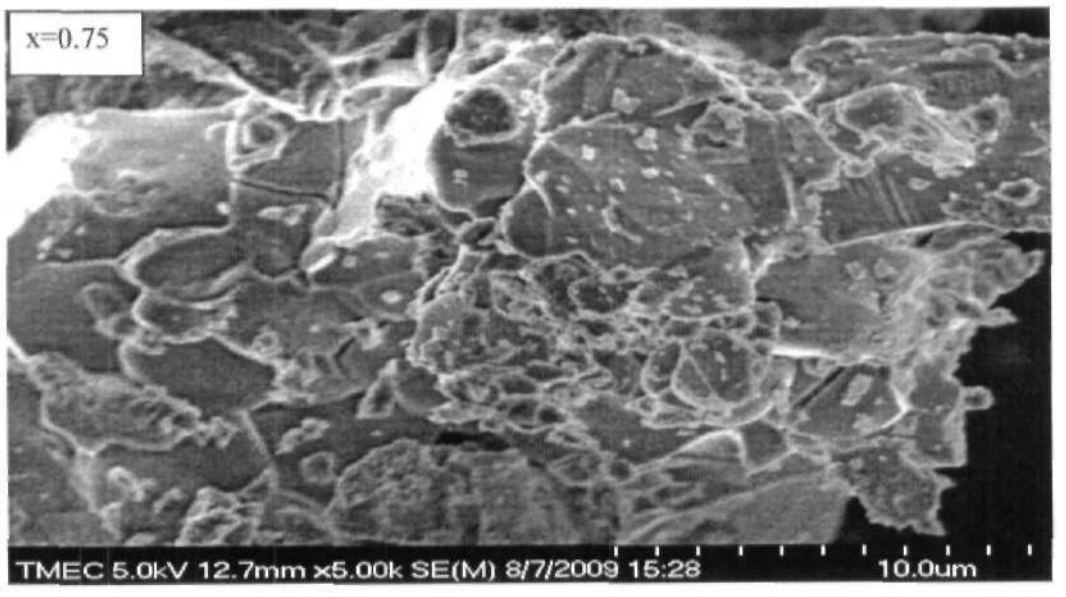


Figure 4.9.2 (g): Micrograph of sintered sample x=0.75 at higher magnification with fairly large grains.

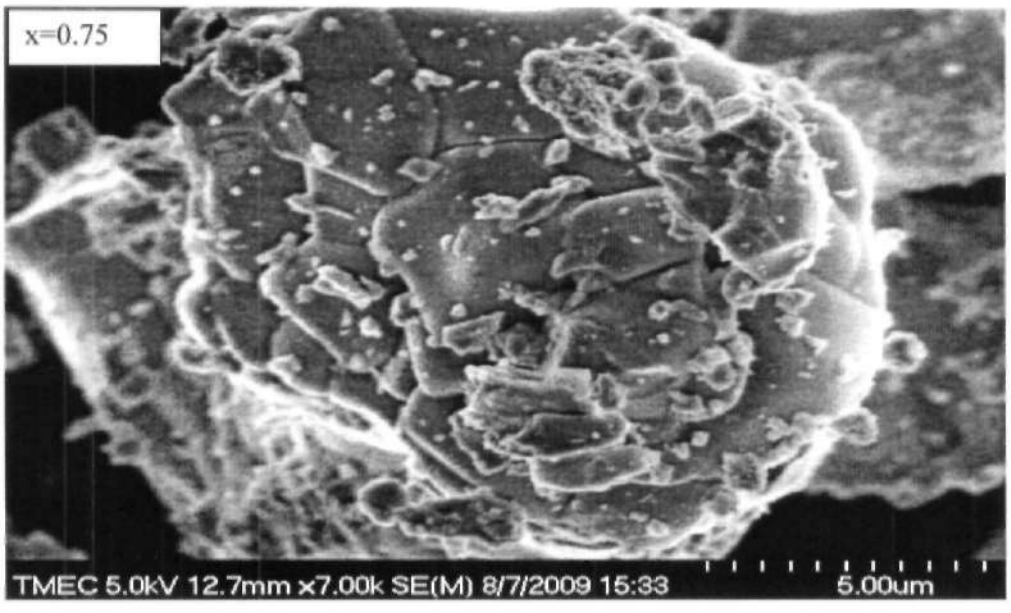


Figure 4.9.2 (h): Micrograph of sintered sample x=0.75 at lower magnification

4.4. Impedance Spectroscopy

The results of the impedance spectroscopy measurement are provided in Nyquist plots of figures 4.9.3(a-c) and 4.9.6(a-c) for the three samples investigated, that is x=0.50,0.75 and 0.00, respectively. In figure 4.9.3(a), two semicircular arcs can be distinguished for sample x=0.50, though not very well formed, rather deformed and overlapping at temperature of 500K. The smaller semicircle can be attributed to processes occurring in the bulk of the materials at high frequencies, whereas the larger semicircle, since it occurs at lower frequency, represents processes occurring in the grain boundary at lower frequencies (Salkus *et al*, 2006a). The fact that the semicircle ended at the origin is attributed to the absence of resistance in series with the two parallel *RC* circuits in series used for the equivalent ciruits and for modelling the behaviour of the ceramics (Anatharamulu *et al*, 2008). The overlapping of the semicircles could be attributed to inhomogeneities (Nga and Son, 2004) in the ceramic, the closeness of the relaxation frequencies (that is time constants) in the bulk and grain boundary processes and the nature of electrodes used (platinum paste was used), which was blocking to the ions (Best *et al*, 1998). The semicircles would be separated if the time constants for the grain boundary $R_{gb}C_{gb}$ is two orders of magnitude larger than for the bulk R_bC_b (Furusawa, 2006). However, electrode effect does not seem to be effective in this composition.

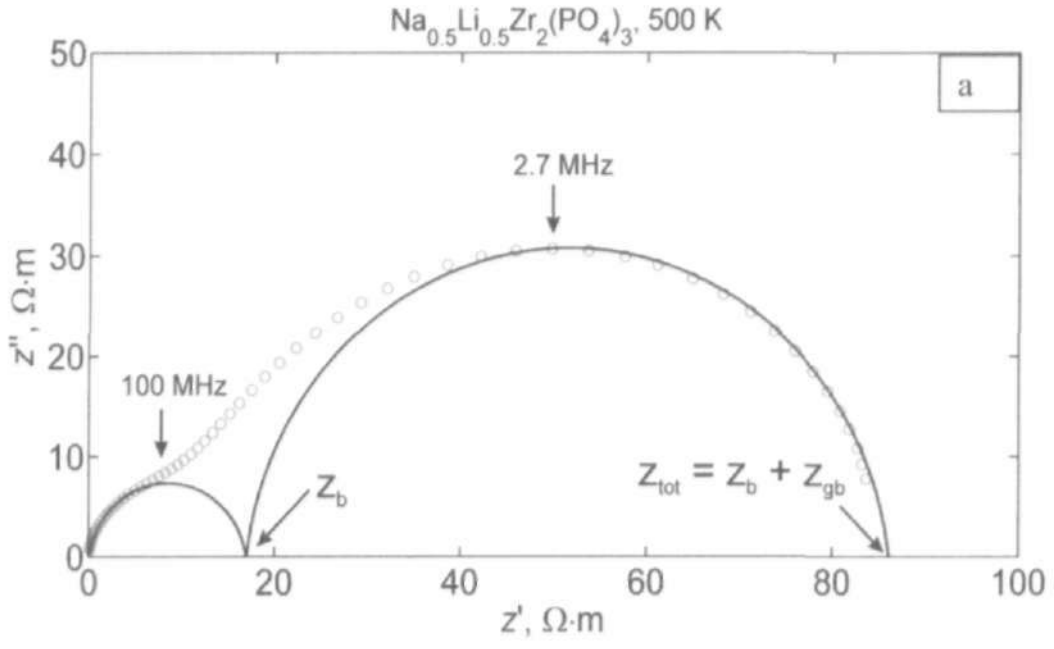


Figure 4.9.3(a): Complex impedance plots at 500K showing the frequencies at the maximum imaginary impedance z'' at 2.7MHz, 100MHz for the grain boundary and bulk repectively.

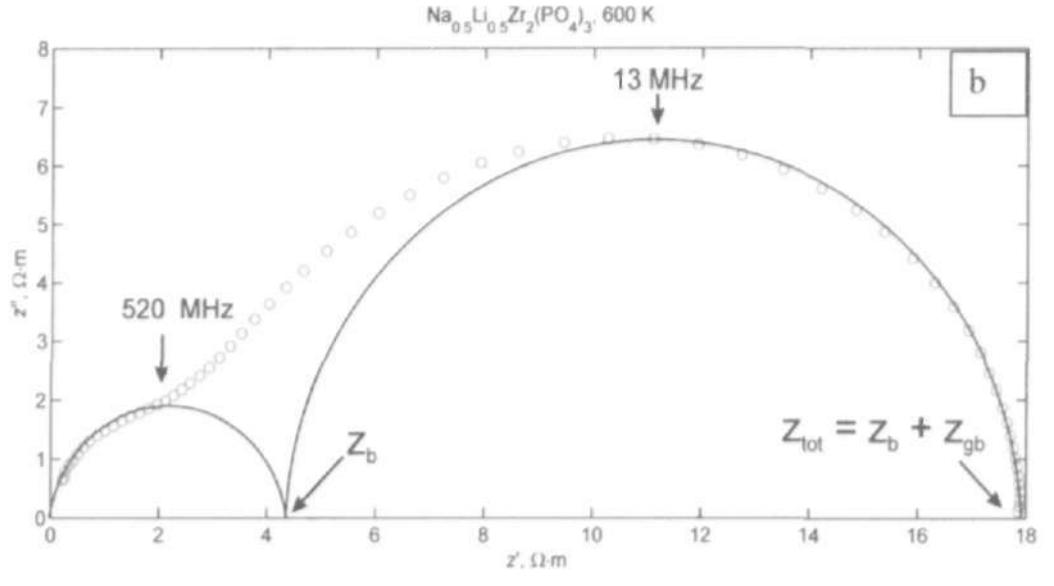


Figure 4.9.3(b): Complex impedance plots at 600K showing the frequencies at the maximum imaginary impedance z'' at 13MHz and 520MHz for the grain boundary and bulk repectively.

Similarly, the centre of the semicircle is a bit off centre, below the axis. This is due to the distribution of relaxation processes occurring in the material (Leftterova *et al,* 2004). The bulk contribution was obtained by extrapolating the high frequency arc of the bulk to cut the real impedance (intrinsic) axis (z'), giving an estimated bulk conductivity of 7.99 x10^{-2}S/m, while the grain boundary conductivity is 6.99 x10^{-5}S/m. The value of the grain boundary conductivity is about 3 orders of magnitude lower, and is in agreement with those obtained for ZrO_2, CeO_2 and $LiTi_2(PO_4)_3$ ionic conductors (Wolfstein, 2008). Further, the low value of the grain boundary conductivity has been attributed to space charge effects, associated with grain boundaries but which are not found in the bulk. The value of the total conductivity was also obtained by extrapolating the low frequency arc to the real intrinsic impedance axis (Lee *et al*, 2004a), to give a value of conductivity of 1.59 x10^{-2}S/m. The real part of impedance spectra showed greater contribution compared to the imaginary part at lower frequencies, as expected. At higher frequencies, it falls due to dispersion effects resulting from onset of ac conduction. The calculation of the grain boundary conductivity and other parameters of the system have been carried out asuming the Brick Layer Model (BLM), at a temperature of 500K for samples x=0.50 and x=0.75. The relaxation frequencies calculated for the bulk and grain boundary processes are 9.43 x 10^{10}Hz and 6.6 x 10^{7}Hz, respectively. This is in accordance with the shorter relaxation time processes in the bulk compared to the grain boundary process. Further, the computed capacitances, based on equivalent circuit modelling using two *RC* parallel circuits in series, indicates a bulk capacitance value of 1.06 x10^{-12}F. In the case of the grain boundary, the capacitance value is 3.03 x10^{-10}F, these are within the characteristic values for the regions (Vitoo,1999; Sanchez-Bautista *et al*, 2010). The bulk properties of ionic materials

normally have smaller dielectric constant values, thus lowering their capacitance. The value of specific grain boundary conductivity, calculated based on the BLM is 3.36 x10^{-4}S/m, indicating that the bulk conductivity was much greater. Figure 4.9.3(b) is the characteristic complex impedance plot at 600K for the same sample which shows a decrease in the radii of the semicircles, pointing to a reduction in resistance with increase in temperature. Simialrly, the characteristic frequencies at the points of maximum imaginary impedance for the grain and grain boundary have increased to 13MHz and 520MHz, respectively. This led to an increase in the relaxation frequencies as a result of increased vibration of the ions with increase in temperature. Also with increase in temperature the semicircles further decreased in radii, a characteristic of ionic materials (Anantharamulu et al, 2008; Khatri et al, 2008).

The frequency dispersion for sample x=0.50 is depicted in figure 4.9.4. It can be seen that the characteristic behaviour, with the lowest (real part) ac conductivity being 5.16 x10^{-3}S/m at 309.5K, and the highest being 7.79 S/m at 599.6K. The conductivity also showed two dispersion regions (frequency independent region and the dispersive high frequency region) which are both thermally and frequency activated in accordance with standard ionic behaviour. The crossover point of the frequency independent plateau and the high frequency dispersive region shifted towards high frequency values with increasing temperature. This is due to the fact that with increasing temperature, the kinetic energy of the ions also increases and hence their vibrational frequency (Leo *et al*, 2002b). In their study of the system Li_2O:TiO_2:SnO_2:P_2O_5, lithium ionic conductor, Abrahams *et al* (2004) observed, at room temperature, a plateau in the real part of conductivity, which is limited at low frequencies by a decrease associated with the blocking Li^+ ions at the gold electrodes, and at high frequencies, by the onset of frequency dispersion. This may also be the

case here given that Pt blocking electrodes were used and Li^+ ion is one of the mobile species.

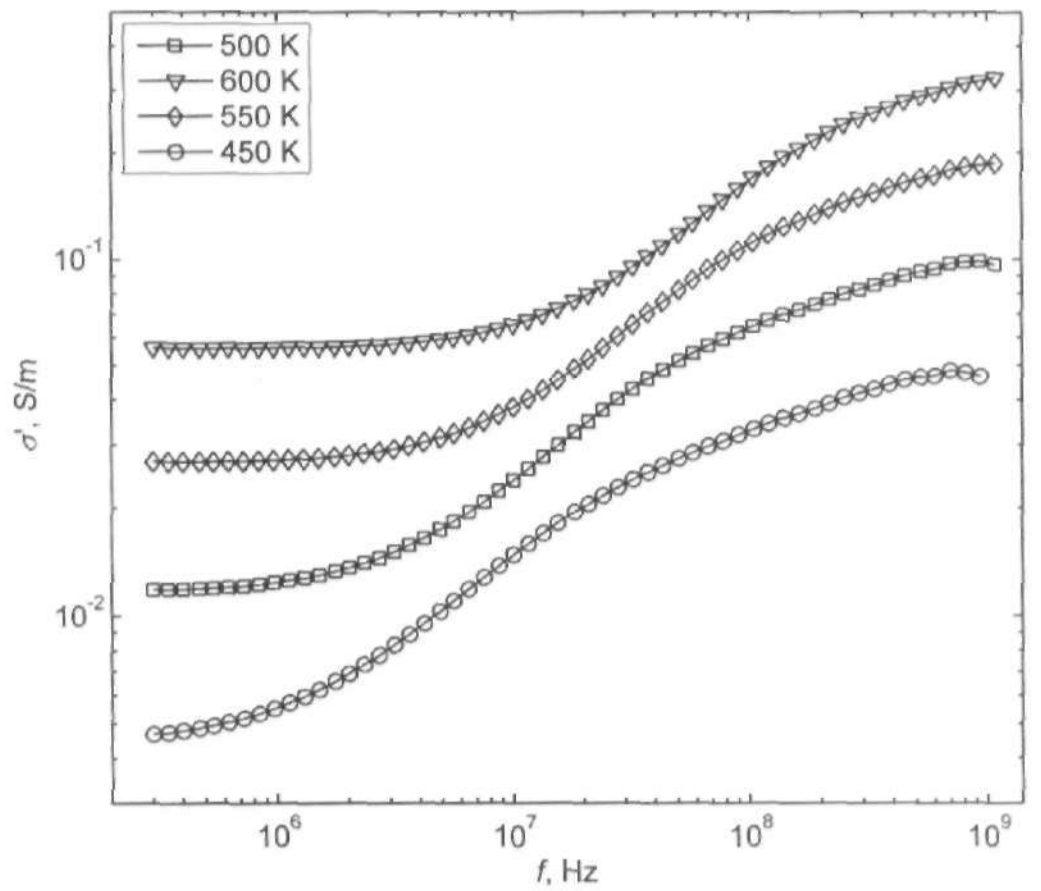


Figure 4.9.4: Plot of sintered sample x=0.50 showing the real part of conductivity σ' versus frequency f and the frequency independent and dispersion regions.

Figure 4.9.5 shows the frequency dependence of real part of conductivity for sample x= 0.75 at temperatures 400, 500 and 590K. The value of the estimated bulk conductivity is 0.01 S/m, 0.10 S/m and 0.30 S/m at the respective temperatures and the total conductivities are 0.01 S/m, 0.03S/m and 0.10 S/m. This shows that there is negligible grain boundary effects. The semicircles show increasing curvature (radii) with rise in temperature, implying that the conductivity increases also as is evident

from the values. The two parallel *RC* circuits in series were used as the equivalent circuit, figure 4.9.6(a). The corresponding relaxation frequency, ω_o and capacitance are 1.88 x10^9 Hz and 1.06 x10^{-8}F, respectively for the bulk. The spectra shows only the high frequency arc, there is minimal grain boundary effects. The small arc, which extrapolated to the real σ' axis on the high frequency arc gives the bulk condiuctivity. The spike is characteristic of slow diffusion processes occurring at the electrode/grain boundary or ceramics interface (Nga and Son, 2004; Lee *et al,* 2004a) and showed that electrode processes are significant. This usually leads to the accumulation of charge at low frequencies, leading to polarization and thus blocking behaviour of the electrodes. The impedance ranges for both the real and imaginary parts of impedance successively decreased with rise in temperature, figure 4.9.6(a-c), pointing to a fall in resistance. Further, the small grain boundary effect means that the grain sizes are large (as reflected in the SEM micrographs) and that there is connectivity between grains. Lefterova *et al* (2004) have attributed the arc and spur (straight line) to interfacial polarization, and is a proof of ionic conductivity appearance. Brunet *et al* (2003) in their study of two NASICON phases $Na_3Al_2(PO_4)_3$-I and $Na_3Al_2(PO_4)_3$-II, also observed a Na^+ ion blocking response at the surface of the Pt electrodes at low frequencies. Absence of grain boundary contribution could also be due to inhomogeneities present in the samples (XRD shows coexistence of a NASICON phase $Na_5Zr(PO_4)_3$ and the nature of the electrodes used (Forsyth *et al,* 1998). Also the relaxation frequency of the processes occurring in the system may have been too close to each other.

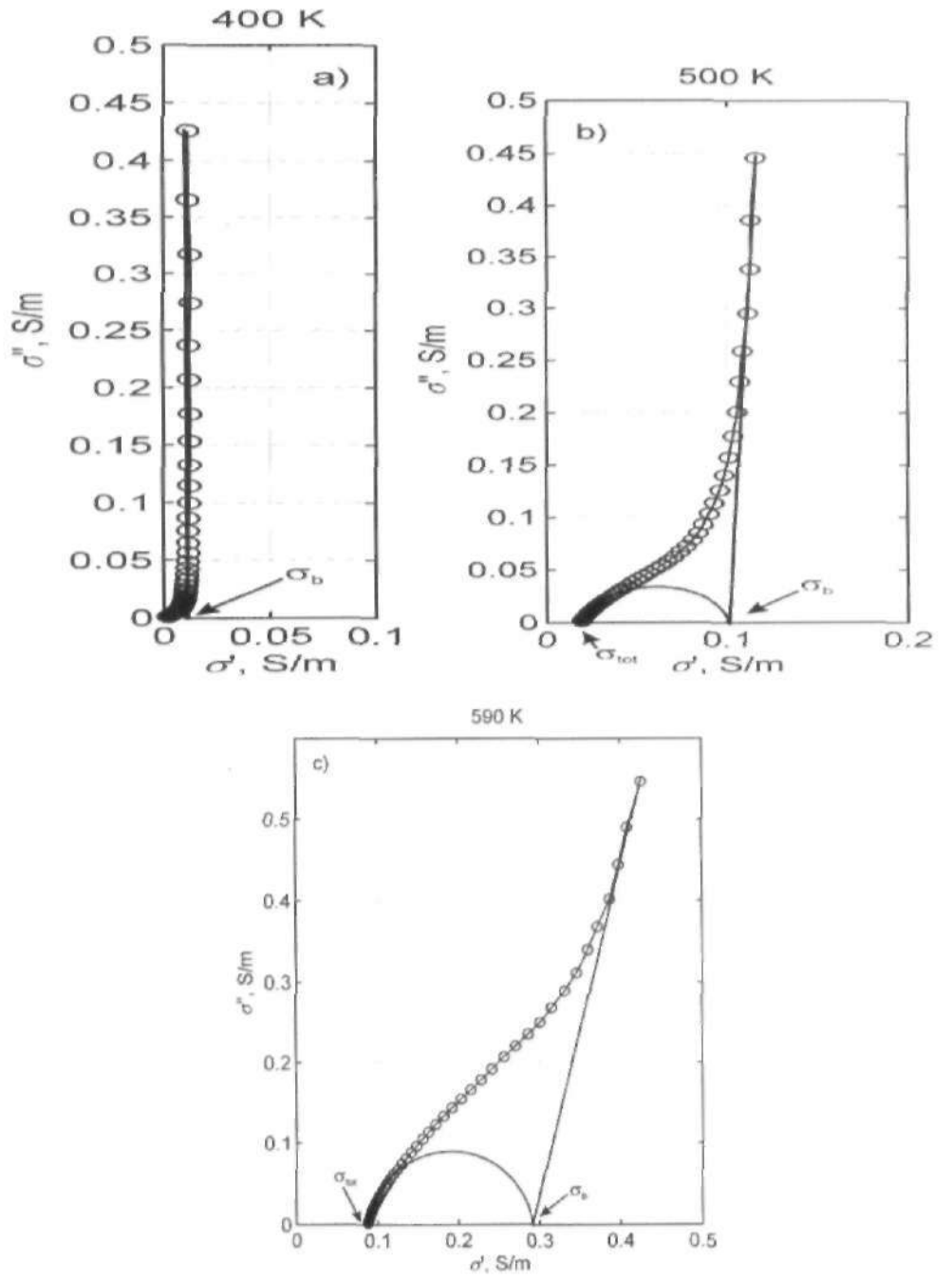


Figure 4.9.5: Complex conductivity plots at different temperatures 400K (a), 500K (b) and 590K (c) for composition x=0.75. The arrows point to the bulk (σ_b) and total conductivities (σ_{tot}), respectively.

The sample has larger range of values of conductivity (both σ' and σ'') compared to sample x=0.50, indicating that lithium substitution drastically reduced the resistance and hence the increased conductivity. This has lead to a fall in grain boundary resistance with subsequent decrease in the activation energy of the bulk.

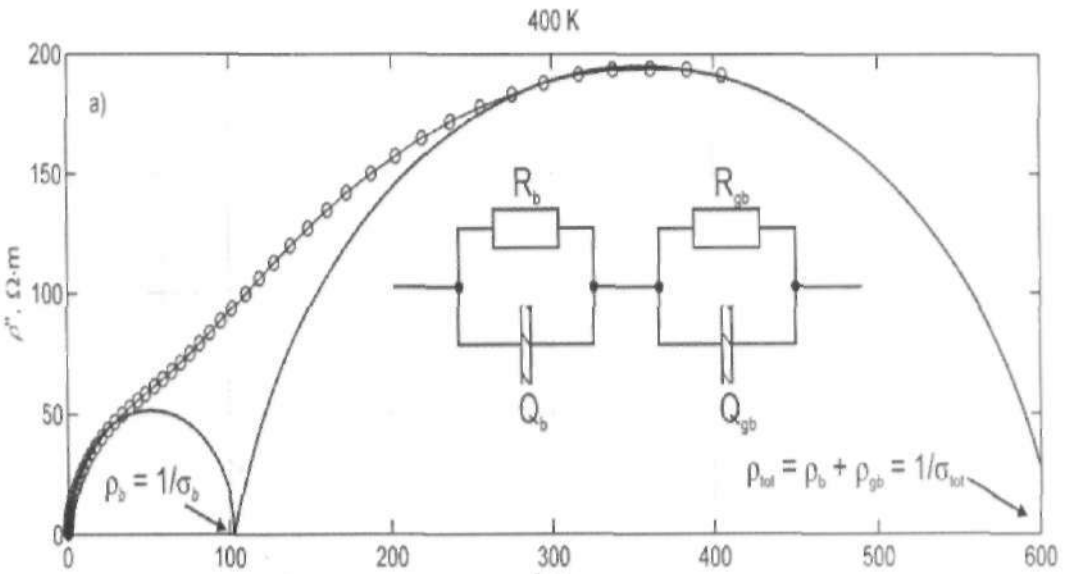


Figure 4.9.6(a): Complex impedance plots of x=0.75 at temperatures 400K. A reduction in the values of the real and imaginary parts of impedance is also observed with increasing temperature. R_b, Q_b are the resistance and capacitance and ρ_b, ρ_{gb} are the bulk and grain boundary ressitivity (intrinsic impedance).

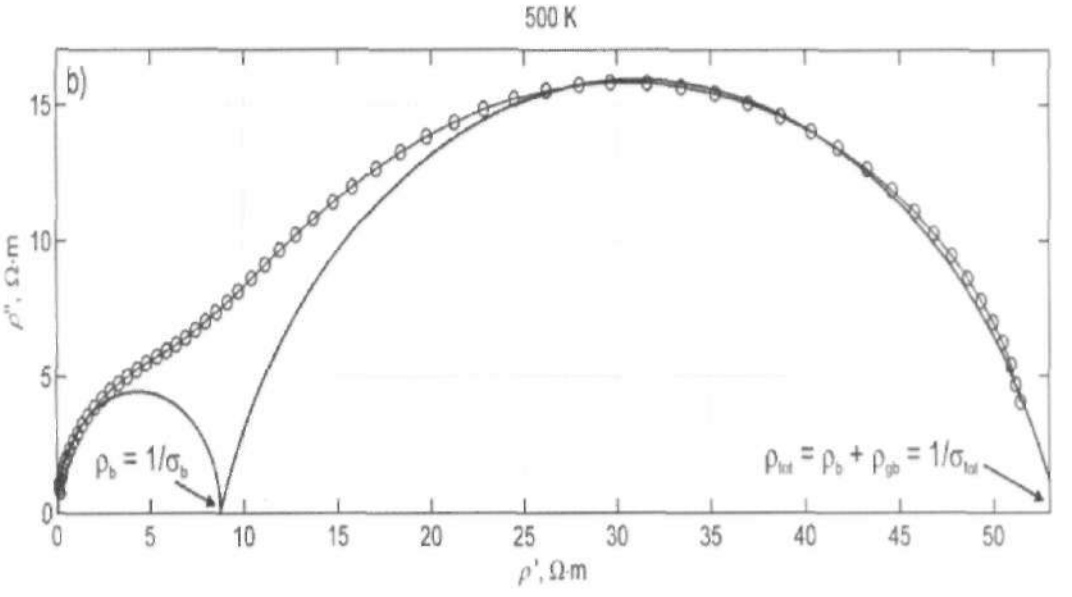


Figure 4.9.6(b): Complex impedance plots of x=0.75 at temperatures 500K. A reduction in the values of the real and imaginary parts of impedance is also observed with increasing temperature. ρ_b, ρ_{gb} and ρ_{tot} are the bulk and grain boundary and total ressitivity (intrinsic impedance).

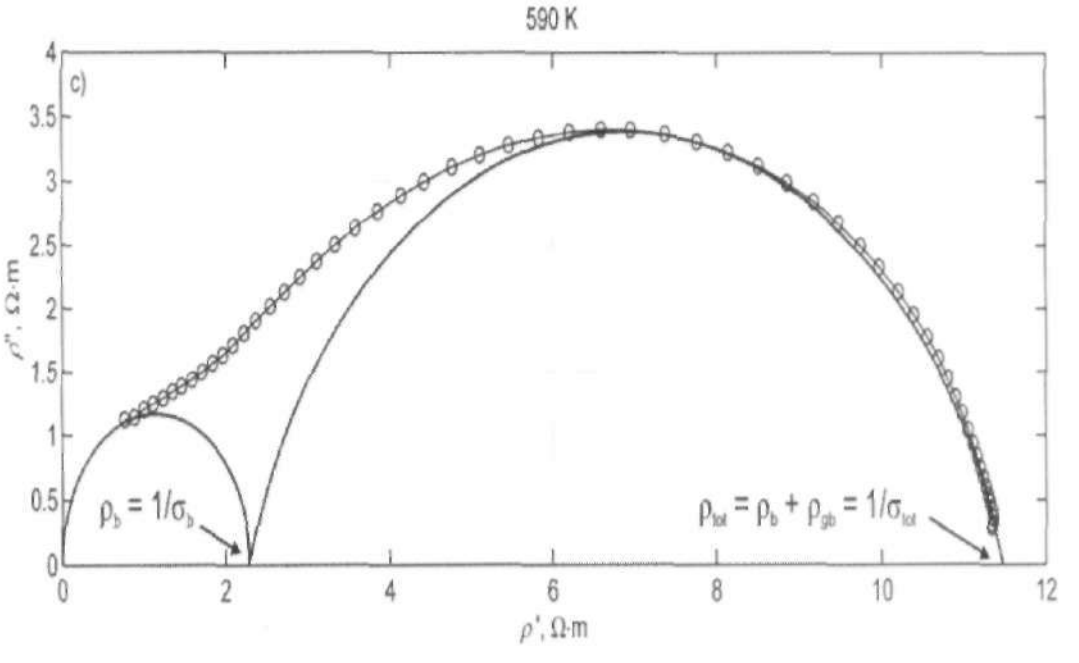


Figure 4.9.6(c): Complex impedance plots of x=0.75 at temperatures 590K. A reduction in the values of the real and imaginary parts of impedance is also observed with increasing temperature. ρ_b, ρ_{gb} and ρ_{tot} are the bulk, grain boundary and total ressitivity (intrinsic impedance).

The frequency dependence of real part of conductivity (σ') vs f for sample x=0.75 is shown in figure 4.9.7 and has the same character with that of x=0.50. Two dispersion regions, which are temperature activated can be seen. The plateau at the low frequency part of the plot represents the dc conductivity, attributed to the grain boundary processes. The beginning of the plateau marked the onset of ac conduction and it is typical of dispersion of conductivity. As the GHz frequency range is approached there seemed to be saturation or decrease of conductivity.

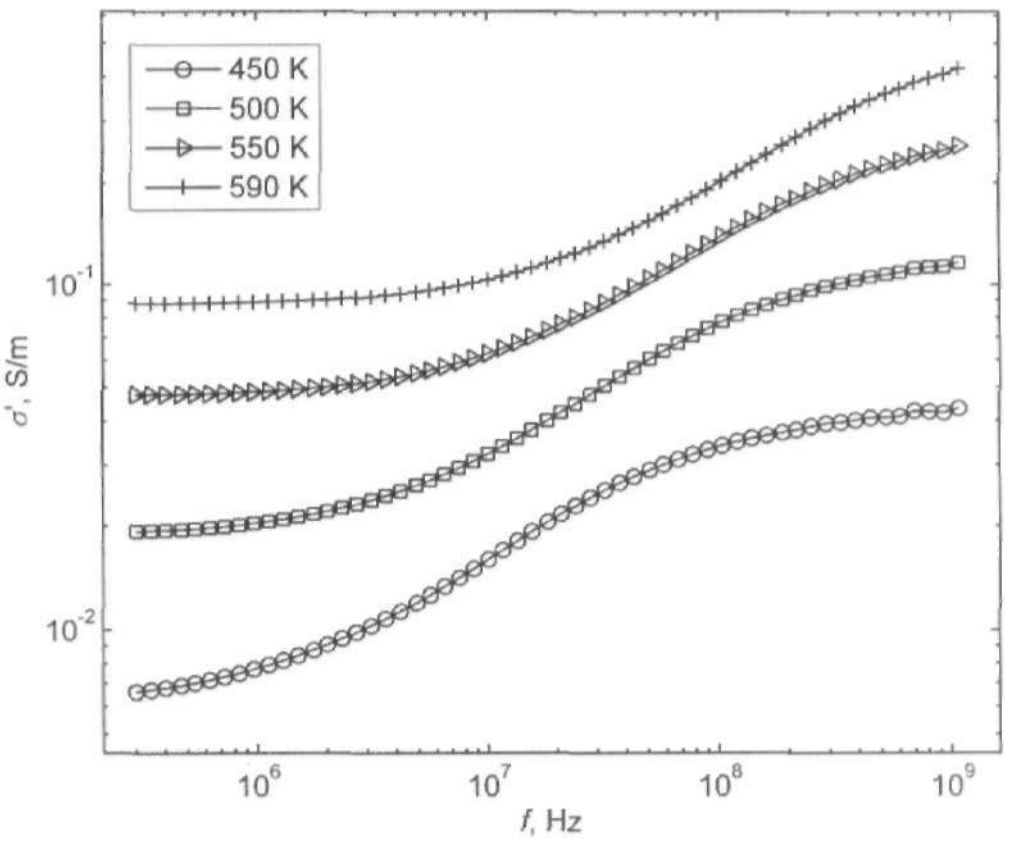


Figure 4.9.7: Plot of real part of conductivity σ' versus frequency f for sample x=0.75 between 450 and 590K.

The whole process is temperature activated and frequency dependent (Salkus *et al*, 2006a). This is one of the few studies characterized in the GHz range, apart from that of Salkus e*t al* (2006a, 2006b) and Kazakevičius *et al* (2004), and may therfore be the first for the current system. Most studies have been carried out in the MHz range of frequency (Forsyth *et al*, 1998; Kang and Cho, 1999; Lee *et al*, 2004b; Oda *et al*, 2007; Anantharamulu *et al*, 2008), and may probably explain why such behaviour may not have been observed. The highest value of real part of conductivity was obtained for the sample x=0.75, that is 22.80 S/m at 590K. The lowest real part of conductivity was 6.16 $x10^{-3}$ S/m at 310K. There has been reports of the observation of a low frequency dispersion behaviour in some compositions in the

$Li_{1+x}[(Ta_{1-2x}Ge_x)Al](PO_4)_3$ system. This occurs at different temperatures and has also been attributed to electrode polarization of mobile ions at the interface (Leo *et al*, 2002b), resulting in a decrease in electrical conductivity. Although the low frequency dispersion region was not observed, the space charge region (polarization) was found to be more effective at lower frequencies, which is the case here. It is therefore expected that the total ionic conductivity of the compound will decrease at a given temperature.

The impedance plot did not give good arcs for sample x=0.00. It was therefore difficult to calculate the bulk resistance or the grain boundary resistance either, rather, the total conductivity. This is because at the temperatures investigated, the sample showed extreme insulating properties. However, at higher temperatures the arcs begin to appear and thus there are more ions for conduction. The frequency dependence of conductivity plot for sample x=0.00 at 500K is shown in figure 4.9.8(a). This has similar characteristics with the previous samples. It is clear that only the high frequency dispersive region is visible, the low frequency dc response plateau is not. The sample shows extremely high ion localization, particularly at low temperatures and therefore very low conductivity. At 520K, the total conductivity is 8.00×10^{-5}S/m, the lowest for all the samples investigated, hence its having the highest activation energy of $0.56eV$. However, there appears to have been a subsequent delocalization of the ions with increase of temperature, and thus the increase in conductivity at 600K, the maximum temperature. The frequency dependence of the conductivity at 600K is shown in figure 4.9.8(b) and they share the same characteristic features with that at 500K. The drop in conductivity is seen to occur at about the same frequency and the maximum conductivity attained is higher within the same temperature, but is greater at this temperaature.

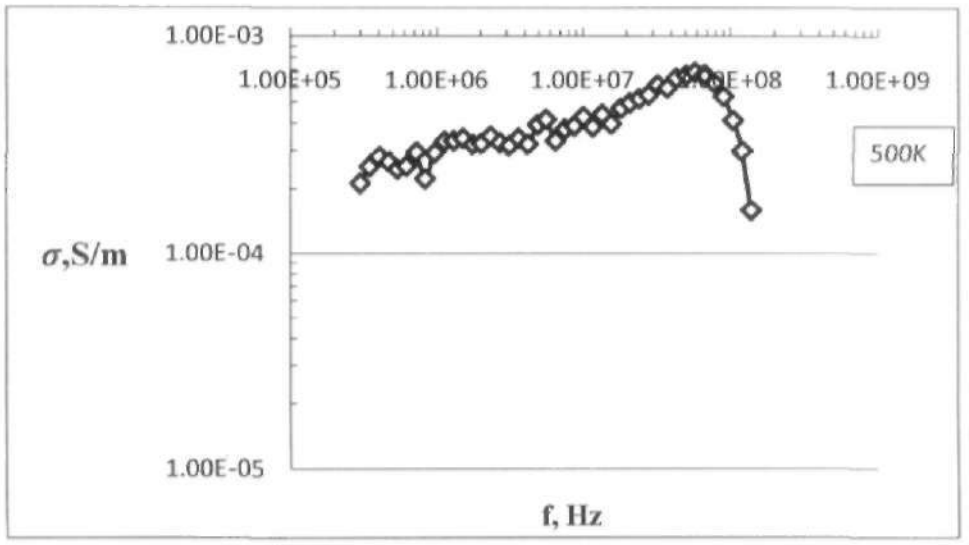


Figure 4.9.8(a): Plot of frequency dependence of real part of conductivity at 500K for sample x=0.00 showing the fall in conductivity at high frequencies.

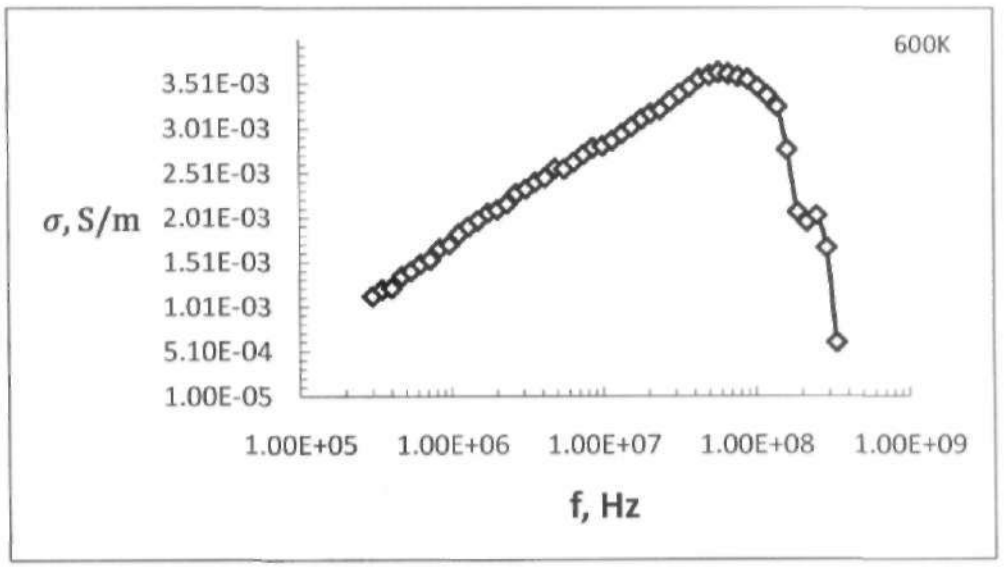


Figure 4.9.8(b): Plot of frequency dependence of real part of conductivity at 600K for sample x=0.00 showing the fall in conductivity at high frequencies.

At the GHz region, the conductivity suddenly dropped to zero, depending on temperature and frequency. Moreover, the sample has the smallest grain size, 1-1.5μm. Further studies need to be carried out on this sample. However, it is known that ZrO_2, a phase in the sample, reduces conductivity in NASICON (Essoumhi *et al*, 2006), thus the lowest ac conductivity of 2.01 $x10^{-5}$ S/m at 309K and highest conductivity of 3.58 $x10^{-1}$ S/m at 600K was observed. The corresponding total dc conductivities are 8.00 $x10^{-5}$ S/m at 520K and 4.19 $x10^{-4}$ S/m at 600K. It is generally observed that increase in lithium content also increased the conductivity, compared to the pristine sample x=0.00.

As a result of the presence of two ions in the samples x= 0.50, and 0.75, it is not possible to resolve which ion was responsible for the conduction, rather it is assumed that a cooperative mechanism is at play. NMR study is necessary to confirm this. It has been reported though, that where two mobile ions are present in the same system, and at a particular composition, it results in the lowering of conductivity of the system to a minimum, a phenomenon known as the 'mixed cation effect' observed in some glassy superionic conductors (Mouahid *et al*, 2001; Kawamura *et al*, 2007). Studies are rarely reported on this phenomena in NASICON. However, Mouahid *et al* (2001) is one such study. The authors observed a decrease in ionic conductivity with an increase in activation energy with increasing lithium content in the coupled ion (Na, Li) system $Na_{1+x}Ti_{2-x}Al_x(PO_4)_3$, which they studied in the MHz range of frequency. Na was being exchanged with Li. They concluded that it could be the 'mixed cation effect' that was observed, due to the presence of both Na and Li ions at the MI site, while Li was also detected at the MII site. The low value of conductivity was attributed to the blocking of the MI-MII pathway which made it difficult for ion motion across the channel. It has been observed that the

conduction channel in NASICON could be through the MI-MII or MII-MII pathways, depending on size and composition being studied. The MI-MI pathway does not seem to be favoured (Kumar and Yashonath, 2006). In the present work, decrease in conductivity is observed only at the GHz region and at almost all the temperatures investigated. Moreover, the samples with lithium content have greater conductivity. However, the same characteristic frequency dependence is also observed in the pristine sample x=0.00, but this cannot be attributed to the same effect. Most probably, to the presence of ZrO_2 or may point to a limit in the high frequency response of the system towards the GHz region. This has not been reported though, as some studies in the GHz region on NASICON would indicate (Kazakevičius *et al*, 2004; Salkus *et al*, 2006a; Salkus *et al*, 2006b). A similar phenomenon (Ribes *et al*, 2001) has been reported however, in the study of the glass ionic conductor $0.5Ag_2S$-$0.5GeS_2$, in a wide temperature (123-473K) and frequency range (up to the GHz region). Two more power law terms had to be added to the Jonscher's power law equation in order to fully describe the spectra. This suggests the need for a modification of the power law assumed in the present case, if indeed the observation turned out to be confirmed. It is important to note that this phenomenon was observed, in the case of glasses, at all temperatures and frequencies investigated, just as in the present work. The conduction mechanisms in these systems is assumed to be a hopping mechanism, both the dc and ac conduction are the result of the same ions, and therefore the same conduction mechanism is predicted. This can be obtained by determining both the dc value of conductivity (σ_o) in the frequency independent regions (plateau) and that of the relaxation frequencies at different frequencies and temperatures. They can then be fitted to the Arrhenius equation, together with their determined activation energies. The closeness of these values to that of the dc

conduction, can determine whether the conduction mechanisms are the same. This has been assumed in this case, since such a situation has been reported on NASICON (Leo *et al*, 2002a; Anantharamulu *et al*, 2008).

4.4.1 Arrhenius Conductivity

The results for the dc conductivity measurements for three samples (x=0.00,0.50 and 0.75) are depicted in the Arrhenius plot of figure 4.9.9. There is clear evidence of increasing dc conductivity with increase of lithium in the samples in accordance with the fitting to the Arrhenius equation. The total and bulk conductivities are indicated for all the samples. The grain boundary conductivity could be calculated by extrapolation to the real impedance axis on the Nyquist plot for sample x=0.50, it is not well distinguished for the other samples.

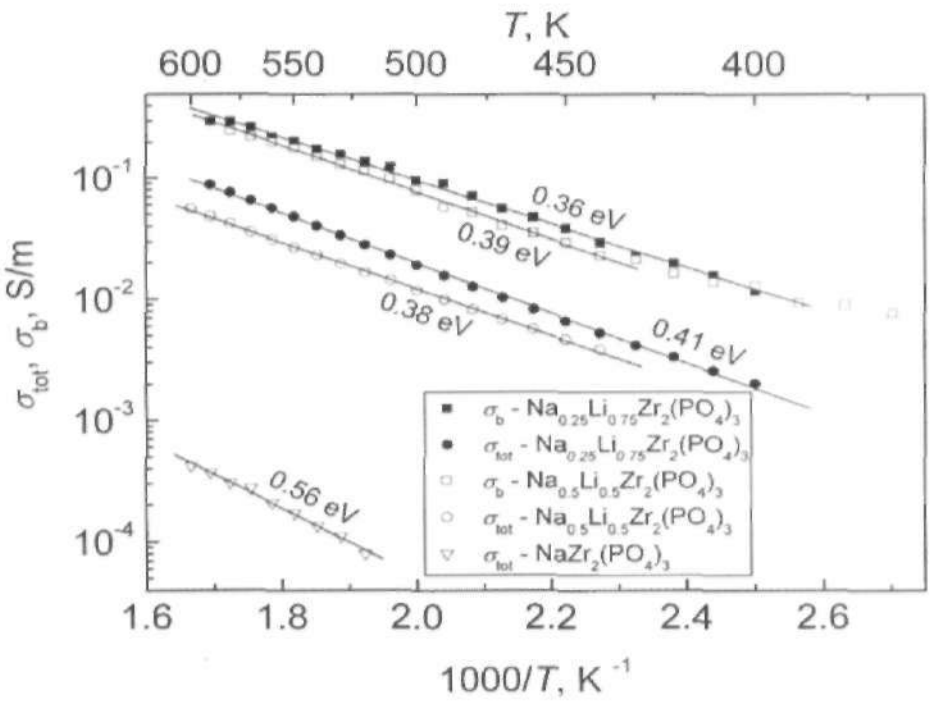


Figure 4.9.9: Arrhenius plot of sintered samples $Na_{1-x}Li_xZr_2(PO_4)_3$ (x=0.00-0.75) showing the bulk (σ_b) and total conductivity (σ_{tot}) at different temperatures.

It can be observed from the figure that the x=0.00 sample showed extreme ion localization at moderate temperatures and therefore the conductivity is very small. It has the lowest conductivity of 0.8×10^{-4}S/m, even at temperature of 520K. The fit for the x=0.00 sample is as good as 0.97. The activation energy, E_a= 0.56 *eV* at 520K, and is the highest, and this may point to a change of conduction mechanism, compared to the other compositions. Brunet *et al* (2003) for example, in his study of the phases of the system $Na_3Al_2(PO_4)_3$, explained that the increase of the activation energy observed at a certain temperature points to a new conduction mechanism or may be due to increase of mobile species, which is not true in this case, as the ion has the least conductivity. Furthermore, the large value of the activation energy may indicate a non localized motion, a rather microscopic diffusion of Na^+. The activation energy of the bulk dc conductivity for all the samples (except x=0.00) is approximately 0.4*eV*, a value that compares well with other NASICON compounds. Similarly, Jasinski *et al* (2005) obtained the same value (0.4*eV*) as activation energy of conduction for the system $Li_{14}Zn(Ge_4O_{16})$, called Lisicon, an ionic conductor for sensors.

The bulk conductivity for the samples x=0.50 and 0.75 and their activation energies (bulk and total conductivity) are virtually the same, while 0.78 and 0.88 respectively are the measures of the fit for the activation energy. This points to the same conduction mechanism and is characteristic of hopping motion of the ion from one lattice site to another. The highest conductivity for the bulk (0.3S/m at 590K) is obtained for x=0.75, followed by the bulk conductivity (0.25S/m at 580K). The activation energies ranged from 0.36-0.56*eV*, and may also point to a common mechanism of conduction (Fuentes *et al*, 2004; Xu Nian *et al*, 2004).

A summary of the most important electrical parameters for the samples at different temperatures together with their activation energies are given in table 4.2.

Table 4.2 : Summary of the bulk (σ_b) and total (σ_t) electrical conductivities and activation energies E_a of the investigated compositions at selected temperatures as deduced from the Arrhenius data together with their uncertainities.

Sample	bulk (σ_b, S/m)		E_a, (eV)	total (σ_t, S/m)	E_a, (eV)
x=0.00	520K	-	-	8.07×10^{-5}	0.56±0.01
	600K	-	-	4.19×10^{-4}	-
x=0.50	370K	7.70×10^{-3}	0.39±0.03	2.02×10^{-3}	-
	580K	0.25	-	3.84×10^{-3} (440K)	0.38±0.01
x=0.75	400K	1.18×10^{-2}	0.36±0.03	8.81×10^{-2} (590K)	0.41±0.01
	590K	0.30	-	2.02×10^{-3} (400K)	-

In table 4.3, a comparison has been made between the results obtained from the present work and from selected literatures on conductivities of NASICON materials at selected temperatures. Their highest conductivities together with their activation energies have been particularly compared. The result from the table showed that the bulk conductivity (σ_b) obtained at both temperatures, 400K and 590K from the present work are almost equal to that of NASICON at 1383K (Dong-mei *et al*, 2007) and greater than that at 400K by Mouahid *et al* (2001), which is the highest obtained for the composition. The results from this work also show improvement both in activation energy and conductivity compared to the best for the composition $Li_{1.4}Al_{1.2}Sb_{0.8}(PO_4)_3$ studied by Anantharamulu *et al* (2008). The total

IM LIBRAR

conductivity (σ_t) was also comparable to that obtained by Kazekevicius *et al* (2004) at 600K, with the same activation energy E_a= 0.41eV. This shows that the synthesized materials have improved conductivities based on the processing method used.

Table 4.3: Summary of bulk (σ_b), total (σ_{tot}) electrical conductivities at selected temperatures and their activation energies (E_b, E_{tot}) for different NZP Compositions, compared with sample from the present work, $Na_{0.25}Li_{0.75}Zr_2(PO_4)_3$.

Composition	T, K	σ_b, S/m	E_b, Ev	σ_{tot}, S/m	E_{tot}, eV	Reference
$Na_{0.25}Li_{0.75}Zr_2(PO_4)_3$	400	1.16×10^{-2}	0.36±0.03	2.02×10^{-3}	0.41±0.01	Present work
	590	0.30		8.81×10^{-2}		Present work
$Li_{1.3}Sc_{0.3}Zr_{1.7}(PO_4)_3$	600	-	-	4.54×10^{-2}	0.41	Salkus *et al*, 2006
$Li_{1.3}Z_{1.4}Ti_{0.3}Al_{0.21\ 0.09}(PO_4)_3$	300	6.1×10^{-3}	0.22	-	-	Nga and Son, 2007
$Na_3Zr_2Si_2PO_{12}$	1383	0.36	-	-	-	Dong-mei *et al*, 2007
$(Li,Na)_{1.8}Ti_{1.2}Al_{0.8}(PO_4)_3$	400	1.5×10^{-4}	0.66	-	-	Mouahid *et al*, 2008
$Li_{1.4}Al_{1.2}Sb_{0.8}(PO_4)_3$	423	-	0.77	4.7×10^{-6}	1.37	Anantharamulu *et al*, 2008

CHAPTER FIVE

SUMMARY, CONCLUSION AND RECOMMENDATIONS

5.1. *Summary and Conclusion*

Sodium zirconium phosphate belonging to the NASICON family of composition $Na_{1-x}Li_xZr_2(PO_4)_3$ (x=0.00, 0.25,0.50 and 0.75) has been synthesized by the method of solid state reaction. The substitution of Li in increasing amounts in the compositions was observed to increase the thermal stability and hence accelerate the formation of the product phase. The compositions show high air stability and no structural transformations were observed.

The compostions have been characterized by X-ray diffraction techniques for phase, structure, lattice parameters, density and crystallite size. Most of the compositions were mainly single phase with small amounts of ZrO_2 and $Na_5Zr(PO_4)_3$ phases detected. The crystal system of all the compositions showed that they belonged to the rhombohedral symmetry of the R-3c space group and were indexed based on hexagonal lattice structure. Although the lattice parameter 'a' was higher than obtained in literature for the x=0.00 sample, the 'c' parameter was within the range obtained for the materials and showed a fairly linear relationship with increasing incorporation of lithium. This high value was attributed to several factors, the most probable of which is the inability to perform the XRD scan at a lower rate (step scan mode). However, the theoretical densities calculated from the lattice parameters were close to those obtained from literature. Similarly, the experimental densities were 60% in most samples, showing that the degree of densification attained was relatively high. Comparable data or literature was not available for compositions

other than x=00, however (except x=0.50). This may thus be the first time such compositions were being investigated.

The SEM micrographs of the materials showed generally, large grains with narrow distribution of particle sizes. The microstructure images also showed dense particles with virtually no porosity and at least, in one case, a liquid-like phase belonging to a glass phase was observed. This was confirmed by the XRD results and has been previously reported to result in decrease in the conductivity of the composition. The crystallite sizes were found to be within an average of 5μm and were fairly uniform sized. In some cases, small crystallite sizes were obtained which were within values obtained for the NZP family in general.

Impedance spectroscopy of the compositions carried out between 300kHz and 3GHz and temperature range 300-600K, showed two distorted semicircles in the composition x=0.50, and a semicircle and an inclined straight line in the composition x=0.75.The pristine sample x=0.00, however, did not give good impedance arcs at the investigated temperatures due to its highly insulating properties. The result is consistent with that for ionic materials, which represent the bulk and grain boundary processes in the former case, and the grain boundary as well as electrode processes in the latter. The impedance spectra did not show high values of impedance at successively higher temperatures, hence their enhancement in conductivity. The graph of temperature-dependent conductivity for the bulk and the total conductivity for the samples, gave a straight-line, reflecting the Arrhenius character. The conductivity spectra for the $Na_{1-x}Li_xZr_2(PO_4)_3$ system, showed total dc conductivity maximum of 8.8 x10^{-2}S/m at 0.41eV activation energy, at a temperature 600K and 2.02 x10^{-3}S/m at 400K, respectively. Their activation energies were within

the range for ionic materials and specifically those observed for NASICON. These values have been enhanced in some samples whereas others are within what is obtained in literature.

The frequency dependent conductivity produced two dispersion regions, reflecting the bulk and grain boundary processes and was observed to shift towards higher frequencies as the temperature increased. In the compositions x=0.50 and x=0.75, at frequencies close to the *GHz* region, a drastic fall in conductivity was observed. This was suspected to be related to the 'mixed cation effect' which has been reported in glassy superionics. Though the case of x=0.00 sample, which showed similar behaviour, was suspected to be due to a different phenomenon, most probably a limitation in the high frequency conductivity response of the system. Further investigations are required for a definitive resolution of the problem.

In conclusion, the work has demonstrated that $Na_{1-x}Li_xZr_2(PO_4)_3$ system, which belongs to the NZP family can be synthesized under the prescribed processing conditions. Most importantly, it showed that it is possible to synthesize NASICON using solid state reaction, and avoid the formation of ZrO_2 second phase in some compositions. Moreover, the microstructure images showed that the sizes of the grains and their distributions are within what is normally obtained for these compounds, showing that there was no compromise of the physical parameters in the process.

One important finding is that the lithium substituted compositions have greater thermal stability than the lithium free compounds, and that there was no structural transformation observed, within the temperature range of investigation. Moreover, since the characterizations were carried out in air, they also showed great air stability. All these properties make them important for applications as electrolytes in solid state

batteries, barring other parameters that need to be tuned, among other applications. A most useful property are the values of conductivity attained in the two lithium compositions, x=0.50 and x=0.75. The values are high enough to be applied in devices and are comparable to what has been achieved in other ion conducting NASICON, whereas in others, the parameters have been enhanced, although the temperature is still high. It is possible though, to make further improvements on the parameters by sintering for longer period of time to improve densification and minimizing the phases present through microwave synthesis. Lithium substituted compounds have higher conductivity due to the appropriateness of the channel sizes for lithium motion. The total conductivity for x=0.50 and x=0.75 are 1.59 $x10^{-2}$ S/m (500K) and 0.10 S/m (590K), respectively. Because it is abundant, light-weight and environmentally friendly, it is more suitable for applications than other contending members. The use of BLM, to calculate the conductivity of the compounds has shown that the electric parameters can be correlated with the microstructure and thus fits the model. Moreover, the fact that in spite of the presence of two ions in the system, the doped compositions showed cooperative character in the conductivity for most of the frequency ranges studied, except about 2 GHz range of frequency and beyond (and at all temperatures investigated), where conductivity decreases. This implied that the 'mixed cation effect' may have been observed. NMR studies are required to determine the ion responsible for the electrical conduction together with complete structural analysis, to determine the site occupancies of the various lattice sites, particularly, the MI and MII sites. Also to determine the conduction mechanisms for both the ac and dc, further analyses of the impedance data are required.

Finally, the study has provided fundamental crystallographic data to complement the current ones on the $NaZr_2(PO_4)_3$ system. In addition, thermal and

electrical properties have been determined, providing a holistic understanding of the systematic changes in the parameters of the system investigated, which was correllated with the electrical parameters and microstructure.

5.2 Future Work

The data obtained from this work and the experimental design can be improved in the future as follows:

1. Microwave method of synthesis should be used in order to explore all its advantages. The sintering conditions should be followed at each stage of the heat treatment with XRD and SEM, to ascertain the formation of the product phase so that optimal conditions for synthesis can be established.
2. High precision X-ray diffraction machine (and high power SEM) capable of scanning from lower 2θ values up to 80^{0} 2θ should be used, together with provision for 'step scan mode' to make the peaks observable (resolvable to 0.02^{0} 2θ or better) and to get wider range of reflections in order to enhance the values of the lattice parameters, among others. The higher power SEM should increase the resolution of the micrographs too.
3. Structural analysis software such as GSAS or RIETAN should be used to determine the composition of each phase, refine the lattice parameters, determine the site occupancies and bond angles, so that the effect of the substitutions in the structure and conduction mechanism can be evaluated and established. This is because the range of 2θ values obtained in the present work is not adequate for a full crystallographic structure analyses.
4. An investigation of the spatial distribution of the ions (Na,Li) and their mobility should be carried out using Nuclear Magnetic Resonance (NMR) or XPS (X-ray photoelectron spectroscopy) on the mixed compositions. This should provide further explanation on the mechanism of electrical conduction and the mobile ion (s) responsible for it.

5. Infrared spectroscopy, using Fourier Transform infrared (FT-IR) spectroscopy should be used to determine the vibrational spectra of the compounds, particularly, the attempt frequencies for the ion motion in their lattice sites.
6. The atomic compositions of the synthesised compositions should be quantified in order to ensure that compositions of correct stoichiometry have been synthesized, energy dispersive spectroscopy, or other appropriate techniques may be used to quantify the Na: Li ratio and other elements.
7. The impedance obtained from the experimental data should be fitted using the complex non linear least squares (CNLS) fitting procedure in order to obtain a correllation of experimental and theoretical imterpretation of data with the physical process in the system. Similarly, a modification of the ac conductivity expression (according to the Jonscher's power law) should be undertaken to take cognizance of the observed fall in conductivity toward the GHz frequency. Also, the ac activation energies for both relaxation frequency ω_o and dc component σ_o of the ac conductivity, together with mobile ion concentration should be determined, so that the mechanism of conduction can be established.
8. The phase transitions for all the sintered compositions, from room temperature-1473K should be investigated so that a phase diagram may be built for the system.

5.3 Recommendations

The following recommendations are specifically directed at the scientific-academic community, the private sector and the government (particularly, at the federal and state levels), except otherwise stated :

1. Against the backdrop of the incessant fuel crises in the country, there is need to establish research in the area of NASICON materials, in order to complement energy requirement in the transport sector through investment in research in Solid Oxide Fuel cells.
2. The urgent need to establish research in the area of rechargeable Li-ion batteries cannot be overemphasized, what with the current users of mobile phones hitting the thirty million mark, and an increasing number of laptop computer users, all using Li-ion batteries.
3. The government should also invest in research in the NZP materials for the purporse of immobilization of nuclear wastes, as we inch towards nuclear power option for energy supply. This is due to their demonstrable immobilization potentials and ease of reprocessing wastes.
4. Our Industries can also harness the potentials of research on NZP and NASICON in general, due to their enormous diverse properties and applications in many areas, such as low thermal expansion and thermal shock resistance, among others.
5. Our Universities and allied research bodies should facilitate the acquisition and establishment of a workable mechanism for materials characterization facilities and their sustainability, such as XRD, SEM, Impedance spectroscopy analyzer systems, among others. This will additionally serve as revenue

generating ventures for the relevant agencies, apart from providing the necessary facilities for exploring and developing our mineral potentials and achieving research objectives. Almost all the characterizations in the present work were carried out outside the country.

6. The Physics departments in the Universities, among others, should acquire important materials characterization facilities, if only to boost internally generated revenue and establish linkages with other foreign Universities to help would-be researchers in the field. Funding should also be made available for researchers in the field in view of the dearth of relevant and key facilities currently in the country.

References

Aboulaicha, A., Boucheta, R., , Torteta, L., Delaizirb, G., Seznecc, V.,Vallet, V., Dollé, M.(2009). Analysis by EIS of the relationship between structural, textural and electrical properties in ceramics : $Li_{1-x}Al_xA_{2-x}(PO_4)_3$ (A=Ge and Ti) case: http://www. electrochem.org/meetings/scheduler/abstracts/216/3179.pdf. Retrieved, June, 2010.

Abrahams, I., Hadzifejzovic, E. and Dygas, J.R. (2004). Structural and electrical characterisation of $Li_2O : TiO_2 : SnO_2 : P_2O_5$ electrolyte glass. *D a l t o n T r a n actions*, 3: 1339 –3 1 35.

Achary, S.N., Jayakumar, O.D., Patwe, S.J., Shinde, A.B., Krishna, P.B.R., Kulshreshtha, S.K. and Tyagi, A.K. (2008). Neutron diffraction studies on $Ca_{1-x}Ba_xZr_4P_6O_{24}$ solid solutions. *Pramana Journal of Physics*, 71: 941-946.

Ahmadu, U. (2005). Electrical conductivity investigations on silver sulphate–lithium sulphate based superionic conductors. Unpublished M.Sc. Thesis. Ahmadu Bello University, Zaria, Nigeria.

Ahmadu, U., Musa, A.O. and Jonah, S.A. (2008). Sintering characteristics and energy applications of sodium superionic conductors (NASICON): *A Review. Bayero Journal of Physics and Mathematical Science*, 1:182-189.

Ahmadu, U., Musa, A.O., Jonah, S.A. and Isah, K.U.(2009). Research and development in Nigeria: A survey of facilities, problems and Institutional Issues in the synthesis and Characterization of sodium zirconium phosphate (*in press*).

Ahmadu, U., Musa, A.O., Jonah, S.A. and Rabiu, N. (2010). Synthesis and thermal characterization of NZP compounds $Na_{1-x}Li_xZr_2(PO_4)_3$ (x=0.00–0.75). *Journal of Thermal Analysis and Calorimetry*, 101:175-179. DOI 10.1007/s10973-010- 0679-y.

Agrawal, D. K., Harshe, G., Breval. E. and Roy, R. (1996). [NZP], $NaZr_2P_3O_{12}$-type materials for protection of carbon-carbon composites. *Journal of materials Research*, 11:3158.

Agrawal, D., Cheng, J., Fang ,Y. and Roy, R. (2006). Microwave processing of ceramics, composites and metallic materials. *In*: Clark, D. E., Folz, D. C., Fogar, C. E. and Mahmoud, M. M. (Eds), *Microwave solutions for ceramic engineers*. The American ceramic society, Ohio,USA. p.213.

Akbar, S., Dutta, P. and Lee, C. (2006). High temperature ceramic gas sensors: A review. *International Journal of Applied Ceramic Technology*, 3:306.

Allan, N.L., Barera, G.B., Purton, J.A., Smiss, C.E., and Taylor, M.B. (2000). Ionic solids at elevated temperatures/or pressures: Lattice dynamics, molecular dynamics, Monte Carlo and *ab initio* studies. *Physical Chemistry and Chemical Physics*, 2:1094-1111.

Anantha, P. S. (2004). Transport studies of some sodium ion conducting dispersed solid electrolytes, polymer electrolytes and glasses. Unpublished synopsis of PhD. Thesis. Indian Institute of Technology, Madras, Chennai , India.p.1.

Anantharamulu, N., Prasad, G. and Vithal, M. (2008). Preparation, characterization and conductivity studies of $Li_{3-2x}Al_{2-x}Sb_x(PO_4)_3$. *Bulletin of Materials Science*, 31(2):133–138.

Anderson, A.S., Kalska, B., Jonson, P., Hagstrom, L., Nardhblad, P., Tellgreen, P. and Thomas, J.O. (2000). The magnetic structure and properties of rhombohedral $Li_3Fe_2(PO_4)_3$. *Journal of Materials Chemistry*, 10 :2542

Angadi, B., Jali, V.M., Lagare, M, T., Kini, N.S., and Umarji, A.M. (2002a). Synthesis and thermal expansion hysteresis of $Ca_{1-x}Sr_xZr_4P_6O_{24}$. *Bulletin of Materials Science*, 25:191-196.

Angadi, B., Jali, V.M., Lagare, M. T., Kini, N.S., Umarji, A.M., Kumar, R., Arora, S.K., Kanjilal, D. (2002b). 50 MeV Li^{3+} irradiation effects on the thermal expansion of $Ca_{1-x}Sr_xZr_4P_6O_{24}$. *Nuclear Instruments and Methods in Physics Research B*, 187: 87–94.

Aniya, M. (1992a). Pseudopotential study of bonding in the superionic conductor AgI. *Journal of Physical Society of Japan*, 61:4474-4483.

Aniya, M. (1992b). A Chemical Approach for the microscopic mechanism of Fast ion transport in solids. *Solid State Ionics*, 50:125-129.

Aniya, M. (1996a). Chemical trends in the real space pseudo potential of zinc-blende structure binary compounds. *Journal of Physics and Chemistry of Solids, 57:*1811-1816.

Aniya, M. (1996b). A Simple formulation of bond fluctuations in superionic conductors. *Journal of Physical Society of Japan*, 65:3406-3407.

Aniya, M. (2006). Chemical bonding in ionic conductors (3). *In*: Sakuma, T. and Takahashi, H.(Eds) *Physics of Solid State Ionics*. Research Signpost, Trivandrum, Kerala, India, p.47.

Aono, H. (1994). Studies On Li^+ ionic conducting solid electrolyte composed of Nasicon-type structure. PhD. Thesis. Osaka University, Japan.p.8.

Arbi, K., Ayadi-Trabelsib, M. and Sanz, J. (2002). Li mobility in triclinic and rhombohedral phases of the Nasicon-type compound $LiZr_2(PO_4)_3$ as deduced from NMR spectroscopy. *Journal of Materials Chemistry*, 12:2985.

Ayliffe, H.E., Frazier, A.B., and Rabbitt, R. D. (1999). Electric impedance spectroscopy using microchannels with integrated metal electrodes. *IEEE Journal of Microelectromechanical Systems*, 8:50.

Battacharya, A. J., Middya, T.R., and Tarafdar, S. A. (1998). Computer simulation study of ionic conductivity in polymer electrolytes. *Pramana Journal of Physics*, 50:1-14.

Bellino, M. G., Lamas, D. G and Walsöe de Reca, N.E. (2005). Enhanced ionic conductivity in heavily doped ceria nanoceramics. *Diffusion Fundamentals*, 2: 47.1 - 47.2.

Best, A.S., Newman, ,P. J, MacFarlane, M.R., Nairn, K.S., Wong, S. and Forsyth, M. (1998). Characterization and impedance spectroscopy of substituted $Li_{1.3}Al_{0.3}Ti_{1.7}(PO_4)_{3-x}$(Z=V, Nb) ceramics. *Journal of Materials Chemistry*, 8: 2199.

Biao, Z. Jingkum, G. and Peinan, Z. (1996). Thermal expansion behavior of $KZr_2P_3O_{12}$-$SrZr_4P_6O_{24}$. *Science in China* (series E), : 337-339.

Bierberle, A. (2000). The electrochemistry of solid oxide fuel cell anodes: Experiments, modelling, and simulations. Unpublished PhD. Thesis. Swiss Federal Institute of Technology, Zurich, Switzeland.

Bonanos, N., Steele, B. C. H. and Butler, E. P. (2005). Microstructural Models for Impedance Spectra of Materials. *In:* Barsoukov, E. and Macdonald, J. R.(Eds), *Impedance Spectroscopy Theory, Experiment, and Applications, Second Edition.* A John Wiley & Sons, Inc., Publication, Hoboken, New Jersey, USA..pp1-47.

Bothe, J.V. and Brown. (2005). Low temperature formation of NZP ceramics: http://www.netl.doe.gov/publications/proceedings/03/ucr-hcbu/Brown/pdf. Retrieved December, 2009.

Bouari, A. El and Jazouli, A. El. (2004). Crystal structure of $Pb_{0.5}Ti_2(PO_4)_3$. *Phosphorus Research Bulletin*, 15:136.

Breval, E., Harshe, G. and Agrawal D.K. (1995). Synthesis and chemical stability of $NaSn_2P_3O_{12}$. *Journal of Material Science Letters*, 14:728-731.

Brown, P. (2004). Nanostructured ceramics and composites for refractory Applications in coal gasification : http://www.netl.doe.gov/publications/processing/03/ucr-hcbu/Brown.pdf. Retrieved, August, 2009.

Brown, P. (2005). Nanostructured ceramics and composites, final progress report, Penn state University, U.S.A: http://*www.osti.gov/bridge/servlets/purl/840414-AWwSQv/native/840414.pdf.* Retrieved, October, 2009.

Brunet, F., Bagdassarov, N. and Miletich, R. (2003). $Na_3Al_2(PO_4)_3$, a fast sodium conductor at high pressure: in-situ impedance spectroscopy characterization and phase diagram up to 8 GPa. *Solid State Ionics,* 159:35-47.

Calleja, M. and Dove, M.T. (2004). Calculating activation energies in diffusion rocesses using a *monte carlo* approach in a grid environment. *In*: Mubarak, M. et al (Eds), *ICCS 2004,LNCS 309*. Springer-Verlag, Berlin Heidelberg, Germany. pp 483-490.

Carvajal, J .J., Pareu, I., Sale, R., Solarus, X., Dianz, F. and Aguilo, M. (2005). Growth and structural *characterization* of $Rb_3Yb_2(PO_4)_3$:A new material for laser and nonlinear optical applications. *Chemistry of Materials*, 17:6746-6754.

Catti, M. and Stramare, S. (1999). ISIS experimental report, Rutherford Appleton laboratory, date of report, 24/5/1999.

Ciobanu, C., Liu,, Y.,Wang, Y.and Patton, B. R. (1999). Numerical calculation of electrical conductivity of porous electroceramics. *Journal of Electroceramics,* 3:17.

Chen, T. (2003). Preparation, thermal expansion, and dielectric properties of $MTi_4P_6O_{24}$(M = Ba, Sr): http://www.etdncku.lib.ncku.edu.tw/ETD-Search-c/view-etd?URN=etd-0674103- 163524. Retrieved, November, 2008.

Colomban, P. and Gouadec, G. (2005). The ideal ceramic fiber/oxide Matrix composite : How to conciliate antagonist physical and chemical requirements ?*In*: Lamon, J. (Ed), *Annales De Chimie (Lavoisier) N° Special Les Composites Céramiques*, 30:4.

Cruz, A.M. and Rodriquez, A.C.M. (2007). Impedance spectroscopy and microstructure of lithium conducting Li_{1+x} $[Al_xGe_{2-x}$ $(PO_4)_3]$ glass ceramics. *Ceramica,* 53:180.

Donald, I. W., Metcalfe, B. L. and Taylor, R. N. J. (1997). The immobilization of high level radioactive wastes using ceramics and glasses. *Journal of Materials Science,* 32 : 5864

Dongare, M.K., Singh, P. and Suryavanshi, P.M. (1992). Hydrothermal synthesis and characterization of sodium zirconium phosphates. *Materials Research Bulletin,* 27:637-645.

Dong-mei, Z., Fa, L., Zang-long, X., Wang-Cheng, Z. (2007). Phase formation and electrical characteristics of NASICON ceramics. *Transactions of nonferrous Metal Society of China*, 17:s1156-s1159.

Essoumhi, A., Favotto et, C., Satre, P., Mansori, M.,Ouzaouit, K. , EL Hichou, A. (2006). New ionic conducting ceramics of NASICON type: synthesis and characterizations. *Moroccan Journal of Condensed Matter*, 27:87.

Fisher, C.A.J. and Mastubara, H. (1998). Oxide ion diffusion along grain boundaries in zirconia: A molecular dynamics study http://www.eng.hawaii.edu/~ssi11/SSI-11Papers/B72/B72.pdf *Retrieved, June, 2010.*

Fleig, J. and Maier, J. (1998). The influence of the microstructure on the impedance of ceramics studied by finite element calculations: http://www.fkf.mpg.de/maier/people/fleig/webjur3.pdf.p.50. Retrieved, June, 2010.

Fleig, J., Jaminik, J. and Maier, J. (2000). On the validity and limits of the brick layer model in impedance spectroscopy:http:// www.fkf.mpg.de/maier/people/fleig/rio98b.pdf. Retrieved, January, 2010.

Forsyth, M., Wong, S. Nairn, K.M., Best, A.S., Newman, P.J. and MacFarlane, D.R. (1998). NMR studies of modified Nasicon-like, lithium conducting solid electrolytes: http://www.eng.hawaii.edu/~ssi II/SSI-II papers/C55/C55.pdf. Retrieved, August, 2009.

Fuentes, R.O, Marques, F .M. B. and Franco, J .I. (1999). Synthesis and properties of nasicon prepared from different zirconia-based precursors. *Boletin de la sociedad Espanola de Ceramica Y Vidrio. V*, 38:631-634.

Fuentes, R.O., Lamas, D.G., Fernandez de Rapp M.D., Figueiredo, M. N., Frade, J.R., Marques, F. M. B. and Franco, J. I. (2004).Restrictions to obtain NASICON by a ceramic route. *Boletin de la sociedad Espanola de Ceramica Y Vidrio V*, 43: 775-779.

Furusawa, C. (2006). Fabrication and ionic conduction of ionic conducting thin films. *In*: Sakuma, T. and Takahashi, H.(Eds), *Physics of Solid State Ionics*. Research Signpost, Kerala,India. pp.273-283.

Gautham, D. (2006). Characterization of the conduction properties of alkali metal ion conducting solid electrolytes using thermoelectric measurements.Unpublished PhD. Thesis.Max-Planck-Institut für Metallforschung, Stuttgart,Germany.

Gimenez,,I. F. and Alves, O, L. (1999). Formation of a Novel Polypyrrole/Porous Phosphate Glass Ceramic Nanocomposite. *Journal of Brazilian Chemical Society*,10: 167-168.

Gopalakrishna, G.S., Doreswamy, B.H., Mahendra, M.J., Sridhar,M.A, Prasad, J.S. and Ashamanjari, K.G. (2005). Hydrothermal synthesis and characterization of new NASICON related Potassium Iron(III) Pyrophosphate. *Bulletin of Materials Science*,28:1-7.

Grey-Weal, A. (2007). Screening and Strain in Superionic Conductors. *Faraday Discuss*, 134:297-313.

Hawkins, H. T. Spirling, D. R. Smith, D. M., Hampel, F. G., Veirs, D. K. and Scheetz, B. E. (2000). Site Preferences of Actinide Cations in [NZP] Compounds. *In:* Pillay, K.K.S. and Kim, K.C.(Eds), *Plutonium Futures-The Science.* American Institute of Physics. pp.168-169.

Hazen, R.M., Finger, L.W., Agrawal, D.K., McKinstry, H. K. and Parrotta, A.A. (1987).High-temperature crystal chemistry of sodium zirconium phosphate (NZP). *Journal of Materials Research,* 2:329-337.

Heimann, R.B. (2002). Materials Science of Crystalline Bioceramics: A review of basic properties and applications. *CMU. Journal*, 1:19.

Holmström, E., Nordlund, K. and Kuronen, A. (2010). Threshold defect production in germanium determined by density functional theory molecular dynamics simulations. *Physica Scripta*, 81:1-5.

Huang, C-Y, Agrawal, D.K. McKinstry, H.K., and Limaye, S. (1994). Synthesis and thermal expansion behaviour of $Ba_{1+x}Zr_4P_{6-2x}Si_{2x}O_{24}$ and $Si_{1+x}Zr_4P_{6-2x}Si_{2x}O_{24}$ systems. *Journal of Materials Research,* 9:2005-2013.

Ignaszak, A. , Pasierb, P. and Komornicki, S. (2006). The effect of humidity on the electrical properties of NASICON-type materials. *Materials Science-Poland, 24:* 95-102.

Izumi, F. (1989). RIETAN: a software package for the Rietveld analysis and simulation of x-ray and neutron diffraction patterns. *The Rigaku Journal*, 6:10.

Jackson, T.B. and Porter, W. D. (2001). Environmental Microcracking of (NZP) type Ceramics:http://ww.osti.gov/bridge/servelets/purl/102178-4Sm09M/102178.pdf. Retrieved, November, 2009.

Jaeger, H., Pechan, M.J. and Lotis, D.K (1998). Materials Physics: A new contemporary Undergraduate laboratory. *American Journal of Physics*, 66:724-730.

Jasinski, G., Jasinski, P., Chachulski, B., Nowakowski, A. (2005). Lisicon Solid Electrolyte Electrocatalytic gas sensor. *Journal of the European Ceramic Society*, 25:2969.

Jasinski, G., Jasinski, P., Chachulski, B., Nowakowski, A. (2006). Electrocatalytic gas sensors based on Nasicon and Lisicon. *Materials Science-Poland,* 24:263.

Judes, J., Kamaraj,V. (2009). Preparation and characterization of yttria stabilized zirconium minispheres by the sol-gel drop generation method. *Materials Science–Poland,* 27:409.

Kalu, P. N., Waryoba, D. and Rollet, A. D. (2008). X-ray difractometer, EML 5930,Spring 2008, advanced materials characterization and miscrostructural analysis:http://www.neon.mems.cmu.edu/rollet/27750/L8A_Micro_1a.ppt. Retrived, June, 2009.

Kang, H. and Cho, N. (1999). Phase Formation ,Sintering behavior, and electrical characteristics of NASICON compounds. *Journal of Materials Science*, 34:5005-5013.

Karasik, B.S. and McGrath,W.R.(1997). Microwave transmission technique for accurate impedance characterization of superconductive bolometric mixers. *Appled Physics Letters*, 71:97-1293.

Karian, M., Galvin, M. E.,Ttrapa, T. E., Sadoway, D.R. and Maxes, A.M. (2005). Single ion conducting Polymer–Silicate nanocomposites electrolytes for lithium battery applications. *Electroceramica Acta,* 50 :2125-2134.

Kartini, E, Sakuma, T.,Purwanto, A., Kamiyama,T. and Collins, M. F.(2004). Conductivity and structure of superionic compound $(AgI)_{0.6}(NaPO_3)_{0.4}$: http:// www.ncnr.nist.gov/acns/program/ACNS2004Program.pdf.Retrieved, November, 2008.

Kawamura, J.,Kuwata, N.,Hattori,K. and Misuzaki, J. (2007). Ionic transport in nanohetergenous materials. *Reports of the Institute of Fluid Science*, 19:1-2

Kazakevičius, E. Orliukas, A. F. , Kežionis, Jucius, A. L., Dindune, A., Kanepe, Z. Ronis, J. (2004). Synthesis and electrical properties of $Li_{1+x}Zr_{2-2x}Al_xTi_x(PO_4)_3$. *Materials Science (Medžiagotyra),*10: 305.

Kerrache, A., Horbach, J. and Binder, K. (2008). Molecular-dynamics computer simulation of crystal growth and melting in $Al_{50}Ni_{50}$. *A letters Journal of Exploring the Frontiers of Physics*, 81:1-6.

Kežionis, A., Kazakevičius, E., Šalkus, T., Orliukas, A.(2010). Broadband high frequency impedance spectrometer with working temperatures up to 1200 K (*Solid State Ionics , in press*)

Khatri, P., Behera, B., Srivanus , V. and Choudhary,R. N. P. (2008). Complex impedance spectroscopic properties of $Ba_3V_2O_8$ ceramics. *Research Letters in Materials Science,* 2008:3.

Kidner, N.J. Homrigaus,. J. Ingram, B.J. Masoni, Garboczi, E. J. (2005). Impedance/Dielectric spectroscopy of electroceramics–Part1: Evaluation of composite models for polycrystalline ceramics. *Journal of Electroceramics,* 14: 283.

Kim, I.J. and Kim, H.C. (2004). Zero level thermal expansion materials based on $ZrTiO_4$-Al_2TiO_5 ceramics synthesized by reaction sintering. *Journal of Ceramic Processing Research, 5:308.*

Kleeberg, R. (2005). Pitfalls in Rietveld phase quantification of complex samples. Microstructure analysis in materials science, Freiberg, June 15 – 17.

Kormaneni, S., Lenain, E., Roy,R. (1986). Thermal expansion of $NH_4Zr_2(PO_4)_3$. *Journal of Materials Science Letters*, 5:1-3.

Kotelnikov, A.R., Kovalskii, A.M., Karyaeva E.G., Orlova, A.I. ,Pet'kov, V.I., Akhmedzanova, G.M. and Ushakovskaya, T.V.(2001). Investigation of (Na,Sr)-Zirconium Phosphate solid solutions: http://www.libray.iem.ac.ru.exper/V8__2/six.pdf. Retrieved,December, 2008.

Kotelnikov, A.R., Kovalskii, A.M., Karyaeva, E.G., Orlova, A.I., Petkov, V.I., Chichagove, A.V., Ushakovskaya, T.V. and Ulin I.V. (2009). Investigation of (Na, K)-zirconium-phosphate experimental study. *Crystal growth, structure and physical properties of crystals,* 7: 68-69.

Kumar, P. and Yashonath S. J. (1999). Structure, conductivity and ionic motion in $Na_{1-x}Zr_2Si_xP_3O_{12}$:A simulationstudy:http://www.iitg.ernet.in/physics/ fac/padmakumarp/Nasicon.JPG/Nasicon-full. Retrieved, July, 2008.

Kumar, P.P. and Yashonath, S. (2006). Ionic conduction in the solid state. *Journal of Chemical Science,* 118(1):135-154.

Kutucktu, M.N. (2005). Synthesis and characterization of low and negative thermal expansion materials. Unpublished M.Sc. Thesis. Georgia Institute of Technology, Georgia.

Lai, W. and Haile, S.M. (2005). Impedance spectroscopy as a tool for chemical and electrochemical analysis of mixed conductors: A case study of ceria. *Journal of American Ceramic Society,* 88: 2979.

Larson, A.C. and Von Dreele, R.B. (2004). *General Structure Analysis System (GSAS)*, Los Alamos National Laboratory Report, LAUR 86-748, USA .

Lasia, A. (1999). Electrochemical Impedance spectroscopy and its applications. *In*: Conway, B.E., Bockris, J.O'M and White, R. E.(Eds.), *Modern aspects of electrochemistry, no.32*. Kluwer Academic Publishers, New York.pp.143-231.

Lee, J.-H., Jung,Y.-S., Woo, H.-S., Chung,Y.-C., Kim,D.-Y. (2004). Spatial distribution of resistive intergranular phase in stabilized zirconia estimated by millicontact impedance spectroscopy. *Journal of the European Ceramic Society,* 24:1129 1133.

Lee, J.S., Chang, C.M., Lee, Y.I., Lee, J.H. and Hong, S.H. (2004a). Spark plasma sintering (SPS) of NASICON Ceramics. *Journal of American Ceramic Society*, 87:305-307.

Lee, J.-S., Lee, J.-H and Hong.,S.-H. (2004b). Solid-state amperometric CO_2 sensor using a sodium ion conductor. *Journal of the European Ceramic Society*, 24:1431.

Lee, W.Y.,Cooley,K.M., Berndt, C.C., Joslin, D.L. and Stintin, D P. (1996). High-temperature thermal plasticity of plasma-sprayed $Ca_{0.5}Sr_{0.5}Zr_4P_6O_{24}$ coatings on NASICON/Sic ceramic matrix composite and Ni-based super alloy substrates. *Journal of American Ceramic Society*, 799:2759-62.

Lefterova, E. D., Kanazirsky, I. A., Bliznakov, S. T., Ilcheva, V. G., and Dimitriev, Y. B.(2004). Impedance and structural investigation of glasses from the system $2TeO_2.V_2O_5$-Ag_2O-AgI. *Impedance Contributions Online,* 2:2-1 –2-8.

Leo, C. J., Chowdari, B. R., Subba Rao, G.V. and Souquet, J. L. (2002a). Lithium conducting glass ceramic with NASICON structure. *Materials Research Bulletin,* 37:1419-1430.

Leo, C.J., Rao, G.V.S. and Chowdari, B. V. R. (2002b). Fast ion conduction in the Li-analogues of Nasicon,$Li_{1+x}[(Ta_{1-2x}Ge_x)Al](PO_4)_3$. *Journal of Materials Chemistry,* 12:1848–1853.

Lessing, P. A. and Huestis, G. (2006). Synthesis of nanocrystalline NASICON-type thin film ceramics. *Journal of Ceramic Processing Research,* 7:1-2.

Macdonald, J. R.(1987). *Impedance Spectroscopy: Emphasizing Solid Materials and Systems,* Wiley-Interscience Publication, New York .

Macdonald, J. R. and Johnson, W. B. (2005). Fundamentals of impedance spectroscopy. *In*: Barsoukov, E. and Macdonald, J.R.(Eds), *Impedance spectroscopy theory, experiment, and applications, second edition.* A John Wiley & Sons, Inc., Publication, Hoboken, New Jersey, U.S.A. pp.1-47.

Maier, J. (2005). Nanoionics: ion transport and electrochemical storage in confined systems. *Nature Materials,* 4: 805-815.

Maldonado-Manso, P., Aranda, M.G., Braque, S.,S and, J. ,Losilla, E.R. (2005). Nominal Vs, actual Stoichiometroies in Al doped NASICONs: A study of the $Na_{1.4}A_{l0.4}M_{1.6}(PO_4)_3$ (M=Ge,Sn,Ti,Hf,Zr) family. *Solid State Ionics,* 176:1613-1625.

Manthiram, A. (2009.). Phospho-Olivine cathodes for lithium-ion batteries. The Electrochemical Society *Interface,* Spring 2009.

Maliki, M., Micoulat,M., Chaimbault, F. and Vaills,Y. (2006). Correlation between floppy to rigid transitions and non Arrhenius conductivity in glasses, *Physical Review Letters*, 96:

Mallick, H. and Sarkar, A. (2000). An experimental investigation of electrical conductivities in biopolymers. *Bulletin of Materials Science,* 23:319-324.

Mao, Z. Sinnott, S.B. and Dickey, E.C. (2002). *Ab Initio* calculations of pristine and doped zirconia_5 (310)/[001] tilt grain boundaries. *Journal of American Ceramic Society,* 85:1594–1600.

Masciocchi, N. (1997). The contribution of powder diffraction methods to structural crystallography: rietveld and ab–initio techniques.*The Rigaku Journal*, 14:10-16.

Mass, P., Meyer,M. Bunde, A. and Dieterich, W. (1996) .Microscopic explanation of non Arrhenius conductivity in glassy fast ionic conductors. *Physical Review Letters,* 7:1528-1531.

Materials Evaluation and Engineering (MEE, 2006). Handbook for Materials Evaluation.Plymouth, Minnesota, USA.pp5-49.

Matsubara, H. And Fisher, C.A.J. (1998). Oxide ion diffusion along grain goundaries In zirconia: A molecular dynamics study: http://www.eng.hawaii.edu/~ssi11/SSI-11Papers/B72/B72.pdf ,1998. Retrieved, October, 2010.

Mitchell, B.S. (2005). Formation and characterization of highly interfacial hybrid nanocomposites. *Review of advanced Materials Sciene,* 10:240.

Mouahid F.E., Zahir M., Maldonado-Manso P.M., Bruque S., Losilla E.R., Aranda M.A.G., Rivera A, Leona C, Santamaria J. (2001). Na-Li exchange of $Na_{1+x}Ti_{2-x}Al_x(PO_4)_3(0.6\leq x\leq 0.9)$ NASICON series: a Rietveld and impedance study. *Journal of Material Chemistry,* 11:3258-3263.

Naik, A.H., Thakkar, N.V., Darwatkar, S.R., Mudher, K.D.S., Venagopal, V.V. (2004). Microwave assisted low temperature synthesis of sodium zirconium phosphate ($NaZr_2(PO_4)_3$). *Journal of Thermal Analysis and Calalorimetry,* 76:707-713.

Naik, A. H., Deb, S. S, Chalke, A. B., Saxena, M. K., Ramakumar, K. L., Venugopal, V. and Dharwadkar, S.R. (2010). Microwave-assisted low temperature synthesis of sodium zirconium Phosphate (NZP) and the leachability of some selected fission products Incorporated in its structure–a case study of leachability of caesium. *Journal of Chemical Science,* 122: 71–82.

Nakayama, S. and Itoh, K. (2003). Immobilization technique of cesium to $HZr_2(PO_4)_3$ using an autoclave. *Journal of Nuclear Technology*, 40:631-633.

Nga, N.T. and Son T. (2004). Interaction model of the interface NASICON with aqueous solution. *Communication in Physics*, 4:105-110.

Nian Xu, Y.,Chung, S.Y.,Bloking, J.T., Chiang, Y.M. and Ching, W.Y. (2004). *Electrical and solid state letters*, 76: A131-A134.

Nowinski, J. L., Mrocczkwoska ,M., Garbarczyk, J.E., and Wasiucionek, M.(2006). Crystallization Process AgI-AgO_2-P_2O_5([AgO_2]/[P_2O_5] glasses. *Material Science-Poland*, 24:

Oda, K. Takase, S. and Shimizu, Y. (2007). Preparation of high conductive lithium ceramic. *Material Science Forum*, 544-5:1033-1036.

Othman, M. H. D., Ismail, A. F., Mustapha, A. (2007). Physico-Chemical study of sulfonated poly(ether ketone) membranes for direct methanol fuel cell application. *Malaysian Polymer Journal (MPJ), 2:10-28.*

Ozmen, B. (2004). Hydrothermal Synthesis of Solid State Materials and Crystallography. Unpublished M.Sc. Thesis. Izmir Institute of Technology, Izmir, Turkey.

Park, H.J., Munir, Z.A. and Kim, S. (2010). Grain boundary protonic conductivity in highly dense nano-crystalline Y-doped $BaZrO_3$. *Journal of the Korean Ceramic Society*, 47:71.

Park, Y., Chab, S., Saitob, Y., Prinz, F.B. (2005). Gas-tight alumina films on nanoporous substrates through oxidation of sputtered metal films. *Thin Solid Films*, 476:168.

Pasciak, G., Chmielowiec, J. and Bujlo, P. (2005).New Ceramic superionic materials for IT SOFC applications. *Materials Science-Poland*, 23:209-219.

Paul, M. (2007). Crystal Structure and Crystal Geometry: http://www.ce.berkeley.edu/paulmont/CE60/New/crystal_structure.pdf. Retrieved, October, 2009.

Petkov, V.I., Orlova, A.I., Trucbach, I.G., Asabina, Y.A., Demarin, V.T. and Kurazhkovskaya, V.S. (2003a). Immobilization of nuclear waste materials containing different alkali elements in single-phase NZP-based ceramics. *Czechoslovak Journal of Physics*, 53: A639-A648.

Pet'kov, V.I. and Orlova ,A.I. (2003b). Crystal-chemical approach to predicting the thermal expansion of compounds in the NZP family. *Inorganic Materials*, 39 :1013-1023.

Pet'kov,V. I., Asabina, E.A., Markin,, A. V. and Smirnova, N.N. (2008). Synthesis, characterization and thermodynamic data of compounds with NZP structure. *Journal of Thermal Analysis and Calorimetry,* 91: 157-8.

Potapova, A., Zhuravleva, M., Smirnova I., Spiridonov, F., Zimina, G. and Novoselov, A.(2008). High conducting heterovalent substituted NASICON-like phases in $ScPO_4$-Na_3PO_4 Quasibinary system. Materials Research Society Symposium Proceedings, Vol.1100, 1100-JJ07-05.

Raistrick, I.D., Franceschetti, D. R. and Macdonald, J. R. (2005). Theory. *In*:. Barsoukov, E. and Macdonald, J. R. (Eds), *Impedance spectroscopy theory, experiment, and applications, second edition*. A John Wiley & Sons, Inc., Publication, Hoboken, New Jersey.pp.1-47.

Ramasesha, S. (1999). Science and Technology of Ceramics. *Resonance,?:23-24.*

Ribeiro, M.C. (2005). Metallic phosphates in biomedical applications-development, chemistry and structure. Unpublished PhD. Thesis. *Universidade Do Porto*, Portugal.

Ribes, M., Bychkova, E and. Pradel, A. (2001). Ion transport in chalcogenide glasses: dynamics and structural studies. *Journal of Optoelectronics and Advanced Materials*, 3:665 – 674.

Rollet, A. D. and Kalu, P. N. (2008). X-ray difractometer, EML 5930, Spring 2008, advanced materials characterization and miscrostructural analysis:www.neon.mems.cmu.edu/rollet/27750/L8A_Micro_1b.ppt. Retrived, June, 2009.

Sadoway, D.R. and Mayes, A.M. (2003). Portable power: Advanced rechargeable lithium batteries. *MRS Bulletin*, August.

Sakuma, T. Basar, K., Shimoyama,T., Hosaka,D., Xianglian and Arai,M. (2006). Static and dynamic structure in solid state ionics. *In*: Sakuma, T. and Takahashi H.(Eds), *Physics of solid state ionics*.Research Signpost , Kerala, India.

Salkus, T., Dindune, A. ,Kanepe, Z. Ronis, J. Kazeonis, A. and Orliukas, A. E. (2006a). Synthesis Structure and Electric properties of $L_{1+x}Sc_xZ_{2-x}(PO_4)_3$(x=0.1,0.2,0.3). *Lithuanian Journal of Physics, 46*:361-366.

Salkus, T., Dindune, A., Kanepe, Z., Ronis, J., Kezionis, A., Kazakevicius, E., Gaukckler, L.J., Mucke, U.P. and Orliukas, A.F. (2006b). Electric properties of lithium conducting solid electrolyte ceramics. *Lithuanian Journal of Physics,* 46: 483-488.

Sánchez-Bautista, C., Santos-García, A. J. D., Peña-Martínez, J. and Canales-Vázquez, J.(2010). Processing of samarium doped ceria for IT-SOFC: grain boundary effect on the electrical conductivity.*Bol e t in de la soci edad e s pañola de*, 49:7-14.

Siekerski, M., Nadara, K. and Rzeszotarski, P. (2006). Conductivity simulation in composite polymeric electrolytes. *Journal of New Materials for Electrochemical Systems, 9:375-390.*

Shimojo, F. (2006). Atomic dynamics in superionic conductors, *ab initio* molecular dynamics simulations. *In*: Sakuma, T. and Takahashi, H.(Eds), Physics of solid state ionics. Research signpost, Keralla, India. pp.70-86.

Simmer, S. P.,Wu, P., and Dunn, B. (1998). Solution processing approaches for solid electrolytes and electrode materials, *Journal of Materials Research*, 13:868.

Singh, K. and Bhoga, S.S. (1998). The ion conduction mechanism of isovalent cation-doped Li_2SO_4. *Applied Physics A : Materials Science & Processing*, 67:475.

Slater, P. (2007). Design of ionic and mixed cation conductors. *In*: Keay-Bright, Sarah (Ed), Accelerated Materials Discovery for Energy Storage and Conversion Devices. Meeting Report. St Antony's College, Oxford, UK, 2nd-4th April, REF: UKERC/MR/MP/2007/012., UKERC Meeting Place. pp.15-16.

SMAHT Ceramics (2004). Brochure. Salt Lake city, USA. WSRC-STI-2007-00366, REVISON 0.

Smith, J. B. (2005). Oxygen ion conductivity measurements: brief summary and introduction. Unpublished PhD. Thesis. University of Oslo, Norway: http://www.wiley-vch.de/books/sample/3527313427_c01.pdf. Retrieved, December,2009.

Smirnova, O.A, Kharton, V.V. and Marques, F.M.B. (2004). Ssynthesis and characterized Sodium-cation conducting $Na_x(M_yL_{1-y})O_2$ ($M=Ni^{2+},Fe^{3+},;L= Ti^{4+},Sb^{5+}$). *Boletin de la sociedad Espanola de Ceramica Y Vidrio. V.*, 43:79-685.

Song, S.-J, Moon, Lee, T. H., Dorris, S. E. and Balachandran, U. (2008). Space charge potential of proton conducting $BaCe_{0.8}Y_{0.2}O_{2.9-\delta}$. *Journal of Ceramic Processing Research,* 9:377.

Stenina, I.A.,,Kilitsyn, M.N.,Pinus,I.Yu, Haile, S.M. and Yaroslavtsev, A.B. (2006). Phase transitions and ion conductivity in NASICON type compounds $Li_{1\pm x}Zr_{2-x}M_x(PO_4)_3$, M=Ta,Nb,Y,Sc,). *Defect and Diffusion Forum*, 249:255-262.

Sumiata, S. ,Mariyanto, E.K. and Adi, A. (2005). Pressure dependence of crystal structure and ionic conductivity of composite $(AgI)_{0.7}(AgPO_4)_{0.3}$. pp.111-125. linkinghub.elsevier.com/retrieve/pii/S0025540804002922. Retrived, November, 2008.

Sunandana, C.S. and Kumar, P.S. (2004). Theoretical approaches to superionic conductivity. *Bulletin of Materials Science,* 27: 1-17.

Suuol, J.J. and Escoda, L. (2007). SEM and TEM studies in alloys developed by mechanical alloying. *In*: A. Méndez-Vilas and J. Díaz (Eds), *Modern research and educational topics in microscopy.*

Synder, K. A., Ferraris, C.,Martys, N. S., and Garboczi, E. J. (2000). Using Impedance Spectroscopy to Assess the Viability of the Rapid Chloride Test for Determining Concrete Conductivity. *Journal of Research of the National Institute of Standards and Technology*, 105: 497.

Tamura, S., Yamamoto, S. and Imanaka, N. (2008). New type of trivalent gadolinium ion conducting solid electrolyte. *Journal of New Materials for Electrochemical Systems, 11 :1-4.*

Tantri, P.S., Greetha, K., Umarji, A.M. and Ramasesha, S.K. (2000). Thermal expansion behaviour of barium and strontium zirconium phosphates. *Bulletin of materials Science,* 23:491-499.

Tarnopolsky, V.A. Aliev, A.D., Churagulove, B.R., Burukhin, A.A., Novikova, S .A. Yaroslavtsev, A.. B. (2003). Influence of thermal treatment on the ion transport of hydrated zirconia. *Solid State Ionics,* 162-163:225-229.

Teneyson, W. (2009). X-ray diffraction: The basics: http://www.nhn.ou.edu/¬bumm/NanoLab/x- ray_Diffraction.ppt. Retrieved, July, 2009.

Thierry, H. C. Nguyen. (1998). CMZP and Mg-doped Al_2TiO_5 thin film coatings for high temperature corrosion protection of Si_3N_4 heat exchangers. M.Sc. Thesis: Virginia Polytechnic Institute and State University, U.S.A.

Trice, R. W., Su, Y.J.,Faber, K.T.,Wang, H. and Porter, W. (1999). The role of NZP additions in plasma-sprayed YSZ: microstructure, thermal stability and phase stability effects. *Materials Science and Engineering,* A272:284-289.

Tschope, A. (2003). Space Charge Layers in Polycrystalline Cerium Oxide. Material Research Society Symposium Proceedings, Vol. 756.

Vera, C.M.C and Aragón, R. (2005). Dependence of *sensitivity* on granulometry in conductimetric γ'-Bi_2MoO_6 sensors. *The Journal of the Argentine Chemical Society*, 93:21-26.

Vijayan, L. (2009). Effect of High-energy Ball-milling on Electrical Properties of $Li_{1.3}Al_{0.3}Ti_{1.7}(PO_4)_{2.9}(VO_4)_{0.1}$ Material. Symposium F: Nanostructured Materials for Electrochemical Energy Systems: Lithium Batteries, Supercapacitors and Fuel Cells. International Conference on Materials for Advanced Technologies and International Union of Materials Research Societies-International Conference in Asia.p21.

Vithal, M., Srinivasulu, B., Koteswara, K., Rao, Ch. M. (2000). Preparation, characterization, ESR and PAS studies of $Cu_{0.5}$ $NbAlP_3$ O_{12} and $HNbAlP_3$ O_{12}. *Materials Letters*, 45:58.

Vitioo, I. (1999). Synthesis, Structure, Conductivity and Electrode properties for some Double Diphosphates, Silicates and Lithium Manganese Oxides. PhD Thesis.Inst. of Solid State Physics, University of Latvia, Riga, Latvia.

Vladicova, D. (2003). Conductivity studies of solid oxide materials for electrical applications. *Impedance contributions online,* 1: I3-1 – I3-34.

Vladislav, A.S., Svetlana, N.P.,Mrina,V.C.,Galina, V.Z.,Raisa,I.M.,sergey,V.T,.,Elena,B.B.,Vladimir,I.Z.,Galina,S.L.,Yiva,V.F .,Dmitry,I,K.,Vladimir,V.K.,Eugene,A.P.,Visevolod,N.K.,Vyacheslav,P.I.,V ladimir,F.A.,Natalia,N.B.,Natalia,N.K.Vale ri,V.L.,Dinesh A. *and* Rustum R. (2002). Synthesis of framework zirconium phosphate via mechanochemical activation of mixed solid salts. *Chemistry for Sustainable Development,* 10:179.

Volkov Yu.F., Kitaev D.B, Lizin A.A., Lukinykh, A.N., Orlova A.I. (2003). New mineral-like ceramics for immobilization of plutonium (structures of monazite and kosnarite): http://www.library.iem.ac.ru/exper/Vol10-1/151-152.pdf.Retrieved, Ausgust, 2009.

Wang, W. and Zhou, N.(1998). Study of Mineral Fast Ion Conductors of Al-Sm-Nasicon:http://www.eng.hawaii.edu/¬ssiII/SSI-II papers/A44.pdf.Retrieved, August, 2009.

West, W.C., Whitacre, J.F., Lim, J.R. (2004). Chemical stability enhancement of lithium conducting solid electrolyte plates using sputtered LiPON thin films. *Journal of Power Sources,* 126:134–138.

Wikipedia (2009). The online Encyclopaedia. Retrieved July, 2009.

Wilkinson, A. (2003). Defects, non-Stoichiometry, solid solutions and ionic conductivity in the solid state: http://www.chemistry.gatech.edu/.../defects_non-stoichiometry_ionic conductivity-solid-state.pdf. Retrieved,October, 2008.

Wilmarth, W.R., D.T. Hob's, Averill, W.A., E., Fox, E., Peterson, R.A. (2007). Review of Ceramatec's caustic recovery technology, July, 20. Washington savannah river company, savannah river site, Aiken, SC 29808. Prepared for the U. S. Department of Energy Under Contract Number DE-AC09-96SR18500.

Wolfenstine, J. (2008). Grain Boundary Conductivity in Crystalline $LiTi_2(PO_4)_3$. Army research laboratory(ARL). Report no. ARL-TN-0313, Adelphi, MD 20783-1197.
USA.

Woodcock, D.A., Lightfoot, P. and Ritter. (1998). Mechanism for low thermal expansion in the cation-ordered NASICON structure. *Chemistry communication*, 107-108.

Woodcock, D.A., Lightfoot, P. and Smith, R.I. (1999). Powder neutron diffraction studies of three low thermal expansion phases in the NZP family: $K_{0.5}Nb_{0.5}Ti_{1.5}(PO_4)_3$, $Ba_{0.5}Ti_2(PO_4)_3$ and $Ca_{0.25}Sr_{0.25}Zr_2(PO_4)_3$. *Journal of Materials Chemistry*, 9: 2631.

Woodward, (2003). Ionic conductors and solid electrolytes I: The Basics:http:// www.chemsirtyohio- state.edu/¬woodword/ch754/lecture 2003/ionic cond /lect 26.ppt.). Retrieved, October,2008.

Wu, J. (2005). Defect chemistry and proton conductivity in Ba-based Perovskites.Unpublished PhD. Thesis. California Institute of Technology, Pasadena, California.

Xu Nian Y. Chung, S.Y., Bloking, J.T., Chiang, Y.M. and Ching, W.Y. (2004). Electronic structure and electrical conductivity of undoped $LiFePO_4$. *Electrical and solid state letters,* 76 : A131-A134.

Xu, X., Wang, J. and Long, Y. (2006). Zeolite-based Materials for Gas Sensors. *Sensors, 6*: 1755.

Y.in, S.-C., Strobel, P. S. Grondey, H. and Nazar, L. F. (2004). $Li_{2.5}V_2(PO_4)_3$: A room- temperature analogue to the Fast-Ion conducting high-temperature γ-phase of $Li_3V_2(PO_4)_3$. *Chemical Materials, 16:* 1456-1465.

Yip, S. (2005). *Handbook of Materials Modeling: Vol.1, Methods and Models.* Springer, Netherlands. pp.1-13.

Zurawaski, A. (2006). Photoacoustic detection of phase transitions. *Physics and chemistry of solid state,* 7:21-24.

Zyryanva, V.N. and Vance,E.R. (1996). Comparison of sodium zircoinium phosphate and synroc matrices for immobilization of high level wastes: http://www.osti.gov./bridge/servelets/purl/102178-4Smo9M/102178.pdf. Retrieved, August, 2009.

APPENDIX A

GLOSSARY

ab initio: it means ' from the beggining' , it is a Latin word.

Armourphous: solid which has disordered atomic structure, example, glasses and polymers. Non crystalline material.

Atomic Absorption Spectroscopy (AAS): a technique used to determine specific metal concentration in a sample. The technique can be used to anlyze over 70 different elements in a solution.

Cole-Cole Plot: a plot of imaginary versus real impedance (Z'', Z'), also known as **Nyquist plots**

Complex Nonlinear Least Squares (CNLS): a form of least squares analyses which is used to fit a set of m observations with a model which is non-linear in n unknown parameters ($m>n$). The basis of the method is to refine the model by a lincar onc and to refine the models by successive iterations.

Crystallites: small, often microscopic crystals that, held together through highly defective boundaries, constitute a crystalline solid. Metallurgists often refer to crystallites as grains.

Density Functional Theory (DFT): a quantum mechanical simulation of periodic systems for many body theory. It is primarilly concerned with the calculation of ground state energy of a collection of atoms

Diffusion Coefficient: a proprtionality constant betwen the moalr flux due to molecular diffusion and the gradient in the concentration of the species.

Dilatometry: the measurement of changes in volume that accompany other physical phenomena such as thermal expansion.

Domains: a region within magnetic materials which has uniform magnetization.

Energy Dispersive Spectroscopy (EDX or EDS): an analytical technique used for the analysis of chemical copmposition of a sample.

Fourier Transform Infrared Spectroscopy (FT-IR): measuremnt technique whereby spectra are collected based on measuremnts of the coherence of a radiative source using time-domain or space domain measurements of the electromagnetic radiation or other types of radiation

Grain Boundary Resistance: the interface between two grains or crystallites in a polycrystalline material. Grain boundaries are defects in the crytal structure. The boundary impedes the flow of current and is thereefore the grain boundary reisitance.

GSAS (General Structure Analysis System): a structural analysis software modules for full profile fitting of X-ray diffraction and neutron data.

Hot-Press Sintering: sintering with pressure is known as hot –pressing.When used for 3D shapes it is called hot isostatic presssing.

Hydrothermal method: a method of synthesizing single crystals which depends on the solubility of minerals in hot water under high pressure.

Hysteresis: this phenomenon is well known in ferromagnetic materials: when an external field is applied to a ferroelectromagnet, the atomic dipoles align themselves with the external field. Even when the external field is removed, part of the alignment will be retained: the material has become magnetized.

Ion exchange: an exchange of ions between two electrolytes or between an electrolyte solution and a complex.

Infrared Spectroscopy (IR): the spectroscopy that deals with the infrared region of the electromagnetic spectrum.

MAS (Magic Angle Spining): a technique used in solid state NMR by spining the sample, usually at a frequency of 1-70 kHz at the magic angle θ_m(54.7°, $\cos^2\theta_m$=1/3).

Mass Spectroscopy (MS): an analytical technique that measures the mass to charge ratio of charged particles.

Microprobe Analysis: an analytical tool used to non destructively determine the chemical composition of small volumes of solid materials.

Monte Carlo (MC): it utilizes random numbers to select from probability distribution and generates atomic configurations in a stochaistic process. It provides ability to reach macroscopc times by modelling diffussional processes and times scales , rather than individual atomic vibrations.

Molecular Dynamics (MD): the simulation technique generates atomic tragectories for an N particle system by direct numerical intergration of Newton's equations of motion based on presumed boundary and initial conditions.The atomic forces are derived from the potential energy functions.

Nanocrsytalline: any nanomaterial with atleast one dimension $\leq 100nm$ and that is single crystalline. Any material with a dimension $\leq$1 micrometre that is one thousand nanometers should be referred to as a nanoparticle not a nanocrystal. Any particle which exhibits regions of crystallinity should be termed nanoparticle or nanocluster based on dimension.

Nanotechnology: study of the controlling of matter on an atomic or molecular scale. Generally nanotechnology deals with structures sized between 1 to 100 nanometer in at least one dimension and involves developing materials and devices within that size, in all solid state nano scale materials.

Nanoionics: is the study and application of phenomena, properties, effects and mechanisms of processes connected with fast ion transport in all solid state nano scale systems.

Nuclear Magnetic Resonace (NMR):-is a property that magnetic nuclei have in a magnetic field and applied electromagnetic (EM) or pulses which cause the nuclei to absorb energy from the EM pulse and radiate this energy back out.

NMR line width: residual line width (full width at half maximum) of ^{13}C nuclei under MAS (Magic Angle Spining) conditions at 5-15kHz, spining rate is typically in the order of 0.5-2 ppm (parts per million).

Phase Transitions: the transition between thermodynamic phases of a physical system, especially one between the solid, liquid and gaseous phases of a substance.

Percolation transition : the theory requires a statistically defined minimum fraction of open volume which is to be distributted in concentration and dimension enough to allow for the desired transport. It is applied in explaining the electrical conductivity of mixtures of conductors and non conductors and complex ionic conductors.

Porosity: is a measure of the void spaces in a material, and is a fraction of the volume of voids over the total volume, between 0–1, or as a percentage between 0–100%.

Polycrystalline: solids that are composed of many crystallites of varyimg size and orientation.

Polymorphism-the ability of materials to exist in more than one form or crystal structure.

Radionuclide: an atom with a stable nuclues, characterized by excess energy which is available to be imparted either to a newly created radiation particle within the nucleus or else to an atomic electron.

Refractory Materials : is one that retains its strenght at high temperature, examples are chromium, firebrick and zirconium dioxide.

Pseudo Potential Method: method of band energy calculation where only the valence electrons are considered. The core electrons are treated as if they are frozen in an atomic–like configuration. As a result the valence elcetrons are thought to move in a free one-electron potential.

Rietveld refinement: a technique designed by Hugo Rietveld for use in the characterization of crystalline materials. The method uses the least squares method to refine a theoretical line profile until it matches the measured profile.

Relaxation Time: relaxation of a perturbed system to equilibrium. Each relaxation process can be characterized by a relaxation time,τ.

Space Group: the set of all symetry operations that can be applied to a crystal without changing it.

Solid Oxide Fuel Cell (SOFC): an electrochemical conversion device that produces electricity from oxidizing a fuel. Fuel cells are characterized by their electrolyte material. They have a solid oxide or ceramic electrolyte. They have high efiiciency,long term stability,fuel flexibitility and low emissions.

Sol-gel Method: also known as chemical solution deposition, is a wet chemical deposition technique widely used in materials science. They are used primarily for the fabrication of materials (oxides) starting from chemical solution (sol) that acts as precursorr for an integrated network(or gel) of either descete particles or network polymers.

Sputtering: physical sputtering is driven by momentum exchange between the ions and atoms in the materials, due to collisions. It is used for deposition of thin films or coatings on materials.

Thin Film-layer of materials ranging from fractions of a nanometre (monolayer) to several micrometres in thickness. Electronic semiconductors devices and optical are the main applications benefitting from thin film construction.

Waveguide: is a structure which guides waves such as electromagnetic waves or sound waves. There are different types of waveguides for each type of wave.

X-ray Photoelectron Spectroscopy(XPS): a quantitative spectroscopic technique that measures elemental composition, emperical formula, chemical state and electronic state of the elements that exists within a material.

APPENDIX B

XRD Powder Diffraction data at room temperature for x =0.00 sample. The ZrO_2 and $NaPO_4$ additional phases are represented by the 2θ values at 33.99 and 48.96°, respectively.

Peak 2θ	I/Io%	h	k	l	d-cal(Å)	d-obs(Å)
18.87	27.00	1	0	4	4.6147	4.6990
19.56	29.80	1	1	0	4.5612	4.5348
19.56	29.80	0	0	5	4.5484	4.5348
20.96	7.30	1	1	2	4.2333	4.2349
22.49	29.40	2	0	0	3.9501	3.9502
22.49	29.40	1	0	5	3.9418	3.9502
27.02	83.10	2	0	4	3.2440	3.2973
30.01	100.00	2	1	0	2.9860	2.9752
30.01	100.00	2	0	5	2.9824	2.9752
32.86	30.20	2	1	3	2.7782	2.7234
33.99	41.90	3	0	0	2.6334	2.6354
39.55	20.30	2	2	0	2.2806	2.2768
39.55	20.30	3	0	5	2.2790	2.2768
43.36	11.40	3	0	7	2.1050	2.0851
44.31	7.90	3	1	4	2.0445	2.0426
46.36	13.90	4	0	1	1.9676	1.9570
47.91	6.90	1	3	6	1.9289	1.8972
48.96	22.60	4	0	4	1.8657	1.8589
53.08	9.60	4	1	0	1.7240	1.7240
53.77	26.40	4	1	2	1.7045	1.7034
56.48	2.40	3	2	6	1.6351	1.6280

APPENDIX C

XRD Powder Diffraction data at room temperature for x =0.25 sample. Additional phases coexist at 34° for ZrO_2 and $Na_5Zr(PO_4)_3$.

Peak 2θ	I/Io%	h	k	l	d-cal	d-obs
19.11	29.4	1	0	4	4.5446	4.6405
19.83	35.7	1	1	0	4.4736	4.4736
19.83	35.7	0	0	5	4.4888	4.4736
21.36	14.9	1	1	2	4.1556	4.1565
22.81	43.1	2	0	0	3.8742	3.8955
22.81	43.1	1	0	5	3.8841	3.8955
25.96	64.3	2	0	3	3.4403	3.4295
27.44	88.4	2	0	4	3.1881	3.2478
27.44	88.4	0	0	7	3.2063	3.2478
30.46	100	2	1	0	2.9286	2.9323
30.46	100	2	0	5	2.9329	2.9323
33.52	13.4	2	0	6	2.6910	2.6713
33.52	13.4	0	2	6	2.6910	2.6713
34	18.7	1	0	8	2.6379	2.6347
34.43	27.4	3	0	0	2.5828	2.6027
34.43	27.4	2	1	4	2.5963	2.6027
38.33	9	3	0	4	2.3462	2.3464
40.45	40.41	2	2	0	2.2368	2.2282
44.25	10.8	0	0	11	2.0404	2.0453
44.63	5.4	2	1	8	2.0259	2.0287

APPENDIX D

XRD Powder Diffraction data at room temperature for x =0.50 sample. Additional phase of $Na_5Zr(PO_4)_3$ at 27.12° exists.

Peak 2θ	I/Io%	h	k	l	d-cal(Å)	d-obs(Å)
16.27	-2.6	0	0	5	4.5491	5.4436
16.69	5.8	0	1	3	5.4692	5.3075
17.37	1.2	0	1	3	5.4692	5.1013
18.99	85.9	1	0	4	4.6131	4.6696
19.47	39.3	1	1	0	4.5593	4.5555
19.47	39.3	0	0	5	4.5525	4.5555
21.15	22.4	1	1	2	4.2323	4.1973
21.28	-2.3	1	1	2	4.2323	4.1720
24.94	2.8	1	1	4	3.5581	3.5674
25.32	5	1	1	4	3.5581	3.5147
25.95	6	2	0	3	3.5026	3.4308
26.14	7.7	1	0	6	3.4196	3.4063
27.12	62.5	2	0	4	3.2440	3.2854
27.12	62.5	1	1	5	3.2215	3.2854
29.96	100	2	1	0	2.9847	2.9801
29.96	100	2	0	5	2.9828	2.9801
30.52	13.2	1	1	6	2.9162	2.9267

APPENDIX E

XRD Powder Diffraction data at room temperature for x =0.75 sample. Additional phase of $Na_5Zr(PO_4)_3$ exists at 34.08°.

Peak 2θ	I/Io%	h	k	l	d-cal(Å)	d-obs(Å)
19.15	38.4	1	0	4	4.5692	4.6309
19.72	19.2	1	1	0	4.4982	4.4983
19.72	19.2	0	0	5	4.4983	4.4983
22.69	37.4	2	0	0	3.8956	3.9158
22.69	37.4	1	0	5	3.8956	3.9158
25.88	100	2	0	3	3.4568	3.4399
25.88	100	2	0	3	3.4568	3.4399
27.26	62.1	0	2	4	3.2022	3.2688
27.26	62.1	1	1	5	3.1808	3.2688
30.29	30.29	2	0	5	2.9448	2.9484
34.08	40.4	0	1	8	2.6445	2.6287
34.08	40.3	0	1	8	2.6445	2.6287
53.91	32.7	4	1	1	1.6953	1.6994

APPENDIX F

Crystallite sizes (N) (in Amstrong units) at different 2θ values for compositions x=0.00-0.75 calculated from the Scherer equation, Eq.(9) and the correspomnding Full Width at Half Maximum (FWHM) values.

X=0.00 **x=0.25**

$2\theta°$	$\theta°$	FWHM(β)	Crystallite Size N Å	$2\theta°$	$\theta°$	FWHM(β)	Crystallite Size N Å
18.87	9.44	0.5843	2.3409	17.38	8.69	0.5250	2.6083
19.56	9.78	0.4408	3.0995	18.05	9.03	0.1580	8.6680
20.96	10.48	0.5824	2.3409	19.11	9.56	0.5383	2.5399
22.49	11.25	0.4962	2.7409	19.83	9.92	0.4567	2.9907
27.02	13.51	0.6684	2.0169	21.36	10.68	0.6170	2.2082
30.01	15.01	0.9445	1.4179	22.81	11.41	0.3404	3.9924
32.86	16.43	1.3534	0.9827	25.96	12.98	0.8644	1.8773
33.99	17.00	0.9543	1.3895	27.44	13.72	0.5060	2.6618
39.55	19.78	1.0216	1.2772	30.46	15.23	0.5057	2.6455
43.36	21.68	0.6942	1.8560	33.52	16.76	2.1141	0.6280
44.31	22.16	0.7464	1.7206	34.00	17.00	0.4904	2.7038
43.36	23.18	0.8252	1.5446	34.43	17.22	1.4904	0.8897
47.91	23.96	0.5714	2.2176	35.43	17.72	2.4904	0.5324
48.96	24.48	0.9735	1.2962	38.33	19.17	2.4904	0.3799
53.08	26.54	0.6005	2.0658	40.45	20.23	4.4904	0.2953
53.77	26.89	0.7724	1.6011	44.25	22.13	5.4904	0.2415
56.48	28.84	0.6698	1.8238	44.63	22.32	6.4904	0.2043

X=0.50 **x=0.75**

$2\theta°$	$\theta°$	FWHM(β)	Crystallite Size N Å	$2\theta°$	$\theta°$	FWHM(β)	Crystallite Size N Å
16.27	8.14	0.81416	1.6797	19.15	9.58	0.6534	2.0923
16.69	8.35	0.67675	2.0208	19.72	9.86	0.3672	3.7206
17.37	8.69	0.21259	6.4328	22.69	11.35	0.5447	2.4960
18.99	9.50	0.6625	2.0641	25.88	12.94	0.3487	3.8756
19.47	9.74	0.5966	2.2905	27.86	13.63	0.6539	2.0667
24.94	12.47	0.4907	2.7591	30.29	15.15	0.7212	1.8557
25.32	12.66	1.4907	0.9082	34.08	37.04	0.9720	1.3638
25.95	12.98	2.4907	0.5436	53.91	26.96	0.9942	1.2432
26.14	13.07	0.5066	2.6661				
27.12	13.56	0.5067	2.6599				
29.96	14.98	1.2805	1.0460				
30.52	15.26	0.3870	3.4569				

APPENDIX G

Specimen data for Differential Thermal Analyses (DTA) at different temperatures for compositions x=0.00-0.75 and the corresponding heat flow rates.

x=0.00		x=0.25		x=0.50		x=0.75	
Temp,K	Heat flow,mw/mg	Temp,K	Heat flow,mw/mg	Temp,K	Heat flow,mw/mg	Temp,K	Heat flow,mw/mg
297.07	-0.10181	298.515	-5.70E-02	295.59	-3.04E-02	273	-4.05E-02
302.07	-0.16469	303.515	-0.35905	300.59	-0.40135	295.615	-0.26985
307.07	-0.26564	308.515	-0.62568	305.59	-0.71609	300.615	-0.45989
312.07	-0.34482	313.515	-0.83475	310.59	-0.98521	305.615	-0.6095
317.07	-0.41081	318.515	-1.01208	315.59	-1.21968	310.615	-0.73533
322.07	-0.44056	323.515	-1.15383	320.59	-1.40687	315.615	-0.83196
327.07	-0.43674	328.515	-1.28276	325.59	-1.54725	320.615	-0.91135
332.07	-0.4704	333.515	-1.40227	330.59	-1.68814	325.615	-0.98873
337.07	-0.50893	338.515	-1.51171	335.59	-1.83024	330.615	-1.06877
342.07	-0.54398	343.515	-1.61218	340.59	-1.97543	335.615	-1.14589
347.07	-0.57564	348.515	-1.70734	345.59	-2.11146	340.615	-1.21712
352.07	-0.60389	353.515	-1.79881	350.59	-2.23521	345.615	-1.28132
357.07	-0.62925	358.515	-1.89496	355.59	-2.34558	350.615	-1.3388
362.07	-0.65247	363.515	-1.99743	360.59	-2.4465	355.615	-1.39177
367.07	-0.67445	368.515	-2.08519	365.59	-2.54234	360.615	-1.44652
372.07	-0.69662	373.515	-2.17265	370.59	-2.63995	365.615	-1.50428
377.07	-0.71945	378.515	-2.26042	375.59	-2.7375	370.615	-1.56574
382.07	-0.74419	383.515	-2.34167	380.59	-2.83964	375.615	-1.6281
387.07	-0.77104	388.515	-2.41378	385.59	-2.93831	380.615	-1.68722
392.07	-0.79304	393.515	-2.47581	390.59	-3.02855	385.615	-1.74077

APPENDIX H

Specimen data for Thermogravimetric Analyses (TGA) at different temperatures for compositions x=0.00-0.75 and the corresponding mass losses.

x=0.00		x=0.25		x=0.50		x=0.75	
Temp,K	Mass loss (%)	Temp,K	Mass loss(%)	Temp,K	Mass loss (%)	Temp,K	Mass loss(%)
304.81	99.8214	304.69	99.8092	304.81	99.8326	305.56	99.6876
304.81	99.8214	304.69	99.8092	304.81	99.8326	305.56	99.6876
304.81	99.8214	304.7	99.8092	304.81	99.8326	305.56	99.685
304.81	99.8214	304.7	99.8092	304.82	99.8326	305.56	99.685
304.82	99.8214	304.7	99.8092	304.82	99.8326	305.56	99.685
304.82	99.8192	304.7	99.8069	304.82	99.8326	305.56	99.685
304.82	99.8192	304.7	99.8069	304.82	99.8299	305.56	99.6825
304.82	99.8192	304.7	99.8069	304.82	99.8299	305.56	99.6825
304.82	99.8192	304.71	99.8069	304.82	99.8299	305.56	99.6825
304.83	99.8192	304.71	99.8069	304.83	99.8299	305.56	99.6825
304.83	99.817	304.71	99.8069	304.83	99.8299	305.56	99.6799
304.83	99.817	304.71	99.8046	304.83	99.8299	305.56	99.6799
304.83	99.817	304.71	99.8046	304.83	99.8299	305.56	99.6799
304.83	99.817	304.71	99.8046	304.83	99.8272	305.56	99.6773
304.83	99.817	304.71	99.8046	304.84	99.8272	305.56	99.6773
304.83	99.817	304.72	99.8046	304.84	99.8272	305.56	99.6773
304.84	99.8148	304.72	99.8046	304.84	99.8272	305.56	99.6773
304.84	99.8148	304.72	99.8046	304.84	99.8272	305.56	99.6748

APPENDIX I

Specimen data for Impedance Spectroscopy Analyses for compositions x=0.00,0.50 and 0.75 at different temperatures and frequencies and the correspondiing real (σ') and imaginary (σ'') parts of conductivity

x=0.00

Temp,K	Freq, Hz	σ',S/m	σ'',S/m
3.10E+02	3.00E+05	2.01E-05	3.50E-04
3.10E+02	3.47E+05	1.45E-05	3.47E-04
3.10E+02	4.02E+05	4.43E-05	4.24E-04
3.10E+02	4.70E+05	-2.33E-07	5.12E-04
3.10E+02	5.38E+05	5.22E-05	5.17E-04
3.10E+02	6.23E+05	-1.79E-05	6.28E-04
3.10E+02	7.21E+05	1.83E-05	7.33E-04
3.10E+02	8.35E+05	3.40E-05	8.88E-04
3.10E+02	9.66E+05	1.51E-05	9.71E-04
3.10E+02	1.12E+06	2.73E-05	1.15E-03
3.10E+02	1.29E+06	-1.51E-05	1.32E-03
3.10E+02	1.50E+06	3.13E-05	1.54E-03
3.10E+02	1.75E+06	2.56E-05	1.77E-03
3.10E+02	2.01E+06	1.27E-05	2.07E-03
3.10E+02	2.32E+06	3.47E-05	2.40E-03
3.10E+02	2.69E+06	4.22E-05	2.71E-03
3.10E+02	3.11E+06	2.07E-05	3.19E-03
3.10E+02	3.60E+06	6.29E-05	3.70E-03
3.10E+02	4.17E+06	6.71E-05	4.24E-03
3.10E+02	4.88E+06	5.35E-06	4.96E-03

x=0.50

Temp,K	Freq, Hz	σ',S/m	σ'',S/m
3.10E+02	3.00E+05	5.16E-03	6.52E-03
3.10E+02	3.47E+05	5.42E-03	6.91E-03
3.10E+02	4.02E+05	5.92E-03	7.65E-03
3.10E+02	4.70E+05	6.34E-03	8.40E-03
3.10E+02	5.38E+05	6.79E-03	9.04E-03
3.10E+02	6.23E+05	7.37E-03	9.88E-03
3.10E+02	7.21E+05	7.97E-03	1.08E-02
3.10E+02	8.35E+05	8.45E-03	1.18E-02
3.10E+02	9.66E+05	8.98E-03	1.29E-02
3.10E+02	1.12E+06	9.62E-03	1.42E-02
3.10E+02	1.29E+06	1.02E-02	1.56E-02
3.10E+02	1.50E+06	1.10E-02	1.73E-02
3.10E+02	1.75E+06	1.16E-02	1.93E-02
3.10E+02	2.01E+06	1.22E-02	2.12E-02
3.10E+02	2.32E+06	1.29E-02	2.37E-02
3.10E+02	2.69E+06	1.36E-02	2.65E-02
3.10E+02	3.11E+06	1.43E-02	2.96E-02
3.10E+02	3.60E+06	1.49E-02	3.34E-02
3.10E+02	4.17E+06	1.57E-02	3.76E-02
3.10E+02	4.88E+06	1.65E-02	4.28E-02

				3.10E+02	5.58E+06	1.72E-02	4.80E-02
3.10E+02	5.58E+06	4.86E-05	5.66E-03				
				3.10E+02	6.46E+06	1.80E-02	5.44E-02
3.10E+02	6.46E+06	3.10E-05	6.60E-03				
				3.10E+02	7.48E+06	1.90E-02	6.18E-02
3.10E+02	7.48E+06	4.81E-05	7.62E-03				
				3.10E+02	8.66E+06	1.97E-02	7.04E-02
3.10E+02	8.66E+06	-2.20E-05	8.84E-03				
				3.10E+02	1.00E+07	2.05E-02	8.02E-02
3.10E+02	1.00E+07	5.38E-05	1.02E-02				
				3.10E+02	1.16E+07	2.15E-02	9.17E-02
3.10E+02	1.16E+07	3.77E-05	1.18E-02				
				3.10E+02	1.34E+07	2.24E-02	1.05E-01
3.10E+02	1.34E+07	8.25E-05	1.36E-02				
				3.10E+02	1.55E+07	2.33E-02	1.20E-01
3.10E+02	1.55E+07	9.81E-05	1.57E-02				

x=0.75

Temp,K	freq.,Hz	σ',S/m	σ'', S/m	Temp,K	freq.,Hz	σ',S/m	σ'', S/m
3.10E+02	3.00E+05	6.16E-03	8.36E-03	3.10E+02	2.32E+06	1.27E-02	3.61E-02
3.10E+02	3.47E+05	6.64E-03	9.14E-03	3.10E+02	2.69E+06	1.31E-02	4.10E-02
3.10E+02	4.02E+05	7.00E-03	1.02E-02	3.10E+02	3.11E+06	1.35E-02	4.68E-02
3.10E+02	4.70E+05	7.55E-03	1.10E-02	3.10E+02	3.60E+06	1.39E-02	5.33E-02
3.10E+02	5.38E+05	7.95E-03	1.21E-02	3.10E+02	4.17E+06	1.41E-02	6.11E-02
3.10E+02	6.23E+05	8.60E-03	1.33E-02	3.10E+02	4.88E+06	1.46E-02	7.07E-02
3.10E+02	7.21E+05	9.13E-03	1.47E-02	3.10E+02	5.58E+06	1.48E-02	8.04E-02
3.10E+02	8.35E+05	9.48E-03	1.62E-02	3.10E+02	6.46E+06	1.51E-02	9.25E-02
3.10E+02	9.66E+05	1.01E-02	1.80E-02	3.10E+02	7.48E+06	1.55E-02	1.06E-01
3.10E+02	1.12E+06	1.06E-02	2.00E-02	3.10E+02	8.66E+06	1.57E-02	1.22E-01
3.10E+02	1.29E+06	1.11E-02	2.23E-02	3.10E+02	1.00E+07	1.61E-02	1.41E-01
3.10E+02	1.50E+06	1.15E-02	2.51E-02	3.10E+02	1.16E+07	1.65E-02	1.63E-01

APPENDIX J

Specimen dc conductivity data at different temperatures for composions x=0.00-0.75 for the bulk (σ_b) and total (σ_t) conductivities.

x=0.00		
T,K	σ_b,S/m	σ_t,S/m
520	--	8E-5
530	--	1.111E-4
540	--	1.354E-4
550	--	1.71E-4
560	--	2.075E-4
570	--	2.755E-4
580	--	3.025E-4
590	--	3.682E-4
600	-	4.186E-4

x=0.50			x=0.75		
T,K	σ_b,S/m	σ_t,S/m	T,K	σ_b,S/m	σ_t,S/m
370	0.0077	-	400	0.01169	0.00202
380	0.00886	-	410	0.0159	0.00258
390	0.0093	-	420	0.0199	0.00336
400	0.0129	-	430	0.0227	0.00417
410	0.01397	-	440	0.0296	0.00527
420	0.01627	-	450	0.0386	0.00662
430	0.02133	-	460	0.0473	0.0083
440	0.02283	0.00384	470	0.056	0.01035
450	0.02965	0.00467	480	0.0714	0.0128
460	0.03548	0.00568	490	0.0911	0.0158
470	0.04068	0.00686	500	0.0962	0.0193
480	0.052	0.00826	510	0.124	0.0234
490	0.0571	0.00992	520	0.137	0.0283
500	0.0799	0.01186	530	0.1577	0.0339
510	0.0992	0.0144	540	0.1745	0.04034
520	0.1156	0.01668	550	0.2044	0.0478
530	0.13	0.01972	560	0.2218	0.05635
540	0.1502	0.02311	570	0.2683	0.0656
550	0.179	0.027	580	0.2987	0.07617
560	0.2	0.03122	590	0.3	0.0881